Predicting Structure-Property Relationships in Polymers through the Development of Thermodynamically Consistent Coarse-Grained Molecular Models

by

Vipin Agrawal

A Dissertation Presented in Partial Fulfillment
of the Requirements for the Degree
Doctor of Philosophy

Approved June 2016 by the
Graduate Supervisory Committee:

Jay Oswald, Chair
Pedro Peralta
Ralph Chamberlin
Kiran Solanki
Yang Jiao

ARIZONA STATE UNIVERSITY

August 2016

ABSTRACT

Improved knowledge connecting the chemistry, structure, and properties of polymers is necessary to develop advanced materials in a materials-by-design approach. Molecular dynamics (MD) simulations can provide tremendous insight into how the fine details of chemistry, molecular architecture, and microstructure affect many physical properties; however, they face well-known restrictions in their applicable temporal and spatial scales. These limitations have motivated the development of computationally-efficient, coarse-grained methods to investigate how microstructural details affect thermophysical properties. In this dissertation, I summarize my research work in structure-based coarse-graining methods to establish the link between molecular-scale structure and macroscopic properties of two different polymers. Systematically coarse-grained models were developed to study the viscoelastic stress response of polyurea, a copolymer that segregates into rigid and viscous phases, at time scales characteristic of blast and impact loading. With the application of appropriate scaling parameters, the coarse-grained models can predict viscoelastic properties with a speed up of 5-6 orders of magnitude relative to the atomistic MD models. Coarse-grained models of polyethylene were also created to investigate the thermomechanical material response under shock loading. As structure-based coarse-grained methods are generally not transferable to states different from which they were calibrated at, their applicability for modeling non-equilibrium processes such as shock and impact is highly limited. To address this problem, a new model is developed that incorporates many-body interactions and is calibrated across a range of different thermodynamic states using a least square minimization scheme. The new model is validated by comparing shock Hugoniot properties with atomistic and experimental data for polyethylene. Lastly, a high fidelity coarse-grained model of polyethylene was constructed that reproduces the joint-probability distributions of structural vari-

ables such as the distributions of bond lengths and bond angles between sequential coarse-grained sites along polymer chains. This new model accurately represents the structure of both the amorphous and crystal phases of polyethylene and enabling investigation of how polymer processing such as cold-drawing and bulk crystallization affect material structure at significantly larger time and length scales than traditional molecular simulations.

ACKNOWLEDGMENTS

I would like to express my sincere appreciation to my advisor, Dr. Jay Oswald, for his mentoring, guidance, and encouragement over the past four and a half years. He gave me enough freedom to pursue my own ideas while he was always available for discussion and promptly answered my emails even after midnight. I have been incredibly fortunate to have been his student and his contagious enthusiasm, perseverance, and insightful vision for research will always be among the virtues I can learn and benefit in my lifetime.

I would like to thank my collaborators, Dr. Pedro Peralta and Dr. Gaurav Arya for their valuable discussion on coarse-graining methods and shock physics. I would also like to thank my thesis committee members, Dr. Ralph Chamberlin, Dr. Kiran Solanki, and Dr. Yang Jiao, for their advice and participation in my defense. I would like to thank the help and support from my colleagues at Arizona State University, Xiao Liao, Dr. Rui Yuan, Yiyang Li, Dr. Mehul Bhatia, and Dr. Ilaksh Adlakha.

I gratefully acknowledge support from the Office of Naval Research under grant numbers N00014-14-1-0824 and N00014-14-1-0295.

Most importantly, I would like to thank my family. Their unyielding love, support, and encouragement made everything easier to achieve.

TABLE OF CONTENTS

CHAPTER Page

LIST OF TABLES

LIST OF FIGURES

Figure Page

Figure Page

Chapter 1

PREDICTION OF VISCOELASTIC PROPERTIES FOR POLYUREA

1.1 Introduction

Polyurea is an elastomeric, alternating copolymer synthesized from the reaction between a difunctional isocyanate and a difunctional amine. Typically, the isocyanate is based on an aromatic moiety and the amine is based on a polyether, resulting in a polyurea chain with alternating regions of long, flexible, aliphatic segments and short, rigid, aromatic segments [1, 2]. Due to differences in the chemical interactions of the two types of segments, polyurea undergoes microphase segregation to yield hard domains, comprised primarily of ordered aromatic segments, surrounded by a soft, viscoelastic matrix, comprised of mostly aliphatic segments. The soft matrix allows polyurea to sustain large viscoelastic deformations while the hard domains serve as physical cross-links and reinforcing fillers [3, 4], affording polyurea mechanical toughness. The hard domains exhibit extensive intermolecular hydrogen bonding between urea functional groups [5, 6]. Such structured morphology seems to endow polyurea with excellent dissipative properties, making polyurea a useful material for shock-resistant coatings and reinforced composites [2]. More recently, polyurea has found potential applications in protective gear of soldiers for mitigating shocks from blasts and ballistic impacts to prevent traumatic brain injury [7–9]. This has spawned a renewed interest in polyurea, especially in resolving the molecular origin of its superior dissipative properties and using this knowledge to design new, improved shock mitigating materials.

In one commercial variant, polyurea is synthesized by reacting Versalink P-1000,

with Isonate 143L. Versalink P-1000 [10] is composed of poly(tetramethylene oxide) di-p-aminobenzoate), with a molecular weight of 1,238 g/mol, shown in Fig. 1.1a. Isonate 143L [11], is a mixture of difunctional and trifunctional isocyanates and other unspecified additives. Due to its proprietary nature, the exact composition of Isonate 143L is not available. Its chemical assay likely consists of oils, stabilizers, antioxidants, and other unspecified additives, and thus the reaction of these prepolymers is more complex than the isocyanate functional groups reacting with the amine functional groups.

In this work, a simplified version of polyurea molecule is considered for molecular modeling. This simplified molecule is synthesized by reacting 4,4′ methylene diphenyl diisocyanate (MDI), as shown in Fig 1.1b with poly(tetramethylene oxide) di-p-aminobenzoate. These efforts are part of an initiative to develop elastomeric composites with optimally designed compositions and characteristics to manage blast-induced stress-wave energy.

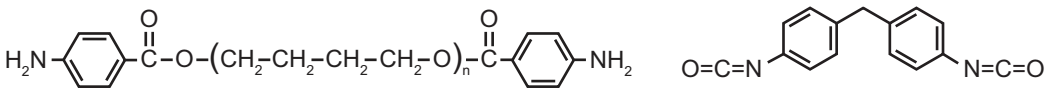

(a) (b)

Figure 1.1: Chemical structures of the prepolymers used to create the benchmark polyurea: (a) poly(tetramethylene oxide) di-p-aminobenzoate, and (b) 4,4′-methylenebis(phenyl isocyanate).

Standard experimental methods to measure viscoelastic material properties, such as relaxation/creep measurements, dynamic mechanical analysis (DMA), and wave propagation testing, generally suffer from limited scope of time or frequency. Therefore, the material response at very short and very long time scales is not easily accessible by direct measurement. These limitations are either physical (how fast the specimen can be loaded in a controlled manner) or practical (how long experimen-

talists can wait to record data). Generally, measurement times of the viscoelastic response of a material range from seconds to hours, although ultrasonic testing allows the linear mechanical response to be measured in the microsecond regime. This range of practical experimental time scales is not typically sufficient to fully characterize the material response, as many polymers do not show a definite plateau in relaxation or creep even when the testing is extended into days. Furthermore, the measured "instantaneous" values represent the time scale of the testing setup more than the real short time response of the material.

The method of time-temperature superposition [12] allows for estimation of properties over a much broader spectrum of time scales by making measurements at accessible time scales over a relatively wide temperature range. The principle behind such equivalence is that the mechanics of polymers are dominated by the collective and statistical rearrangement of molecular chains. High rate deformations at a given temperature may be estimated by looking at how the material behaves at low rates and lower temperatures, where there is reduced free volume and thermal energy available for the rearrangement of molecular chains in response to an applied stress or other driving force, e.g. electric field. Therefore, a viscoelastic master curve that extends over many more decades in time (or frequency) than what practical constraints on laboratory tests allow can be produced from both high and low temperature testing. Over the past 50 years, this technique has been shown to provide very reliable estimates for thermorheologically-simple polymers, i.e. those whose transition mechanisms all share a consistent scaling in time with changes in temperature [12–14].

As polyurea is a phase-separated, block copolymer, it should generally be considered as thermorheologically-complex and cannot, in principle, be shifted from one temperature to another by a constant factor. Nevertheless, Zhao et al. [15] successfully applied time-temperature superposition with the well-known Williams-Landel-Ferry

(WLF) equation to polyurea to extract its properties at short time frames for modeling small-deformation wave propagation in a Hopkinson bar test. Their results show that viscoelastic properties determined through quasistatic measurements and shifted with time-temperature superposition can be used to make predictions that are consistent with wave propagation measurements in split Hopkinson bar experiments. Thus, they conclude that polyurea, despite its complexity, obeys the time-temperature superposition principle and a classical viscoelastic master curve can properly predict its material response for dynamic situations, even when the deformation rates exceed the quasistatic characterization by factors of 10^6 to 10^8. Earlier work by Amirkhizi et al. [16] included the effect of pressure into the WLF equation to create a pressure and temperature dependent viscoelastic model of polyurea, based on the argument that large hydrostatic pressures decrease free volume and therefore chain mobility.

Recent experiments to measure the dynamic mechanical and ultrasonic properties of polyurea conducted by Qiao et al. [17], have provided further confirmation that time-temperature superposition provides reliable estimates of the dynamic storage modulus at high frequencies, however the predicted loss moduli were significantly lower than those calculated from ultrasonic wave dissipation at high frequencies. A possible explanation given for this discrepancy is the activation of internal resonances between hard domains in polyurea, a phenomenon that would not be accounted for by time-temperature superposition analysis.

The development of a computational platform that can predict high frequency viscoelastic properties from polymer chemistry and microstructure is thus motivated to improve the understanding of the viscoelastic properties of thermorheologically-complex polymers. However, creating such a platform remains a formidable task due to the wide range of spatial and temporal scales over which stress relaxation occurs. One approach toward bridging molecular simulations with macroscopic re-

sponse is through hierarchical multiscale methods, where physical parameters of theoretical models are estimated from atomistic simulations. This approach was recently demonstrated by Li et al. [18] to predict the viscoelastic properties of polyisoprene by combining atomistic and CG simulations with primitive chain analysis [19] to extract the parameters of the tube model of primitive paths [20, 21], which is then bridged to a finite strain, constitutive law. The reader is referred to a recent review by Li et al. [22] for a comprehensive overview of multiscale techniques for modeling polymeric materials.

For a phase segregated copolymer such as polyurea, molecular chains within soft domains are constrained both through entanglements and by connectivity to the hard domains, which act as chemical cross-links. The reduction of soft phase mobility was previously proposed based on dielectric measurements of segmental relaxation processes in polyurea [23]. The extra constraints on the soft domain chains could in principle be accounted for through a modified tube theory, similar to those developed to predict the constraints on entangled polymer nanocomposites [24]. Such physically based models require *a-priori* knowledge of the essential physical mechanisms governing stress relaxation. The unexpected, higher loss observed in polyurea under ultrasonic loading is not reproducible under such theories without a phenomenological correction or fundamental knowledge of the loss mechanism responsible. This lack of knowledge motivates the development of CG simulation methods that can directly predict the effect of the two-phase structure of polyurea on its viscoelastic properties.

Many bottom-up strategies to produce CG models for specific polymer chemistries have been developed based on force matching approaches [25, 26] or by systematic matching of atomistic structural features using methods such as inverse Monte Carlo (IMC) [27], or iterative Boltzmann inversion (IBI) [28–30]. Shell and coworkers developed a general framework based on the relative entropy method [31, 32] to which

the IMC and IBI methods are closely related. Models arising from bottom-up strategies generally fail to predict accurate thermomechanical properties for a variety of reasons, including their lack of temperature transferability and the reduced friction acting amongst particles due to their coarsened, and thus more smooth, free energy landscape. Furthermore, some thermodynamical properties, such as heat capacity, will clearly differ in the CG model due to the reduced degrees of freedom available to store vibrational energy.

Hybrid approaches for developing more representative models combine bottom-up and top-down strategies, in which some accuracy in matching structural features is sacrificed to explicitly calibrate the model to match select thermophysical properties. Recent examples include models developed by Hsu et al. [33, 34], where CG nonbonded interactions are modeled by an LJ potential with parameters optimized to match experimentally measured values of density, glass transition temperature, and elastic modulus. Although hybrid approaches have been successful in modeling homopolymers, the loss of accuracy in reproducing radial distribution functions is undesirable when modeling a phase segregating polymer such as polyurea.

An alternative approach combining bottom-up coarse-graining strategies with dissipative particle dynamics (DPD) was demonstrated by Maurel et al. [35, 36] by which CG models for polymer melts and cross-linked polymers were developed that can reproduce atomistic structural distributions and approximate long term dynamic processes such as the relaxation time of the autocorrelation vector of the end-to-end vector. From these models, density, entanglement mass, end-to-end distance and thermal expansion properties were computed with good agreement between experiment and simulation. However, for simple homopolymers the calibration of the DPD friction coefficient and dissipation cutoff radius is complex [37] and thus it is not clear how one would select appropriate values for copolymers. Furthermore, as the objec-

tive in this study is to explore microsecond to millisecond time scales, it is desirable to exploit the faster time scales inherent to CG models provided that a consistent mapping can be made from simulation to real time scales.

To develop an accurate coarse-grained (CG) model of polyurea, we implement the iterative Boltzmann inversion (IBI) method [28–30], previously used successfully to coarse-grain a variety of other polymers [28, 35, 38–40]. Briefly, this approach treats the atomistic polymer chain as a chain of CG beads, where each bead represents a groups of atoms along a polymer chain, allowing polymer chains to be described by significantly fewer degrees of freedom. The CG beads interact with each other, both along and across chains, through "effective" potentials derived in an rigorous, iterative manner such that the CG bead-chain exhibits similar configurational properties as the fully atomistic polymer chain; in other words, the CG bead-chain reproduces the structural distributions of the atomistic chains obtained from molecular dynamics (MD) simulations.

In this work, we develop two different variations of CG model of polyurea. The first variation so called 2-bead model used two different kind of beads for CG mapping scheme (Figure 1.2a). Due to differences in the physical properties of the hard and soft segments, we use two distinct CG beads in representing such a chain. One type of bead, which we term soft bead, or "S" for short, represents each of the 14 repeating -C_4H_8O- units in the soft segment (Figure 1.2d). A second type of bead, which we term hard bead or "H", represents each of the 2 symmetric halves -C_6H_6-NH-CO-NH-C_6H_6-CO- of the hard segment (Figure 1.2d). The resulting CG bead-chain can therefore be denoted by $(H_2S_{14})_n$, where n denotes the number of times the H_2S_{14} block is repeated, depending on the degree of polymerization of the polyurea chains.

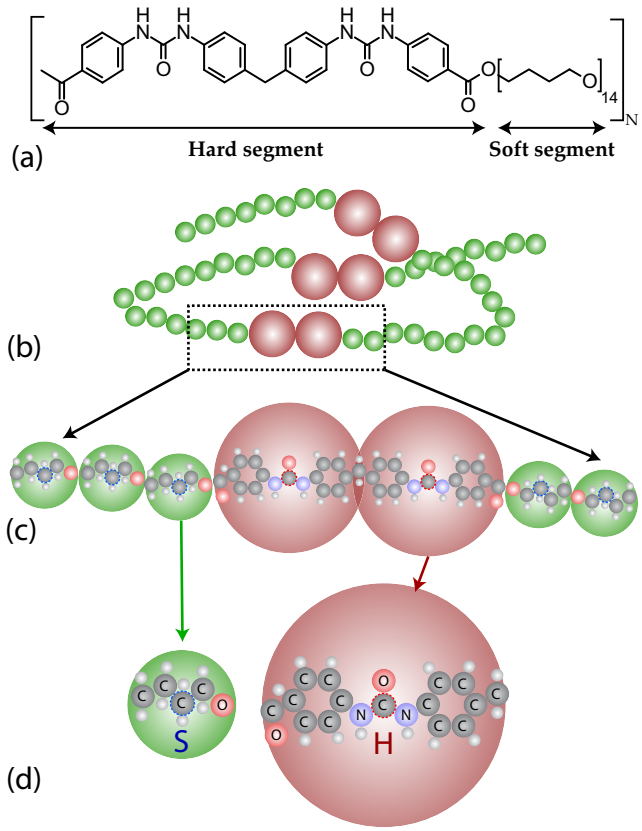

Figure 1.2: 2-bead CG model of polyurea: (a) chemical structure of the repeating units of polyurea consisting of alternate hard and soft segments, (b) figurative representation of a short polyurea chain composed of coarse-grained beads, (c) coarse-grained mapping of hard and soft segments of polyurea, and (d) chemical structure of CG mapped beads; S represents the soft bead while H represents the hard bead. The carbon atoms within each bead that are encircled by dotted lines are the virtual sites from which interbead distances are calculated in the generation of structural distribution functions.

Each CG bead type is assigned a mass equal to the sum of the molecular weights of its atomic constituents ($m_H = 245$ g/mol and $m_S = 72$ g/mol). The total potential

energy of the CG bead-chain U_{tot} is given by three contributions:

$$U_{\text{tot}} = U_{\text{str}} + U_{\text{bend}} + U_{\text{nonb}} \tag{1.1}$$

where U_{str} is the energy associated with stretching the bonds between adjacent beads along the bead-chain, U_{bend} is the energy associated with bending the angles subtended by consecutive bonds, and U_{nonb} is the energy of non-bonded interactions between beads, on separate chains or beads located further than two bonds apart on the same chain. Many studies include a fourth contribution arising from the dihedral angles defined by four consecutive beads along the chain. However, we find that such a contribution is not required, as explained later.

The total bond stretching energy U_{str} is calculated as the sum of stretching energies of the three types of bonds present in the CG system:

$$U_{\text{str}} = \sum_{i=1}^{N_{\text{H-H}}} \mathcal{V}^{\text{str}}_{\text{H-H}}(l_i) + \sum_{i=1}^{N_{\text{H-S}}} \mathcal{V}^{\text{str}}_{\text{H-S}}(l_i) + \sum_{i=1}^{N_{\text{S-S}}} \mathcal{V}^{\text{str}}_{\text{S-S}}(l_i) \tag{1.2}$$

where l_i is the length of the i^{th} bond; $\mathcal{V}^{\text{str}}_{\text{H-H}}$, $\mathcal{V}^{\text{str}}_{\text{H-S}}$, and $\mathcal{V}^{\text{str}}_{\text{S-S}}$ are the CG potentials describing the stretching energies of the *H–H*, *H–S*, and *S–S* bonds as a function of their lengths, respectively; and $N_{\text{H-H}}$, $N_{\text{H-S}}$, and $N_{\text{S-S}}$ are the number of bonds of each type present in the system.

Similarly, the net bending energy U_{bend} has contributions arising from the three types of bond angles present in the CG model:

$$U_{\text{bend}} = \sum_{i=1}^{N_{\text{H-H-S}}} \mathcal{V}^{\text{bend}}_{\text{H-H-S}}(\theta_i) + \sum_{i=1}^{N_{\text{H-S-S}}} \mathcal{V}^{\text{bend}}_{\text{H-S-S}}(\theta_i) + \sum_{i=1}^{N_{\text{S-S-S}}} \mathcal{V}^{\text{bend}}_{\text{S-S-S}}(\theta_i) \tag{1.3}$$

where θ_i is the angle between the i^{th} set of consecutive bonds; $\mathcal{V}^{\text{bend}}_{\text{H-H-S}}$, $\mathcal{V}^{\text{bend}}_{\text{H-S-S}}$, and $\mathcal{V}^{\text{bend}}_{\text{S-S-S}}$ are the CG potentials describing the energy of bending the angles subtended by *H–H–S*, *H–S–S*, and *S–S–S* segments as a function of their bending angles; and $N_{\text{H-H-S}}$, $N_{\text{H-S-S}}$, and $N_{\text{S-S-S}}$ are the number of bending angles of each type present in the system.

Finally, the total non-bonded energy U_{nonb} is calculated as the sum of all non-bonded interactions in between and across the H and S beads in the CG system:

$$U_{\text{nonb}} = \sum_{i=1}^{N_{\text{H}}-1} \sum_{j=i+1}^{N_{\text{H}}} \mathcal{V}_{\text{H/H}}^{\text{nonb}}(r_{ij}) + \sum_{i=1}^{N_{\text{H}}} \sum_{j=1}^{N_{\text{S}}} \mathcal{V}_{\text{H/S}}^{\text{nonb}}(r_{ij}) + \sum_{i=1}^{N_{\text{S}}-1} \sum_{j=i+1}^{N_{\text{S}}} \mathcal{V}_{\text{S/S}}^{\text{nonb}}(r_{ij}) \qquad (1.4)$$

where r_{ij} is the distance between beads i and j; $\mathcal{V}_{\text{H/H}}^{\text{nonb}}$, $\mathcal{V}_{\text{H/S}}^{\text{nonb}}$, and $\mathcal{V}_{\text{S/S}}^{\text{nonb}}$ are the CG potentials describing the non-bonded interactions between H beads, between H and S beads, and between S beads as a function of their separation distance, respectively; and N_{H} and N_{S} are the total number of H and S beads in the CG system, respectively.

The CG force field described by Eqs. (1.1)–(1.4) requires a total of 9 effective CG potentials to fully describe the energetics and conformational dynamics of the CG polyurea system. Next, we describe a procedure for deriving functional (or numerical) forms of these CG potentials, via a combination of atomistic and CG simulations.

1.2.1 Atomistic MD Simulations

The purpose of these simulations is to generate reference structural distributions of polyurea chains in the melt state for parameterizing the effective potentials of the CG model described above. Because simulations of full-length polymer systems are computationally prohibitive, CG potentials are usually derived from simulations of much shorter, oligomeric versions of the chains carried out at the same temperature and pressure. The assumption is that the potentials derived for shorter chains are transferable to full-length chains. In this study, we use short atomistic chains of polyurea containing a single repeating motif (atomistic H_2S_{14}) for generating the structural distributions.

We measure three types of structural distributions from our atomistic simulations. First, we collect distributions in bond lengths l, i.e., distances between virtual points

along the atomistic polymer chain representing the centers of adjacent beads in the CG model. There are three types of bonds in our CG system, so we obtain three sets of bond length distributions, denoted by $P_{\text{H-H}}(l)$, $P_{\text{H-S}}(l)$, and $P_{\text{S-S}}(l)$ for the H–H, H–S, and S–S bonds. These distributions are used to parameterize the bond stretching potentials $\mathcal{V}^{\text{str}}_{\text{H-H}}(l)$, $\mathcal{V}^{\text{str}}_{\text{H-S}}(l)$, and $\mathcal{V}^{\text{str}}_{\text{S-S}}(l)$ of our CG model. Second, we collect distributions in bond angles θ, i.e., the angles between points along the atomistic chain representing the centers of three adjacent beads in the CG model. We thus obtain three distributions, $P_{\text{H-H-S}}(\theta)$, $P_{\text{H-S-S}}(\theta)$, $P_{\text{S-S-S}}(\theta)$, corresponding to the three types of bond angles present in our CG chains, as defined by H–H–S, H–S–S, and S–S–S bead triplets. These three distributions will be used to parameterize the three CG bending potentials $\mathcal{V}^{\text{bend}}_{\text{H-H-S}}(\theta)$, $\mathcal{V}^{\text{bend}}_{\text{H-S-S}}(\theta)$, and $\mathcal{V}^{\text{bend}}_{\text{S-S-S}}(\theta)$. Finally, we gather radial distribution functions (RDFs) of distances r between pairs of points on the atomistic chains representing non-bonded centers of beads in the CG model. Three types of RDFs, namely, $g_{\text{H/H}}(r)$, $g_{\text{H/S}}(r)$, and $g_{\text{S/S}}(r)$, are collected corresponding to distributions in distances between non-bonded pairs of H beads, non-bonded H and S beads, and non-bonded pairs of S beads, respectively. These RDFs are used to parameterize the CG non-bonded potentials $\mathcal{V}^{\text{nonb}}_{\text{H/H}}(r)$, $\mathcal{V}^{\text{nonb}}_{\text{H/S}}(r)$, and $\mathcal{V}^{\text{nonb}}_{\text{S/S}}(r)$. We also measure distributions in the dihedral angle, as defined by four points along the atomistic chain representing the centers of four adjacent beads in the CG bead-chain. However, these distributions measured for the different kinds of bead quadruplets (e.g., H–H–S–S, H–S–S–S, etc) are quite flat, suggesting that a dihedral potentials might not be required in the CG force field of polyurea chains.

To perform MD simulations of the atomistic polyurea segments, we construct cubic simulation domains with edge lengths of 36.3 Å, each containing 20 randomly distributed chains of atomistic H_2S_{14} polyurea segments. For this purpose, we use the amorphous cell component within the Materials Studio environment [41]. Simulations

are carried out using the large-scale atomic/molecular massively parallel simulator (LAMMPS) package, developed at Sandia National Laboratories [42] to integrate atomic trajectories with a time step of 1 fs. The atomic interactions are governed by the Condensed-phase Optimized Molecular Potentials for Atomistic Simulations Studies (COMPASS) forcefield, a class II forcefield that is parameterized for a wide range of experimental measurements for organic compounds [43]; the functional form of class II potentials can be found in various sources [42, 44, 45]. Additionally, we use the particle-particle/particle-mesh (PPPM) approach in the LAMMPS kspace package[42] to calculate long-range Coulombic interactions.

To speed up equilibration of the initial randomly generated configurations, each atomistic system is equilibrated in a constant pressure-temperature (NPT) ensemble for 8 ns at an elevated temperature ($T = 500$ K) and atmospheric pressure and subsequently quenched to 300 K over a time span of 8 ns. The systems are then held for an additional 16 ns at ambient temperature and pressure ($T = 300$ K and $p = 1$ atm) so that the total simulation time for equilibration is 32 ns. Following equilibration, a production run of 1 ns is performed in the canonical (NVT) ensemble at $T = 300$ K for sampling pair, bond, and bond-angle structural distributions. To reduce the influence of the initial randomly generated state of each system the pair, bond, and bond-angle structural distributions are averaged from MD trajectories obtained from 15 different starting configurations. The average density over all runs is 1.068 g/cm^3, close to the experimentally measured density of polyurea. For calculating structural distributions, we use the carbon atom near the center of the backbone atoms of the relevant segments (H or S) as the CG bead centers.

For the IBI method to generate accurate CG potentials, proper equilibration of the atomistic systems is critically important. Figures 1.3a-c show the evolution of the radial distribution functions $g_{\mathrm{H/H}}(r)$, $g_{\mathrm{H/S}}(r)$ and $g_{\mathrm{S/S}}(r)$ for the three bead pairs

at various equilibration times. In particular, $g_{\mathrm{H/H}}(r)$ and $g_{\mathrm{H/S}}(r)$ undergo significant changes before approaching a stationary state at 32 ns of equilibration. The convergence of $g_{\mathrm{H/H}}(r)$ is more clearly shown by examining the time evolution of it's peak value (Figure 1.3d). As smaller peak values in the radial distribution functions will lead to weaker attractive energies in the effective CG models, sampling an insufficiently equilibrated all-atom system will lead to under-represented attractive forces between CG beads.

1.2.2 Iterative Boltzmann Inversion

We use the distributions $P_{\text{H-H}}(l)$, $P_{\text{H-S}}(l)$, and $P_{\text{S-S}}(l)$ measured from atomistic simulations to derive the CG bond-stretching potentials $\mathcal{V}^{\text{str}}_{\text{H-H}}(l)$, $\mathcal{V}^{\text{str}}_{\text{H-S}}(l)$, and $\mathcal{V}^{\text{str}}_{\text{S-S}}(l)$ via Boltzmann inversion:

$$\mathcal{V}^{\text{str}}_{x}(l) = -k_B T \ln\left[P_x(l)/l^2\right], \quad x \equiv \text{H-H, H-S, S-S} \tag{1.5}$$

where k_B is the Boltzmann constant and the l^2 term accounts for the degeneracy in the position of a bead located at a fixed distance l from another bead [46]. The potentials derived in this manner typically have a quadratic shape about their minimum, implying a harmonic underlying potential. Therefore, one can simply model the bond-stretching potential as a harmonic spring:

$$\mathcal{V}^{\text{str}}_{x}(l) \approx \frac{k_x}{2}\left(l - l_x\right)^2, \quad x \equiv \text{H-H, H-S, S-S} \tag{1.6}$$

where the effective bond stiffnesses $k_{\text{H-H}}$, $k_{\text{H-S}}$, and $k_{\text{S-S}}$ and equilibrium bond lengths $l_{\text{H-H}}$, $l_{\text{H-S}}$, and $l_{\text{S-S}}$ for the three types of bonds can be obtained fitting the potentials derived via Eq. (1.5) to the harmonic functions described in Eq. (1.6).

Similarly, one can directly derive the CG angle-bending potentials $\mathcal{V}^{\text{bend}}_{\text{H-H-S}}(\theta)$, $\mathcal{V}^{\text{bend}}_{\text{H-S-S}}(\theta)$, and $\mathcal{V}^{\text{bend}}_{\text{S-S-S}}(\theta)$ via Boltzmann inversion of the bending angle distributions

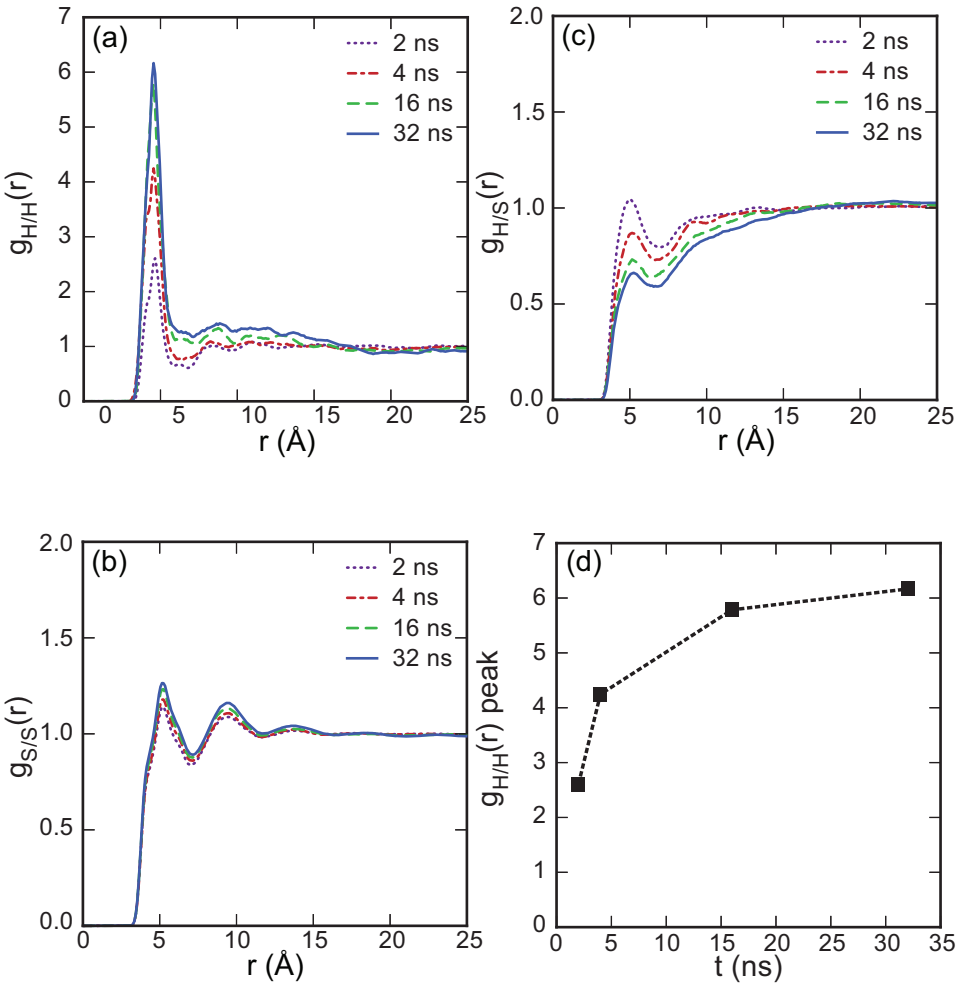

Figure 1.3: Evolution of radial distribution functions (a) $g_{\mathrm{H/H}}(r)$, (b) $g_{\mathrm{H/S}}(r)$, and (c) $g_{\mathrm{S/S}}(r)$, with equilibration time, and (d) convergence of the $g_{\mathrm{H/H}}(r)$ peak.

$P_{\text{H-H-S}}(\theta)$, $P_{\text{H-S-S}}(\theta)$, and $P_{\text{S-S-S}}(\theta)$ measured from atomistic simulations:

$$\mathcal{V}_x^{\text{bend}}(\theta) = -k_B T \ln\left[P_x(\theta)/\sin\theta\right], \quad x \equiv \text{H-H-S, H-S-S, S-S-S} \tag{1.7}$$

where the $\sin\theta$ term accounts for the degeneracy in the position of a bead subtending an angle θ with a bond. As in the case of bond lengths, the bending potential in

Eq. (7) can be approximated as a harmonic angular spring:

$$\mathcal{V}_x^{\text{bend}}(\theta) \approx \frac{k_x}{2}\left(\theta - \theta_x\right)^2, \quad x \equiv \text{H-H-S, H-S-S, S-S-S} \tag{1.8}$$

where the effective bending angle stiffnesses $k_{\text{H-H-S}}$, $k_{\text{H-S-S}}$, and $k_{\text{S-S-S}}$ and equilibrium bending angles $\theta_{\text{H-H-S}}$, $\theta_{\text{H-S-S}}$, and $\theta_{\text{S-S-S}}$ for the three types of bending angles can be obtained fitting the potentials derived via Eq. (1.7) to the functions described in Eq. (1.8).

The bond stretching and bending potentials derived from such direct Boltzmann inversion of bond length and angle distributions are usually good approximations of the true underlying potentials. The reason is that each distribution has a stiff, localized dependence on its corresponding order parameter (bond length or angle) and is therefore uncorrelated with other distributions. However, this is not true for non-bonded RDFs, which arise from softer potentials and include significant contributions from beads other than the pair of beads used in the RDF calculation (multibody effects), especially in condensed phases like polymer melts. Hence, direct Boltzmann inversion of the RDFs will *not* generally yield the correct nonbonded pair potentials.

To derive the true CG non-bonded pair potentials, we perform MD simulations of CG H_2S_{14} bead-chains at the same relevant densities and temperatures as the corresponding atomistic simulations. For the CG force field, we use initial guesses of the three CG non-bonded potentials obtained via Boltzmann inversion:

$$\mathcal{V}_{x,0}^{\text{nonb}}(r) = -k_B T \ln g_x(r), \quad x \equiv \text{H/H, H/S, S/S} \tag{1.9}$$

along with the set of six bond-stretching and bending potentials obtained via Eqs. (1.5-1.8). These CG MD simulations yield RDFs $g_{x,0}(r)$ that may differ from the target RDFs $g_x(r)$ obtained from atomistic simulations, where $x \equiv$ H/H, H/S, or S/S. Based on differences between the two sets of RDFs, the CG non-bonded potentials $\mathcal{V}_{x,0}^{\text{nonb}}(r)$

can be iteratively improved by the following correction:

$$\mathcal{V}^{\text{nonb}}_{x,i+1}(r) = \mathcal{V}^{\text{nonb}}_{x,i}(r) - \alpha k_B T \ln\left(\frac{g_{x,i}(r)}{g_x(r)}\right), \quad x \equiv \text{H/H, H/S, S/S} \tag{1.10}$$

where i stands for the iteration number and $\alpha < 1$ is a scaling factor that helps improve the convergence and stability of the IBI process. In general, the value of α is problem specific, however for the polyurea model, we find that a value of $\alpha = 0.05$ is sufficient for robust optimization of the potentials. This iterative procedure is continued until all non-bonded potentials converge to their limiting profiles, as denoted by $\mathcal{V}^{\text{nonb}}_{\text{H/H}}(r)$, $\mathcal{V}^{\text{nonb}}_{\text{H/S}}(r)$, and $\mathcal{V}^{\text{nonb}}_{\text{S/S}}(r)$. At this point, the CG simulations should yield the same RDFs as the targets $g_{\text{H/H}}(r)$, $g_{\text{H/S}}(r)$, and $g_{\text{S/S}}(r)$ obtained from the atomistic MD simulations. Even after matching the target RDFs, the pressures computed from the CG simulations might not match the target pressure. To resolve this potential issue, we modify the pressure by adding a linear term to the CG non-bonded pair potential after each iteration until we get the correct pressure [30, 47–49]:

$$\Delta\mathcal{V}_{\text{pc}}(r) = A k_B T \left(1 - \frac{r}{r_{\text{cut}}}\right) \tag{1.11}$$

where the value of A depends on the deviation from the target pressure.

Figure 1.4 summarizes our implementation of the IBI method. We begin by placing 150 H_2S_{14} CG bead-chains in random, non-overlapped configurations within a cubic simulation box of size commensurate with the target density. The initial bond lengths and angles of the chains are set equal to their respective equilibrium values obtained from Eqs. (1.6) and (1.8). Each IBI iteration step starts with a 0.8 ns equilibration step at 300 K. For the force field, we utilize the CG bond-stretching and bending potentials derived from atomistic simulations, Eqs. (1.6) and (1.8), along with the CG nonbonded potentials obtained from the previous iteration step, except for the first step where we use the direct Boltzmann inversion of the atomistic RDFs as an initial

guess for the nonbonded potentials. The equilibration step is followed by a cycle of pressure-correction steps. During this cycle, the CG system is held at $T = 300$ K in an NVT ensemble to compute a ensemble- and time-averaged pressure. This pressure is compared against the target pressure ($p = 1$ atm) so as to adjust the CG non-bonded potential according to Eq. (1.11). The pressure correction cycle is repeated until the computed CG pressure matches the target pressure, which is quite rapid and typically converges within 3–5 iterations. At this point, longer CG MD simulations (1.6 ns) are performed in the NVT ensemble at $T = 300$ K , using the pressure-corrected nonbonded potentials to compute the RDFs. These CG RDFs are compared against the atomistic RDFs to propose more accurate estimates of CG nonbonded potentials via Eq. (1.10). We iterate the IBI steps discussed above, inclusive of the pressure correction cycle, until the CG RDFs converge to the atomistic RDFs. As with the atomistic simulations, all CG MD simulation steps are performed using the LAMMPS software [50].

1.2.3 Model Validation

The utility of a CG model is measured by its ability to correctly predict structural and thermodynamic properties of the atomistic system that did not feature in the CG force field parameterization. We validate our CG model by comparing several of its properties, including the density, heat capacity, and stress relaxation spectrum against those computed from atomistic simulations.

Heat Capacity

The specific heat capacity C_{v} plays an important role in energy storage and dissipation. We compute the specific heat C_{v} of our polyurea systems from the fluctuation

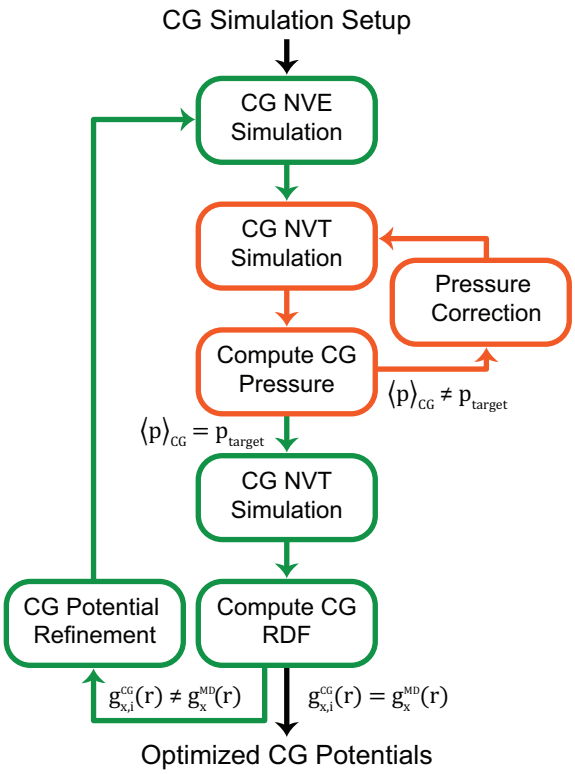

Figure 1.4: IBI implementation procedure.

in the total energy of the system in the NVT ensemble [51].

$$C_V = \left.\frac{\partial \langle E \rangle}{\partial T}\right|_V = \frac{\langle \delta E^2 \rangle}{k_B T^2} \tag{1.12}$$

where $\langle E \rangle$ and $\langle \delta E^2 \rangle$ are the mean value and variance of the total energy, respectively. Following Zhou et al. [52] we decompose the specific heat in terms of the kinetic and potential energy contributions as

$$C_V = \left.\frac{\partial \langle K \rangle}{\partial T}\right|_V + \left.\frac{\partial \langle U \rangle}{\partial T}\right|_V \tag{1.13}$$

From the equipartition theorem, $\langle K \rangle = \frac{3}{2} N k_B T$, and therefore

$$\frac{\partial \langle K \rangle}{\partial T} = \frac{3}{2} N k_B, \tag{1.14}$$

where N represents the number of atoms or CG beads in the system. This term represents the ideal heat capacity of the system. The remainder of the heat capacity

due to the interaction between particles can be formulated assuming that the potential energy follows the Boltzmann distribution.

$$\left.\frac{\partial \langle U \rangle}{\partial T}\right|_V = \frac{\langle \delta U^2 \rangle}{k_B T^2} + \frac{\langle \delta U \delta K \rangle}{k_B T^2} \tag{1.15}$$

where $\langle \delta U \delta K \rangle$ is the ensemble-averaged arises from the cross-correlation of potential energy and kinetic energy.

Diffusion Coefficient

The self-diffusion coefficient D_s characterizes the mobility of the polymer chains within the melt. We compute D_s of the center of mass of polyurea chains, both CG and atomistic, from the slope of the mean square displacement [46]:

$$D_\mathrm{s} = \lim_{t\to\infty} \frac{1}{6t} \left\langle |\mathbf{r}(t) - \mathbf{r}(0)|^2 \right\rangle \tag{1.16}$$

where t denotes time, $\mathbf{r}(t)$ is the position of the center of mass of the polymer chain i at time t, and $\langle \cdots \rangle$ denotes ensemble average of the quantity within the angular brackets over all chains in the simulation and reference positions $\mathbf{r}(0)$.

Stress Relaxation

The stress relaxation spectrum $G(t)$ is perhaps the most important quantity relevant to energy dissipation. We compute $G(t)$ from the stress autocorrelation function [53]:

$$G(t) = \frac{V}{k_B T} \langle \sigma_{xy}(t) \sigma_{xy}(0) \rangle \tag{1.17}$$

where σ_{xy} is the instantaneous shear stress computed from the virial theorem:

$$\sigma_{xy} = \frac{1}{V} \left[\sum_{i=1}^{N} m_i v_{ix} v_{iy} + \sum_{i=1}^{N-1} \sum_{j=i+1}^{N} r_{ijx} F_{ijy} \right] \tag{1.18}$$

where V is the volume of the simulation box; m_i, v_{ix}, and v_{iy} are the mass and x- and y-component velocities of bead i and j, respectively; and r_{ijx} and F_{ijy} are the

x-component separation distance and y-component force acting between beads i and j, respectively. Since the stresses σ_{xy}, σ_{xz}, and σ_{yz} are equivalent for an isotropic system, we use the average of the autocorrelations functions obtained from the three stresses to obtain smoother estimates of $G(t)$. We further smooth $G(t)$ by computing a running average over a window from $0.9t$ to $1.1t$. From $G(t)$ the frequency-dependent shear moduli are computed as [54]:

$$G'(\omega) = \omega \int_0^\infty G(t) \sin(\omega t)\, \mathrm{d}t \tag{1.19}$$

$$G''(\omega) = \omega \int_0^\infty G(t) \cos(\omega t)\, \mathrm{d}t \tag{1.20}$$

where $G'(\omega)$ represents the storage modulus and $G''(\omega)$ is the loss modulus.

1.2.4 Simulation Details

The above properties are computed for both the atomistic and CG systems using equilibrium MD simulations. In particular, we use *four* different monodisperse, short-chain systems in which the length of the polyurea chains varies from one to eight blocks—H_2S_{14}, $(H_2S_{14})_3$, $(H_2S_{14})_5$, and $(H_2S_{14})_8$. We also examine how well the CG model can predict properties of polyurea melts containing much longer chains, $(H_2S_{14})_{20}$. For the atomistic simulations, the number of chains in each system are varied to keep the net number of H_2S_{14} blocks fixed at 40, so that each system contains about 10,000 atoms. The simulations are performed with a time step of 1 fs. The fully atomistic systems are constructed in a random, non-overlapping configurations and annealed for 8 ns in the NPT ensemble at $T = 500$ K and $p = 1$ atm, followed by a decrease in temperature to 300 K for 8 ns, and equilibrated at 300 K for 16 ns. Thereafter, the equilibrated systems are simulated in the NVT ensemble at 300 K for 100 ns. The MD simulations of the corresponding CG chains are equilibrated at NPT ensemble at 300 K for 250 ns because of the limited temperature transferability

of CG potentials, however this simpler equilibration is sufficient due to their faster dynamics. The number of polyurea blocks is also increased to 500 for the CG systems and the integration time step is increased to 25 fs. For each simulation, the densities, heat capacities, and stress relaxation profiles are computed from the atomic/CG bead positions and velocities to test how well the CG model reproduced these properties in comparison to the corresponding fully atomistic MD simulations.

1.2.5 Model Parameterization

As discussed in the previous section, nine different structural distributions were computed from atomistic MD simulations of short-chain polyurea systems (H_2S_{14}) in the melt state at atmospheric conditions. Figure 1.5 presents the bond length distributions $P_{\text{H-H}}(l)$, $P_{\text{H-S}}(l)$, and $P_{\text{S-S}}(l)$ computed from these simulations. All three distributions exhibit a typical Gaussian shape, suggesting that the underlying bond-stretching potentials can indeed be modeled as harmonic springs. Figure 1.6 shows the Boltzmann-inverted estimates of the underlying bond-stretching potential $\mathcal{V}^{str}_{\text{H-H}}(l)$, $\mathcal{V}^{str}_{\text{H-S}}(l)$, and $\mathcal{V}^{str}_{\text{S-S}}(l)$ obtained via Eq. (1.5). Also shown in the same plots are the excellent fits to these potentials using the harmonic equation presented in Eq. (1.6), with the exception of the *S-S* bond length distribution that has a minor second peak due to two torsional conformations. While the harmonic bond approximation does not allow the CG model to reproduce this double-peaked bond length distribution, this has a negligible effect on the structural and thermodynamic properties of the CG system. The resulting fits yield the effective bond stiffnesses and equilibrium bond lengths tabulated in Table 1.1. These values indicate that the *S-S* bonds are the shortest while the *H-S* bonds are the stiffest, while the *H-H* bonds are the longest and softest, clearly due to the smaller size of the *S* segments.

Figure 1.7 shows the bending angle distributions $P_{\text{H-H-S}}(\theta)$, $P_{\text{H-S-S}}(\theta)$, and $P_{\text{S-S-S}}(\theta)$

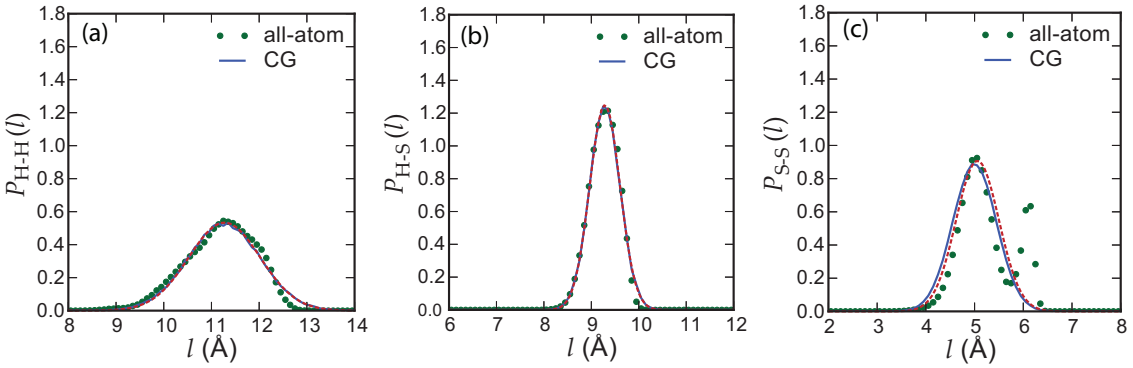

Figure 1.5: Bond length distributions (a) $P_{\text{H-H}}(l)$, (b) $P_{\text{H-S}}(l)$, and (c) $P_{\text{S-S}}(l)$ obtained from atomistic MD simulations and from CG MD simulation after IBI convergence. The dashed line shows a weighted Gaussian fit to the bond distributions obtained from atomistic MD simulations.

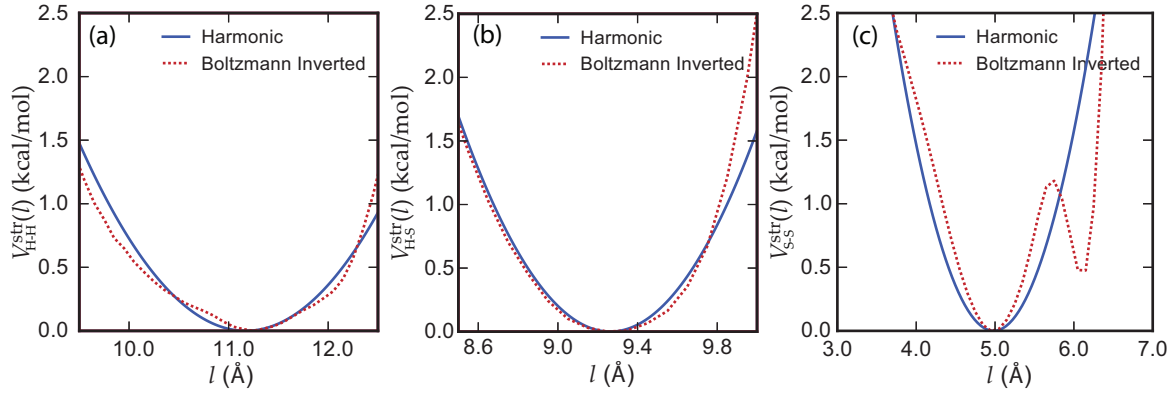

Figure 1.6: Bond-stretching potentials (a) $\mathcal{V}^{\text{str}}_{\text{H-H}}(l)$, (b) $\mathcal{V}^{\text{str}}_{\text{H-S}}(l)$, and (c) $\mathcal{V}^{\text{str}}_{\text{S-S}}(l)$ obtained from Boltzmann inversion of bond length distributions and from harmonic approximation based on fitted parameters summarized in Table 1.1.

measured from atomistic simulations. Boltzmann-inverting the distributions via Eq. (1.8) yields the effective bending potentials $\mathcal{V}^{bend}_{\text{H-H-S}}(\theta)$, $\mathcal{V}^{bend}_{\text{H-S-S}}(\theta)$, and $\mathcal{V}^{bend}_{\text{S-S-S}}(\theta)$, which are plotted in Figure 1.8. The potentials exhibit a harmonic shape, though somewhat less harmonic than the bond stretching potentials. Nonetheless, fitting the potentials to the harmonic function in Eq. (1.8) yields the parameters tabulated in Table 1.1.

Bond type	Bond Length (Å)	Stiffness (kcal/mol/Å^2)
H–H	11.17	1.05
H–S	9.26	5.82
S–S	4.98	3.03
Angle type	**Angle (degrees)**	**Stiffness (kcal/mol/rad^2)**
H-H-S	128.4°	1.60
H-S-S	134.5°	0.76
S-S-S	169.5°	0.64

Table 1.1: Summary of bond and angle parameters for CG model of polyurea

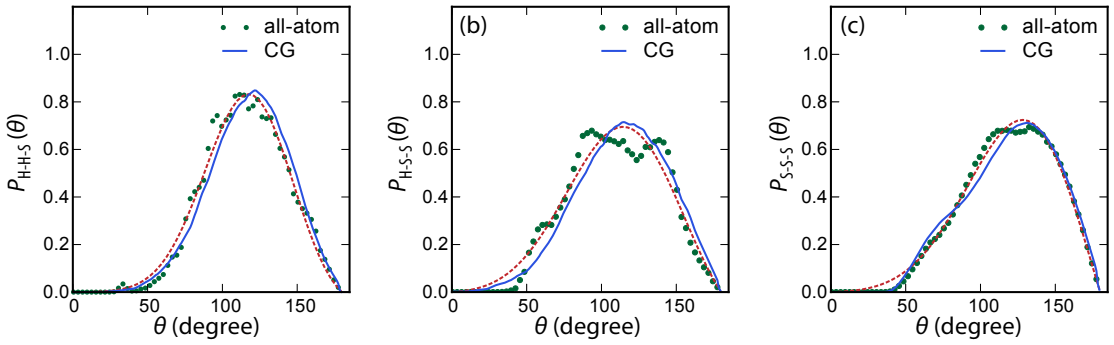

Figure 1.7: Bending angle distributions (*a*) $P_{\text{H-H-S}}(\theta)$, (*b*) $P_{\text{H-S-S}}(\theta)$, and (*c*) $P_{\text{S-S-S}}(\theta)$ obtained from all-atom MD simulations and from CG MD simulations after IBI convergence. The dashed line shows a weighted Gaussian fit to the all-atom angle distributions via Eq. (1.7) and (1.8).

Figure 1.9 shows the RDFs $g_{\text{H/H}}(r)$, $g_{\text{H/S}}(r)$, and $g_{\text{S/S}}(r)$ corresponding to the three types of non-bonded pairwise interactions, as computed from the atomistic MD

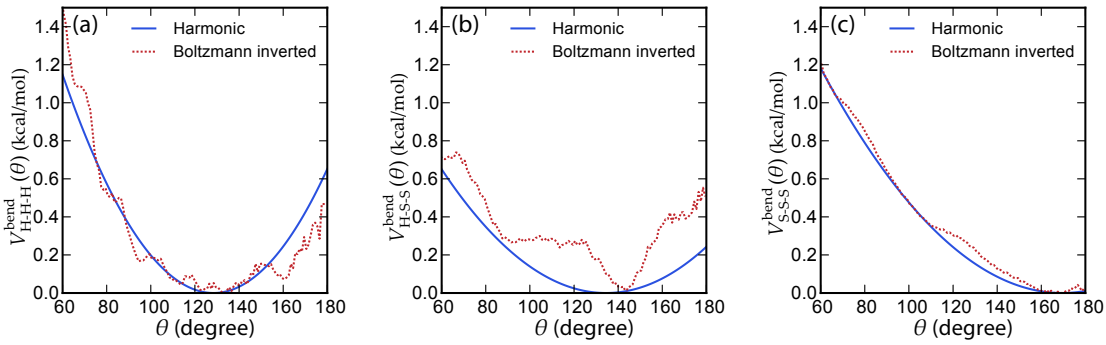

Figure 1.8: Bending angle potentials (*a*) $\mathcal{V}^{\text{bend}}_{\text{H-H-S}}(\theta)$, (*b*) $\mathcal{V}^{\text{bend}}_{\text{H-S-S}}(\theta)$, and (*c*) $\mathcal{V}^{\text{bend}}_{\text{S-S-S}}(\theta)$ obtained from Boltzmann inversion of bending angle distributions and from harmonic approximation based on the fitted parameters summarized in Table 1.1. The Boltzmann inverted potential is shifted by an arbitrary constant so that its minimum value is zero energy. Note that this shift plays no role in determining the structure and dynamics of the CG system

simulations. All three RDFs exhibit a discernible peak at short separation distances. As expected, $g_{\text{H/H}}(r)$ displays the highest peak, indicating strong aggregation of hard segments into hard domains due to π-stacking of the aromatic rings and hydrogen bonding between the urea linkages; in contrast, $g_{\text{S/S}}(r)$ and $g_{\text{H/S}}(r)$ display much smaller peaks, suggesting weaker interactions between soft segments and between soft and hard segments, respectively. We also observe some modulations in the RDFs beyond these first peaks, implying higher-order caging effects. However, these modulations decay quickly, and by $r \geq 22$ Å for $g_{\text{H/H}}(r)$ and $r \geq 16$ Å for both $g_{\text{H/S}}(r)$ and $g_{\text{S/S}}(r)$, plateau to their nominal bulk value of 1.

To derive the CG nonbonded potentials $\mathcal{V}^{\text{nonb}}_{\text{H/H}}(r)$, $\mathcal{V}^{\text{nonb}}_{\text{H/S}}(r)$, and $\mathcal{V}^{\text{nonb}}_{\text{S/S}}(r)$, we use the above RDFs to obtain initial guesses of the nonbonded potentials via Eq. (1.10). We then use these guesses along with the bond-stretching and bending potentials derived earlier to initiate the IBI procedure. In Figure 1.9 we compare the RDFs

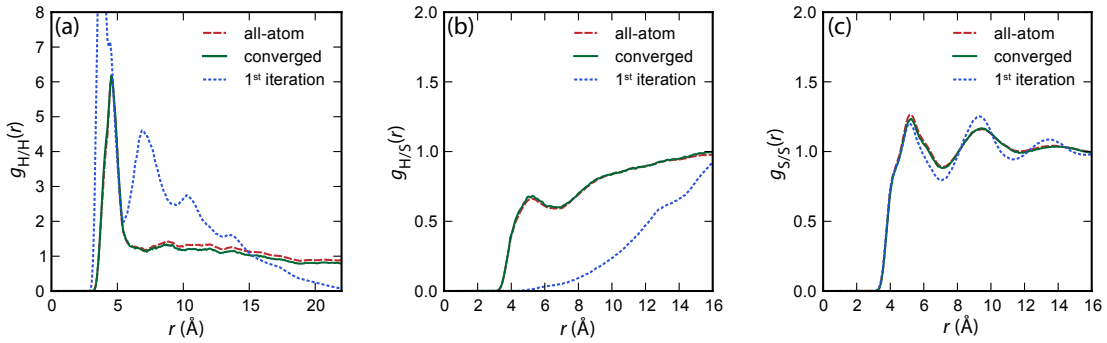

Figure 1.9: Radial distribution functions (a) $g_{\mathrm{H/H}}(r)$, (b) $g_{\mathrm{H/S}}(r)$, and (c) $g_{\mathrm{S/S}}(r)$ obtained from all-atom MD simulations, CG MD simulations after IBI convergence and CG MD simulations during the 1st IBI iteration, i.e., based on the initial guess potential obtained from Boltzmann inversion the all-atom MD RDFs.

computed from CG MD simulations $g_{\mathrm{H/H},i}$, $g_{\mathrm{H/S},i}$, and $g_{\mathrm{S/S},i}$ after the first IBI iteration ($i = 1$), and after convergence against the target RDFs obtained from atomistic simulations. It can be observed that the IBI procedure implemented here leads to converged RDFs for all three types of nonbonded interactions within 80 iterations. We also note that amongst the three RDFs, those corresponding to S/S interactions converge the fastest (within 10 iterations) while those corresponding to H/H interactions converge the slowest because of the phase segregation between hard and soft segments of polyurea. As a result structural distribution from CG MD simulation from H/H and H/S pair interaction observed to be interdependent with large entropic contribution.

The final, converged CG nonbonded potentials $\mathcal{V}^{\mathrm{nonb}}_{\mathrm{H/H}}(r)$, $\mathcal{V}^{\mathrm{nonb}}_{\mathrm{H/S}}(r)$, and $\mathcal{V}^{\mathrm{nonb}}_{\mathrm{S/S}}(r)$ are plotted in Figure 1.10. We observe that $\mathcal{V}^{\mathrm{nonb}}_{\mathrm{H/H}}(r)$ exhibits a much deeper energy minimum ($\sim 1k_BT$) than the other two nonbonded potentials ($<< 1k_BT$). Clearly, it is this difference in the interactions of hard and soft segments that is responsible for the microphase separation observed in polyurea systems. We have also plotted

in the same figure the initial guesses for the nonbonded potentials, as obtained from Boltzmann-inversion. The converged nonbonded potentials are clearly very different from the initial guesses, which emphasizes the importance of the IBI procedure in deriving correct nonbonded interaction potentials. These differences also aptly illustrate the distinction between a pairwise potential energy, as captured by the converged potentials $\mathcal{V}_x^{\text{nonb}}(r)$, and a potential of mean force (or free energy), as captured by the initial guesses $\mathcal{V}_{x,0}^{\text{nonb}}(r)$.

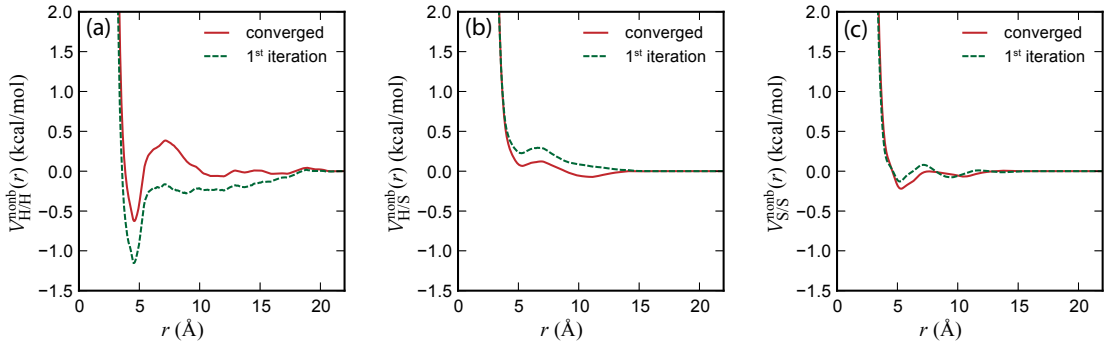

Figure 1.10: Nonbonded potentials (a) $\mathcal{V}_{\text{H/H}}^{\text{nonb}}(r)$, (b) $\mathcal{V}_{\text{H/S}}^{\text{nonb}}(r)$, and (c) $\mathcal{V}_{\text{S/S}}^{\text{nonb}}(r)$. obtained from convergence of the IBI method compared against those used in the 1st IBI iteration (i.e., obtained from Boltzmann inversion of the all-atom RDFs).

Our current IBI procedure of *simultaneously* optimizing the CG nonbonded potentials $\mathcal{V}_{\text{H/H}}^{\text{nonb}}(r)$, $\mathcal{V}_{\text{H/S}}^{\text{nonb}}(r)$, and $\mathcal{V}_{\text{S/S}}^{\text{nonb}}(r)$ seems to work efficiently and robustly. We also attempted a slightly different scheme for deriving the CG nonbonded potentials involving *sequential* optimization of the potentials. In this sequential scheme, we first derived $\mathcal{V}_{\text{S/S}}^{\text{nonb}}(r)$ by implementing IBI on S_{14} chains, using the bonded potentials $\mathcal{V}_{\text{S-S}}^{\text{str}}(r)$ and $\mathcal{V}_{\text{S-S-S}}^{\text{bend}}(r)$ derived earlier. Next, we derived $\mathcal{V}_{\text{H/H}}^{\text{nonb}}(r)$ by implementing IBI on H_2 dimers, using the bonded potential $\mathcal{V}_{\text{H-H}}^{\text{str}}(r)$ derived earlier. Finally, $\mathcal{V}_{\text{H/S}}^{\text{nonb}}(r)$ was derived by implementing IBI on H_2S_{14} chains using the two non-bonded CG potentials and six bonded CG potentials derived earlier. We find that while this

scheme yields similar estimates of $\mathcal{V}_{\mathrm{S/S}}^{\mathrm{nonb}}(r)$ as those obtained from simultaneous IBI optimization, the IBI step for deriving $\mathcal{V}_{\mathrm{H/H}}^{\mathrm{nonb}}(r)$, and $\mathcal{V}_{\mathrm{H/S}}^{\mathrm{nonb}}(r)$ was generally unstable and failed to converge because sequential optimization scheme is best suitable for the polymers where structural distribution of each pair interaction sites is independent of each other while this is not the case for heterogeneous systems. Thus, we suggest that simultaneous IBI optimization, as opposed to sequential optimization, is perhaps the most efficient strategy for deriving CG nonbonded potentials of heterogeneous systems composed of more than one type of bead.

1.2.6 Model Verification

To validate the 2-bead CG model of polyurea developed above, we have computed several thermophysical and structural properties of short-chain polyurea systems using the CG model and compared the properties against those computed from fully atomistic models. As mentioned earlier, we carry out this comparison for four different systems, each containing polyurea chains of different lengths: $(H_2S_{14})_n$, where $n = 1, 3, 5$ and 8. Due to the computational expense in generating equilibrium configurations with all-atom models, only the 1-block polyurea end-to-end distribution, morphology, stress relaxation spectra, and dynamic scaling factor are computed as verification of the CG model.

We begin by comparing the average densities ρ and constant-volume heat capacities C_{v} computed from the CG and atomistic models for the four different polyurea systems, which are plotted in Figure 1.11 as a function of chain length. Each atomistic model was simulated with a single system due to the large computational expense to equilibrate all-atom systems. For the CG models, five different replica systems were simulated and the results averaged to produce the predicted density and heat capacity

values. The standard deviation of the density predictions was less than 0.1%, while for the heat capacity, the standard deviation was less than 1%.

We observe an increase in density with increasing chain length for both the CG and atomistic systems, although the CG models exhibit a larger increase, particularly at the transition from one to two block chains. The largest difference in the predicted density is seen for the 8 block system, where the disparity is 4.4%. The density of polyurea reported by Amini et al [55] is 1.1 g/cm^3 for a molecular weight consistent with a 20 block chain is plotted with an asterisk as a reference.

Comparison of the computed heat capacity between atomistic and CG models via Eqs. (1.14) and (1.15) is less straightforward as the thermodynamic temperature of the system explicitly depends on the number of degrees of freedom in the system. As the CG models contain significantly fewer degrees of freedom per unit volume, their computed heat capacities are proportionally lower. A single block (H_2S_{14}) of polyurea contains 246 atoms or 16 CG beads with the previously described mapping, leading to a scaling factor of C_k=15.375 for the ideal heat capacity of the system. For the non-ideal components, we compare the ratio of the fluctuation terms $\langle \delta U^2 \rangle$ and $\langle \delta U \delta K \rangle$ between the CG and all-atom MD simulations of single block systems to empirically determine scaling factors of C_u=9.30, and C_{uk}=26.67, respectively, with the assumption that the partitioning of energy between the coarse-scale energy fluctuations observed in the CG system and the averaged-out fine scale fluctuations is invariant to molecular weight. Figure 1.11(b) shows the predicted heat capacities from atomistic and CG simulations with these scaling factors applied via Eq. 1.21 for the CG values:

$$C_V = \frac{3}{2} C_k N_{CG} k_B + \frac{C_u \langle \delta U_{CG}^2 \rangle}{k_B T^2} + \frac{C_{uk} \langle \delta U_{CG} \delta K_{CG} \rangle}{k_B T^2} \tag{1.21}$$

where N_{CG} represents the number of CG beads in the system, $\langle \delta U_{CG}^2 \rangle$ is the variance

of CG potential energy, and $\langle \delta U_{CG} \delta K_{CG} \rangle$ is the ensemble averaged arises from the cross correlation of CG potential energy and CG kinetic energy. The sensitivity of the chain length to the heat capacity is somewhat exaggerated in the CG model, however comparison to an experimentally measured value for polyurea of 1.977 $JK^{-1}cm^{-3}$ is quite reasonable[16].

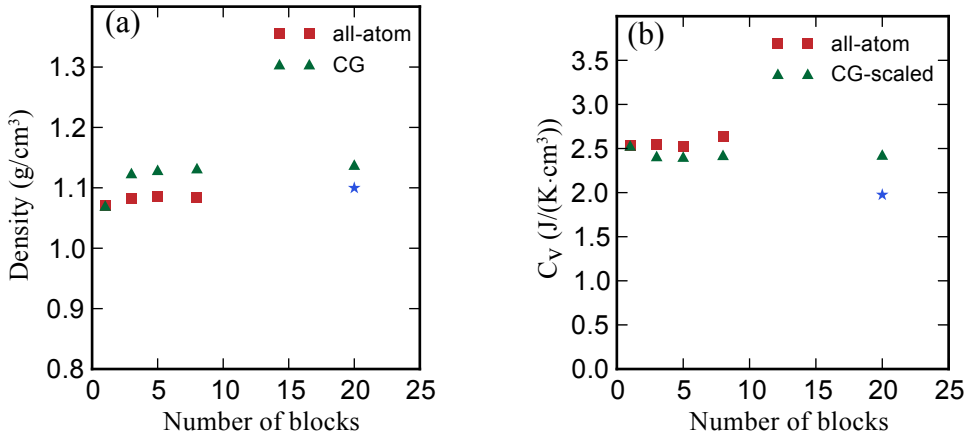

Figure 1.11: Comparison of (a) density and (b) heat capacity between all-atom MD simulations and CG simulations for oligomeric polyurea of varying chain lengths. Experimental values are denoted with asterisks.

Next, we compare the *global* structure of the polyurea systems computed using CG and atomistic models, in terms of chain conformations and overall morphology of the system. No attempt is made to compare the *local* structure from the CG and atomistic models because the IBI parameterization automatically leads to preservation of the local structure of the atomistic system, as noted by the excellent match between the CG and atomistic RDFs (Figure 1.9). We characterize chain conformations in terms of the distribution of chain end-to-end distances $P(d_{\text{ee}})$, where the end-to-end distance $d_{\text{ee}} \equiv |\mathbf{r}_{\text{N}}(t) - \mathbf{r}_1(t)|$. We also qualitatively characterize the overall morphology in terms of the size and shape of microphase-separated domains.

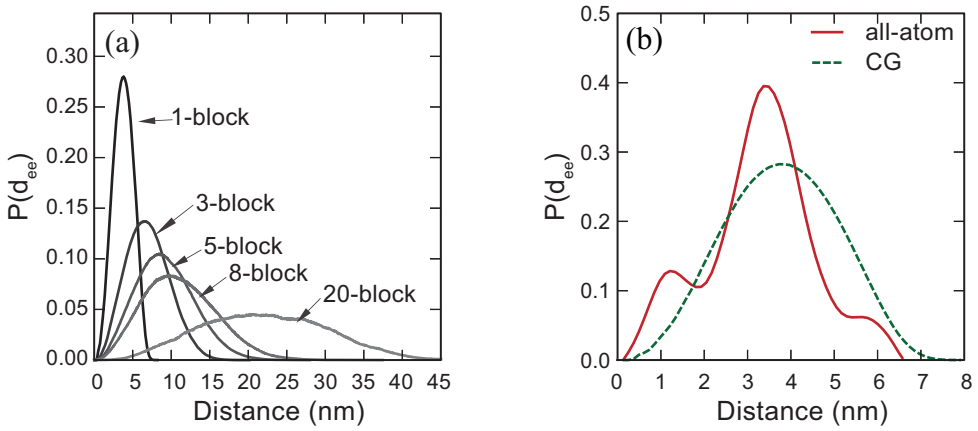

Figure 1.12: (a) Predicted distributions of chain end-to-end distances $P(d_{\text{ee}})$ from CG MD simulations with increasing chain lengths, and (b) Comparison of $P(d_{\text{ee}})$ for 1-block systems obtained from all-atom MD and CG MD simulations.

To characterize the effect of the chain length on end-to-end distances in polyurea, five different CG systems of increasing chain length are simulated, with the results shown in Figure 1.12(a). Due to the computational expense in generating equilibrium configurations with all-atom models, only 1-block polyurea end-to-end distribution is computed as verification of the CG model, which is shown in Figure 1.12(b). Due to the slow diffusion in the atomistic system, the end-to-end distributions deviate very slowly from their initial state, and therefore sufficient sampling is challenging even for this short short-chain system. Table 1.2 summarizes the calculated expected value $\langle d_{\text{ee}} \rangle$ for different CG systems and the single-block fully-atomistic system showing reasonable agreement between the CG and all-atom systems for the 1-block polyurea chains. The dependence of the average end-to-end distance with chain length follows a power law with an exponent of 0.577 consistent with the theoretical scaling of 0.588 obtained for three-dimensional random walk chains in good solvent[56].

To characterize the phase morphology of polyurea, we simulate $(H_2S_{14})_1$ and $(H_2S_{14})_{20}$ CG polyurea systems containing 128,000 beads in a cubic simulation box

# Blocks	all-atom(nm)	CG(nm)
1	3.13	3.79
3	-	6.99
5	-	9.28
8	-	11.19
20	-	22.17

Table 1.2: Summary of expected value $\langle d_{ee} \rangle$ for different CG and all-atom MD systems.

that has an edge length of 26.5 nm. As a comparison, we also simulate a fully-atomistic system containing 160 1-block chains, equivalent to 2,560 CG beads, in a 7.2 nm cubic simulation box. Figure 1.13a shows the initially random configuration of the single block CG system. After 200 ns of simulation time, the resulting microstructures for the $(H_2S_{14})_1$ and $(H_2S_{14})_{20}$ systems can be seen in Figures 1.13b-c. The initial and final states of the atomistic system are shown in Figures 1.13d-e. The atomistic system is equilibrated for only 32 ns, but at elevated temperatures as previously described.

To more quantitatively compare the morphology of the CG and all-atom systems, and to investigate the effect of the number of blocks, we computed the number and sizes of segregated hard domains for single block and 20 block CG systems. Clusters are identified by grouping all neighboring hard beads with a neighbor threshold distance of 7.5 Å. A clear difference between the morphology of the $(H_2S_{14})_1$ and $(H_2S_{14})_{20}$ systems can be observed as the single block polyurea chains tend to aggregate into a fewer number of larger clusters as observed by Arman et al.[53] These results are plotted in Figure 1.14 for the CG systems. Since the fully-atomistic sim-

ulation box contains only 2% of the volume of the CG simulation box, quantitative analysis of the number and size of the segregated hard domains is not meaningful, although qualitatively, the clustering of hard domain segments is similar to the CG models. Moreover, Fully atomistic simulations of phase segregation in polyurea for quantitative predictions would require prohibitive computational effort.

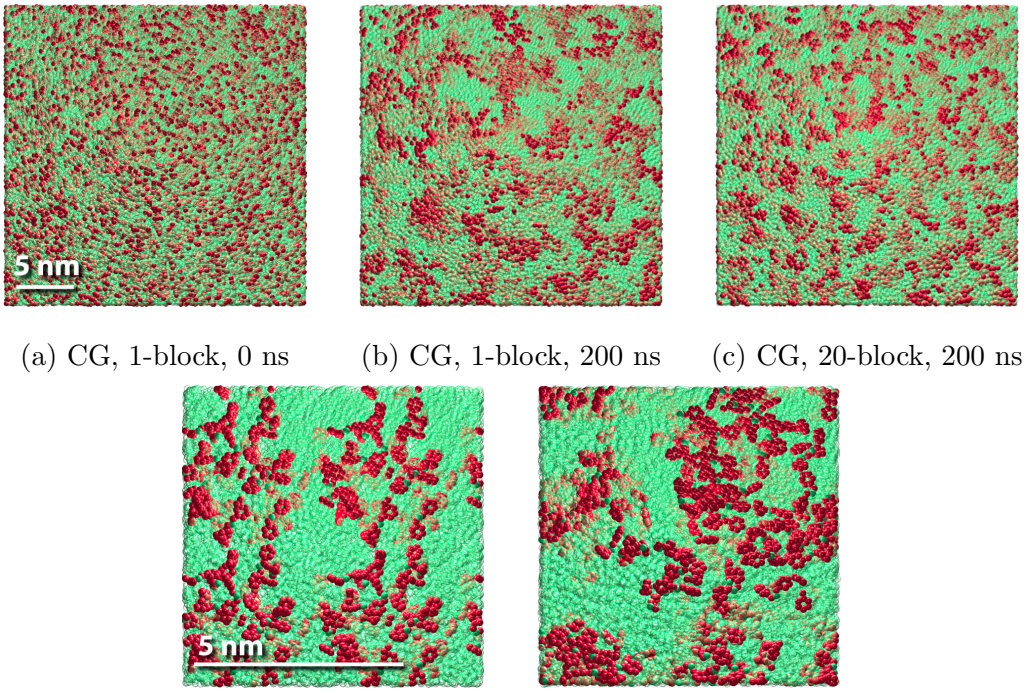

(a) CG, 1-block, 0 ns (b) CG, 1-block, 200 ns (c) CG, 20-block, 200 ns

(d) all-atom, 1-block, 0 ns (e) all-atom, 1-block, 32 ns

Figure 1.13: Morphologies of CG and all-atom polyurea systems before and at the end of the simulation runs: (a) initial and (b) final morphology of 1-block CG chains; (c) final morphology of 20-block CG chains; and (d) initial and (e) final morphology of 1-block all-atom chains. Red points represents the hard segments while green points represents the soft segments.

Finally, we compare the stress relaxation function $G(t)$ from a one block system computed from both the CG and atomistic models. Since the stress relaxation function computed directly from the autocorrelation of the virial stress via Eq. (1.17) is

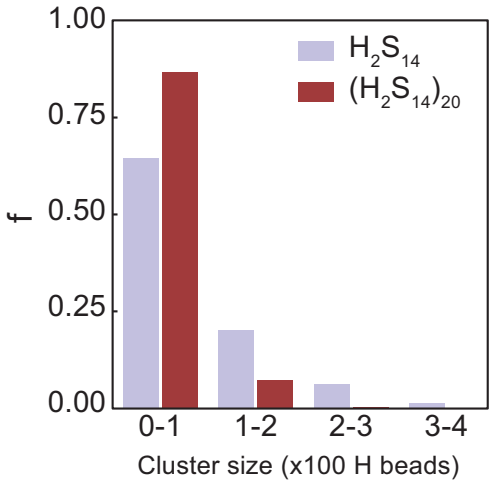

Figure 1.14: Size distribution of hard domains in terms of the fraction of H beads within each domain for H_2S_{14} and $(H_2S_{14})_{20}$.

highly noisy, we take running averages of the raw $G(t)$ between $0.9t$ and $1.1t$, consistent with previous studies [54]. Furthermore, the time axis of the CG stress relaxation function must be rescaled to account for the faster dynamics of the CG system due to its smoothed energy landscape and reduced frictional forces acting between molecules. While several authors have suggested the use of a constant scaling factor related to the ratio of self-diffusivities[57, 58], we find that this is insufficient to match the profile of the stress relaxation function between the CG and all-atom models. Instead we observe that the ratio in the mean square displacement between the two systems is not constant, starting at a value near unity and increasing until reaching an asymptotic value after 100 ns. This trend suggests that at extremely short time spans, the diffusion of the system is limited only by the available thermal energy and momenta of the atoms, and not until longer time scales is motion limited by frictional forces. Figure 1.15a shows the ratio of mean square displacements from the CG and all-atom MD systems fitted to a time-dependent dynamic rescaling function $f_t(t)$, defined as

$$f_t(t) = 1 + a(1 - e^{-t/\tau}), \tag{1.22}$$

where the constants $a = 8,731$ and $\tau = 23.8$ ns reflect the long time scale scaling constant and transition time, respectively. Thus, the relaxation spectrum for the CG model is rescaled as

$$G(t) = G_{CG}(t_{CG} \times f_t(t_{CG})). \tag{1.23}$$

Figure 1.15b compares the rescaled CG relaxation spectrum for $(H_2S_{14})_1$ with all-atom MD simulation. At very short time scales, ($t \leq 10$ ps), the stress relaxation function of the all-atom system decays much faster than that of the CG system because some of the atomic-scale relaxation mechanisms, such as damped oscillations of collective bond and bending angle vibrations, are not represented in the CG model. At intermediate time scales (10 ps $\leq t \leq$ 1 ns) the agreement between the two models is excellent. Beyond 1 ns sufficient sampling of the all-atom MD model becomes increasing computationally expensive and the autocorrelation of the stress decays rapidly with insufficient sampling. However, the efficiency of the CG model allows for sufficient sampling well past 1000 ns, far beyond the practical range of all-atom MD simulations.

1.3 5-Bead CG model of Polyurea

The 2-bead CG model of polyurea can predict realistic phase segregation in polyurea, however, due to the large size of the H beads, the two bead model exhibits topology violations that manifest as unphysical bond crossings between H beads. These bond crossings can occur because the excluded volume of the H bead from the repulsive part of the pair potential is too small compared with the bond length between H beads. These unphysical bond crossings cause the CG system to relax more rapidly as entanglements can be spuriously broken, which results in incorrect scaling of relaxation times with molecular weight.

For soft-core potentials such as those utilized in dissipative particle dynamics, a

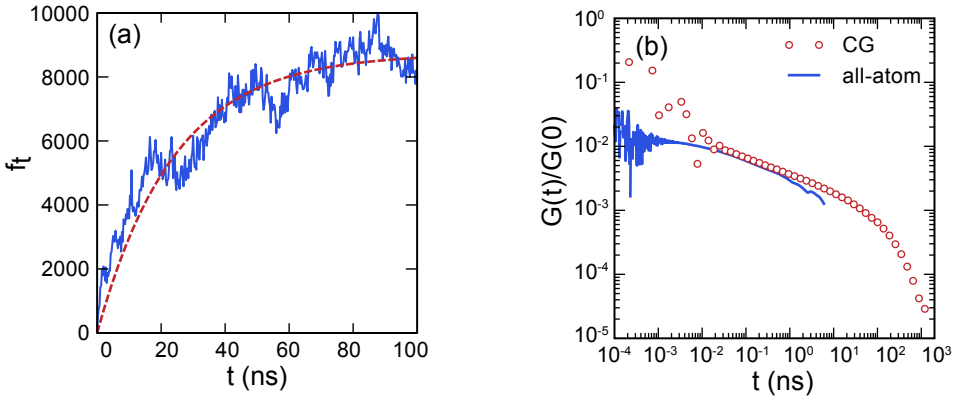

Figure 1.15: (a) Dynamic scaling factor f_{t} for $(H_2S_{14})_1$ system; the dashed line shows the exponential fit of f_{t}, and (b) comparison of all-atom MD and scaled CG stress relaxation spectra $G(t)/G(0)$ for $(H_2S_{14})_1$.

corrective bond-bond repulsion potential was developed by Kumar et al. [59], and later modified by Sirk et al. [60]. Sliozberg et al. [61] compared hard-core potentials, such as the Kremer-Grest model, with combined soft-core potentials augmented with bond-bond repulsion and determined that the soft-core potentials were more efficient at representing a chain with a fixed number of entanglements for a simple model polymer system, i.e. no attempt was made to match the short-range structural distributions of a specific polymer.

We develop 5-bead CG model of polyurea for preventing bond crossings by utilizing a finer CG mapping for the hard segments of polyurea, by splitting symmetric halves of hard segment into four different types of CG beads, each of similar size. In this new model, A and B bead types are mapped to the aromatic groups within the hard segment, a U bead type corresponds to the urea linkage, and a C bead type represents the ester group connecting the hard and soft segments. Figure 1.16 shows the mapping scheme in detail. The resulting bead-chain is denoted as $(\mathrm{S}_{13}\mathrm{CAUBBUAC})_n$

or $(S_{13}H_2)_n$, where H represents a (CAUB) bead motif, and n denotes the number of times the $S_{13}H_2$ block is repeated.

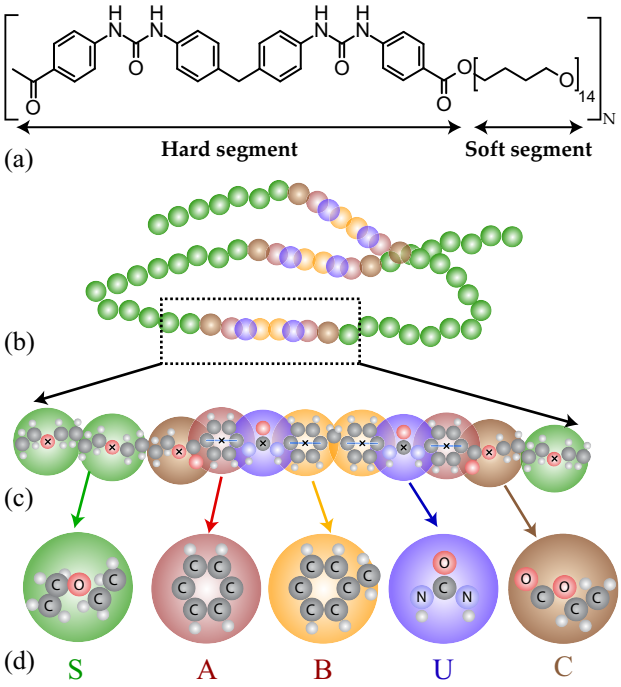

Figure 1.16: 5-bead CG polyurea model: (a) chemical structure of the repeated block making up polyurea chains, (b) representation of a polyurea chain composed of CG beads, (c) CG mapping within the hard and soft segments of polyurea; crosses represent bead coordinates used in computing structural distributions, and (d) chemical structure of each bead type.

1.3.1 Model Parameterization

Each CG bead has a mass equal to the total mass of its constituent atoms, summarized in Table 1.3. The total potential energy of the CG model consists of three terms: bond energies between adjacent beads along the bead-chain, angle bending energies associated with angles subtended by consecutive bonds, and non-bonded interactions between all pairs of beads, excluding pairs connected by a bond. The total bond

energy is calculated as the sum of stretching energies of all six types of bonds present in the CG system. Similarly, the net bending energy has contributions arising from the six types of bond angles present in the CG model. Lastly, the total non-bonded energy is calculated as the sum of all possible non-bonded interactions in between and across the five different beads in the CG system. The energies of each bond and angle are modeled by the harmonic potentials

$$\mathcal{V}_{\text{str}}(l) = \frac{k}{2}\left(l - l_0\right)^2 \tag{1.24}$$
$$\mathcal{V}_{\text{bend}}(\theta) = \frac{k}{2}\left(\theta - \theta_0\right)^2$$

where k and l_0 are the stiffness and equilibrium length for each bond, and likewise, k and θ_0 are the stiffness and equilibrium angle for each angle. These parameters are determined by fitting quadratic functions to the Boltzmann inversion of the bond length and bond angle distributions. Table 1.4 summarizes the bond and angle parameters, computed from bond lengths and angle distributions sampled from atomistic MD simulations.

Bead type	Molecular weight g/mol
A	76.09
B	83.11
C	72.05
S	72.10
U	58.03

Table 1.3: Summary of molecular weights assigned to each type of bead.

To parametrize the effective potentials of the CG polyurea model, structural dis-

Bond type	l_0 (Å)	K (kcal/mol/Å^2)
A-C	3.62	141.34
A-U	3.80	111.30
B-B	4.89	25.30
B-U	3.81	116.52
C-S	4.90	3.52
S-S	4.95	3.77
Angle type	**θ_0 (deg)**	**K (kcal/mol/rad^2)**
A-C-S	135.0	4.25
A-U-B	117.4	63.52
B-B-U	149.8	7.99
C-A-U	162.2	9.64
C-S-S	139.9	1.55
S-S-S	143.9	1.60

Table 1.4: Summary of bond and angle parameters for the CG model of polyurea.

tributions of short oligomeric polyurea chains are generated from atomistic MD simulations. Details of the atomistic MD simulations are described in previous section. The average density from atomistic MD simulations is 1.0713 g/cm^3, 3.6% higher than the experimentally measured density. The structural distributions are computed at virtual sites of the CG beads. The virtual sites for each bead are shown in Figure 1.16c, denoted by a cross symbol. The virtual sites of the aromatic groups are taken at the midpoint of the 1,3 carbon atoms in each ring.

The CG system is composed of 75 bead-chains ($S_6H_2S_7$) arranged in a random,

non-overlapped configuration within a cubic simulation box of size commensurate with the target density. The initial bond lengths and angles of the chains are set equal to their respective equilibrium values as shown in Table 1.4. The IBI method is then performed until a convergence criterion is satisfied. The error of each interaction is computed as the L^2-norm of the difference between the CG and target atomistic radial distribution functions normalized by the L^2-norm of the target distribution function,

$$e_{L_2} = \left(\frac{\int \left[g^{\mathrm{CG}}(r) - g^{\mathrm{target}}(r) \right]^2 dr}{\int \left[g^{\mathrm{target}}(r) \right]^2 dr} \right)^{1/2} \tag{1.25}$$

The convergence criterion is defined such that the iteration is completed when the maximum error computed over each of the 15 unique pair types is less than a value of 0.05. The converged, tabulated potentials and input scripts for both all-atom and CG models can be found in the supplementary material.

In Fig. 1.17a-o, radial density functions (RDFs) of all 15 unique pair combinations sampled from coarse-grained MD simulations are compared with those sampled from all-atom MD simulations. The distributions based on the initial potential obtained from a Boltzmann inversion of the all-atom distributions are also shown. For most pair types, the initial Boltzmann inversion provides a very poor reproduction of the pair correlations, while the converged iterative Boltzmann inversion provides an excellent match with the atomistic distributions. A comparison of 15 converged and initial pair potentials is shown in Fig. 1.18a-o.

1.3.2 Model Verification and Validation

To verify that our 5-bead CG model of polyurea is representative of the underlying atomistic model from which it was calibrated, we compare several thermophysical and viscoelastic properties against those computed from fully atomistic simulations for oligomeric polyurea systems. In particular, we examine three different monodisperse,

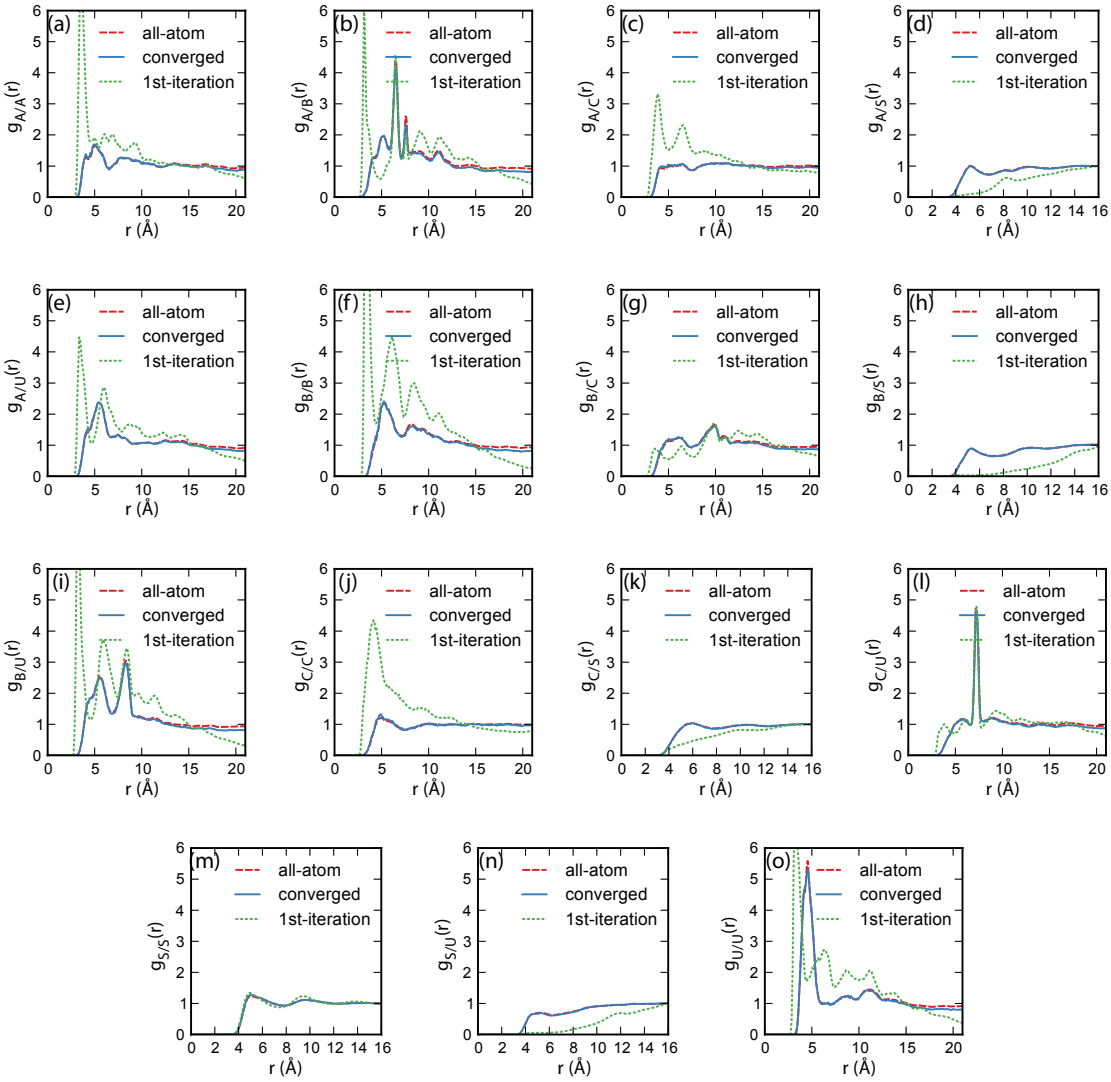

Figure 1.17: Radial distribution functions (a) $g_{\mathrm{A/A}}(r)$, (b) $g_{\mathrm{A/B}}(r)$, (c) $g_{\mathrm{A/C}}(r)$, (d) $g_{\mathrm{A/S}}(r)$, (e) $g_{\mathrm{A/U}}(r)$, (f) $g_{\mathrm{B/B}}(r)$, (g) $g_{\mathrm{B/C}}(r)$, (h) $g_{\mathrm{B/S}}(r)$, (i) $g_{\mathrm{B/U}}(r)$, (j) $g_{\mathrm{C/C}}(r)$, (k) $g_{\mathrm{C/S}}(r)$, (l) $g_{\mathrm{C/U}}(r)$, (m) $g_{\mathrm{S/S}}(r)$, (n) $g_{\mathrm{S/U}}(r)$, and (o) $g_{\mathrm{U/U}}(r)$ obtained from the all-atom MD simulations, CG MD simulations after IBI convergence and CG MD simulations during the 1st IBI iteration, i.e., based on the initial potential obtained from Boltzmann inversion of the all-atom distributions.

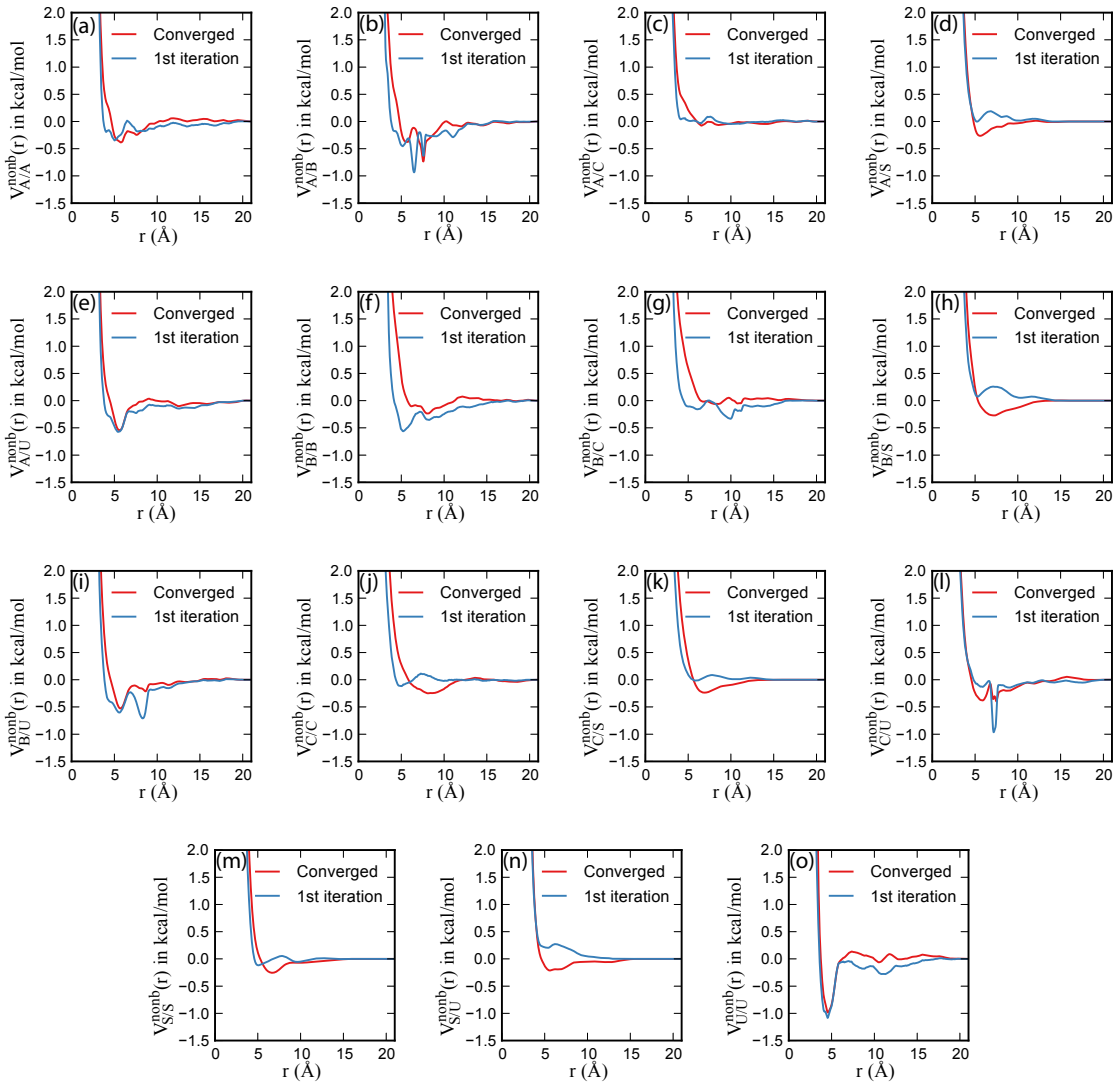

Figure 1.18: Nonbonded potentials (a) $\mathcal{V}^{\text{nonb}}_{\text{A/A}}(r)$, (b) $\mathcal{V}^{\text{nonb}}_{\text{A/B}}(r)$, (c) $\mathcal{V}^{\text{nonb}}_{\text{A/C}}(r)$, (d) $\mathcal{V}^{\text{nonb}}_{\text{A/S}}(r)$, (e) $\mathcal{V}^{\text{nonb}}_{\text{A/U}}(r)$, (f) $\mathcal{V}^{\text{nonb}}_{\text{B/B}}(r)$, (g) $\mathcal{V}^{\text{nonb}}_{\text{B/C}}(r)$, (h) $\mathcal{V}^{\text{nonb}}_{\text{B/S}}(r)$, (i) $\mathcal{V}^{\text{nonb}}_{\text{B/U}}(r)$, (j) $\mathcal{V}^{\text{nonb}}_{\text{C/C}}(r)$, (k) $\mathcal{V}^{\text{nonb}}_{\text{C/S}}(r)$, (l) $\mathcal{V}^{\text{nonb}}_{\text{C/U}}(r)$, (m) $\mathcal{V}^{\text{nonb}}_{\text{S/S}}(r)$, (n) $\mathcal{V}^{\text{nonb}}_{\text{S/U}}(r)$, and (o) $\mathcal{V}^{\text{nonb}}_{\text{U/U}}(r)$ obtained from the convergence of the IBI method compared against those used in the 1st IBI iteration (i.e., obtained from the Boltzmann inversion of the all-atom RDFs).

oligomeric polyurea systems varying from one to five blocks, $(S_6H_2S_7)_1$, $(S_6H_2S_7)_3$, and $(S_6H_2S_7)_5$. We further validate that the predicted stress response is representa-

tive of the real benchmark polyurea system by performing two simulations, one of a monodisperse polyurea system containing polymer chains composed of 7 blocks, i.e. $(S_6H_2S_7)_7$, which corresponds to the measured mass-averaged molecular weight of the benchmark polyurea, and a second polydisperse system generated by sampling from a cumulative distribution function that matches both the mean molecular weight and polydispersity index of the benchmark system.

We begin by comparing the density and thermal expansion coefficient computed from the CG and atomistic MD simulations. The computed density results are tabulated in Table 1.5 as a function of chain length. A slight increase in density with increasing chain length is seen in both the CG and atomistic MD simulations. The predicted density from the CG simulations of the $(S_6H_2S_7)_7$ polyurea system is in excellent agreement with the experimentally measured value of 1.033 g/cm^3 with negligible difference between the monodisperse and polydisperse systems. The thermal expansion coefficients computed from atomistic and coarse-grained MD simulations of monodisperse polyurea systems were 2.1×10^{-4} and 1.8×10^{-4} K^{-1}, respectively, both in excellent agreement with the experimentally measured value of 2.0×10^{-4} K^{-1}[16].

	Density		
Blocks	CG	AA	exp
1	1.071	1.064	—
3	1.078	1.079	—
5	1.081	1.080	—
7	1.087	—	1.033

Table 1.5: Comparison of calculations from CG-MD simulation (CG) and atomistic MD simulation (AA), with experimental measurements (exp) of the density.

To characterize the chain mobility of the melt state, we compute the self-diffusion coefficient D_s from the slope of the mean square displacements of each chain's center of mass [46]. The stress relaxation function $G(t)$ is computed for both CG and atomistic models from the autocorrelation of the stress history [35, 53, 62], We further smooth $G(t)$ by computing a running average over a window from $0.9t$ to $1.1t$. From $G(t)$ the frequency-dependent shear moduli, storage modulus $G'(\omega)$ and loss modulus $G''(\omega)$ are computed.

The dynamics of the CG system are much faster compared to that of the atomistic system due to the smoother CG energy landscape and reduced frictional forces acting between CG polymer chains. Previous efforts to apply time mapping between CG and atomistic simulations have used constant scaling factors [57, 58]. Conversely, in 2-bead CG model, it was found that a time-dependent scaling function $f_t(t)$ is needed to match the relaxation function with its atomistic counterpart. This dynamic scaling function is determined from the ratio of mean square displacements computed for CG and all-atom systems. At very short time scales, the value of the dynamic rescaling function is unity, and at longer time scales the rescaling function increases monotonically and saturates at a fixed value. This behavior reflects a transition from very rapid molecular relaxations, e.g. bond rotations, that do not require the chain to escape the confinement imposed by neighboring chains, to relaxation at longer time scales, which are governed by diffusion. Figure 1.19 shows the ratio of mean square displacements computed for systems containing single block chains of polyurea for CG and atomistic MD. The dynamic scaling function $f_t(t)$ is fit to an exponential series, Eq. (1.26), expressed as

$$f_t(t) = 1 + \sum_i a_i(1 - e^{-t/\tau_i}), \tag{1.26}$$

with the fitted coefficients listed in Table 1.6. The characteristic simulation times τ_i

reflect time scales over which the simulated dynamics are accelerated by the corresponding time factor a_i. The fact that multiple of such time scales exists, may be a reflection of the thermorheologically complex nature of polyurea. Using Eq. (1.26)

i	1	2	3
a_i	1773	253	282
τ_i (ns)	47	4.42	0.13

Table 1.6: Fitted coefficients to the dynamic scaling function $f_t(t)$.

the stress relaxation spectrum of the CG model is rescaled as

$$G(t) = G_{CG}(\xi(t)), \quad \text{where } \xi(t) = f_t(t)t. \tag{1.27}$$

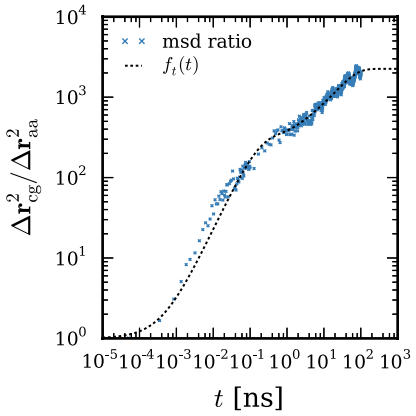

Figure 1.19: Dynamic scaling factor f_t for $(S_6H_2S_7)_1$ system; the dashed line shows the fit of f_t via Eq. (1.26)

To verify that the CG model is representative of the atomistic model in terms of its viscoelastic properties, we compare normalized relaxation spectra computed from atomistic and CG simulations, as shown in Fig. 1.20, where the CG spectra have been rescaled both by dynamic and constant time scaling factors, $f_t(t)$ and $f_t(\infty)$, respectively. The relaxation spectra scaled by $f_t(t)$ have reasonably good agreement

with their atomistic counterparts at intermediate time scales (10 ps $\leq t \leq$ 1 ns) for all three simulated molecular weights. At extremely short time scales, ($t \leq$ 10 ps), relaxation occurs through local chain conformation changes [63], which are not fully resolved in the CG model. At longer time scales, ($t \geq$ 1 ns), it becomes infeasible to sample a sufficient atomistic stress history and thus the autocorrelation function artificially decays rapidly. Similar to findings by Lee et al. [64], we observe strong oscillations in $G(t)$ at very short time scales where the running average has a very small window and where local chain relaxations occur abruptly through conformational transitions. As the geometric restrictions of the backbone of the CG model are limited to bond and relatively weak angular interactions, the initial stress relaxation computed from the CG model exhibits less severe oscillations.

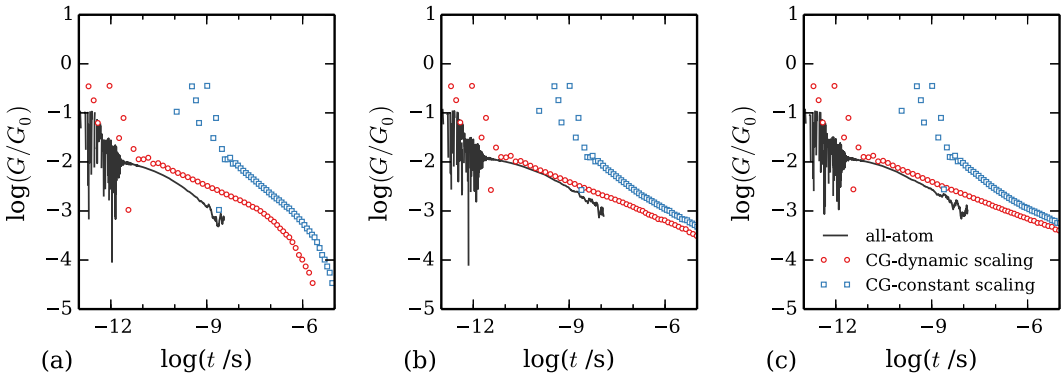

Figure 1.20: Stress relaxation spectrum $G(t)/G(0)$ for, (a) $(S_6H_2S_7)_1$, (b) $(S_6H_2S_7)_3$, and (c) $(S_6H_2S_7)_5$ obtained from all-atom MD simulations and from CG MD simulations after applying constant time scaling and dynamic time scaling factor.

The CG shear modulus is also rescaled because the stress fluctuations in the CG system reflect averaged quantities, and thus the variation of the stress is decreased. This reduction is clearly demonstrated by examining the contribution of the kinetic energy to the instantaneous shear modulus. The instantaneous shear modulus of a fluid limited to two-body interactions was derived by Zwanzig [65]. For a CG system

consists of more than one types of bead, the instantaneous shear modulus can be computed as:

$$G(0) = \rho k_B T + \sum_{\alpha=1}^{n} \sum_{\beta=1}^{n} \frac{2\pi}{15} \rho_\alpha \rho_\beta \int_0^\infty g_{\alpha\beta}(r) \frac{d}{dr} \left[r^4 \frac{d\phi_{\alpha\beta}}{dr} \right] dr. \tag{1.28}$$

where n is the number of the types of bead present in CG system. The first term, which comes from the kinetic part of the virial stress, is proportional to ρ, the number density in the system. This implies that the portion of $G(0)$ resulting from the kinetic energy of the system scales proportionally with the degree of coarse-graining. We further investigate this by computing the $G^{KE}_{\mathrm{AA}}(0)$ and $G^{KE}_{\mathrm{CG}}(0)$ values from the autocorrelation of the kinetic stress history as:

$$G^{KE}(t) = \frac{V}{k_B T} \left\langle \sigma^{KE}_{xy}(t) \sigma^{KE}_{xy}(0) \right\rangle \tag{1.29}$$

Indeed, the values of $G^{KE}_{\mathrm{AA}}(0)$ and $G^{KE}_{\mathrm{CG}}(0)$ computed only from the kinetic energy contributions to the virial stress are 430 MPa and 36 MPa respectively, and their ratio matches the degree of coarse-graining within 2%. The second term in Eq. (1.28) is also related to the number density, suggesting that the scaling factor for the pairwise contributions may be related to the degree of coarse-graining, however the radial distribution functions of the CG model are not equivalent with those of the atomistic system. In order to investigate the differences of shear modulus from pairwise energy contributions, we compute the $G^{pair}_{\mathrm{AA}}(0)$ and $G^{pair}_{\mathrm{CG}}(0)$ from the autocorrelation of pairwise stress history as

$$G^{pair}(t) = \frac{V}{k_B T} \left\langle \sigma^{pair}_{xy}(t) \sigma^{pair}_{xy}(0) \right\rangle, \tag{1.30}$$

and the computed value of $G^{pair}_{\mathrm{AA}}(0)$ and $G^{pair}_{\mathrm{CG}}(0)$ are 3.87 GPa and 0.36 MPa respectively. In order to compare the value of $G^{pair}_{\mathrm{CG}}(0)$ with Eq. (1.28), we computed the second term in Eq. (1.28) using the RDFs and pair potentials as shown in Fig. (1.17)

and (1.18). The computed value of $G_{\mathrm{CG}}^{pair}(0)$ from Eq. (1.28) is 0.25 MPa, which is in good agreement with the $G_{\mathrm{CG}}^{pair}(0)$ value computed from the pairwise energy contributions to the virial stress. Since the contributions to $G(t)$ from the bonded and nonbonded interactions are not so easily determined analytically, a comprehensive scaling parameter for $G(t)$ is computed empirically by the ratio of $G_{\mathrm{AA}}(0)$ to $G_{\mathrm{CG}}(0)$. We assume that this scaling parameter is time-independent and also independent of the length of the system. The latter of these assumptions is verified with the results summarized in Table 1.7.

Similar to the shear response, the coarse-grained model predicts an overly soft response under bulk deformation. Equilibrium MD simulations were performed under the NPT ensemble for systems composed of short, single block chains in order to calculate the long-term bulk modulus with both the coarse-grained and atomistic models, using the relationship $\kappa = \langle \delta V^2 \rangle / k_B T \langle V \rangle$. While the bulk modulus calculated from the atomistic system was 2.82 GPa, the value computed from the coarse-grained model was 0.31 GPa, an order of magnitude lower. This discrepancy is consistent with recent observations by Hsu et al. [34] that purely bottom up coarse-graining methods do not demonstrate thermomechanical consistency with their atomistic counterparts and thus either top down calibrations or determination of thermodynamic scaling relationships are necessary to make quantitive predictions from coarse-grained models.

Using the MD simulations-based approaches described earlier, we have computed the relaxation spectrum $G(t)$ of a melt of $(S_6H_2S_7)_7$ under atmospheric conditions. To obtain a quantitative spectrum, one needs to rescale the time and shear modulus axes using scaling factors $f_{\mathrm{t}}(t)$ and f_{G} obtained by performing short atomistic MD simulations of the polymer system being investigated. However, this is quite challenging for such long polyurea chains, especially obtaining $f_{\mathrm{t}}(t)$, which requires

Blocks	$G_{\mathrm{AA}}(0)$(GPa)	$G_{\mathrm{CG}}(0)$(GPa)	$f_G = \frac{G_{\mathrm{AA}}(0)}{G_{\mathrm{CG}}(0)}$
1	93.5	2.93	31.8
3	94.5	2.99	31.5
5	95.9	2.99	31.8
7	—	3.01	31.7*

Table 1.7: Summary of $G_{\mathrm{AA}}(0)$, $G_{\mathrm{AA}}(0)$, and f_G obtained from all-atom MD and CG MD simulations by varying chain lengths of different oligomeric polyurea system. The asterisk value was computed from the average value of f_G obtained from short chain length polyurea systems.

computation of a long time scale property (self-diffusivity). Fortunately, we observe that the time and shear modulus scaling factors change only slightly across the three chain lengths of polyurea studied earlier (Table 1.7). Hence, $f_{\mathrm{t}}(t)$ and f_{G} for long chains could be determined by the scaling factors computed for shorter chain systems. We expect that fully atomistic MD simulations of such a melt would require prohibitively long simulation times to probe its entire relaxation spectrum, while that the CG simulations are able to capture with much less computational effort. This can easily be gleaned from Fig. 1.21, which plots the rescaled CG relaxation spectra of the three different chain lengths polyurea melts and shows how dramatically the relaxation times of the melt rise with increasing chain length.

Additionally, we compute $G'(\omega)$ and $G''(\omega)$ obtained from the Fourier transform of $G(t)$ (Eqs. 1.19 and 1.20). In Figure 1.22, we plot $G'(\omega)$ and $G''(\omega)$ obtained from atomistic MD simulation of $(S_6H_2S_7)_5$ polyurea system. Also shown in the plots are the obtained $G'(\omega)$ and $G''(\omega)$ from CG-MD simulations after applying constant time rescaling factor and dynamic time rescaling factor, f_{t}. At first glance,

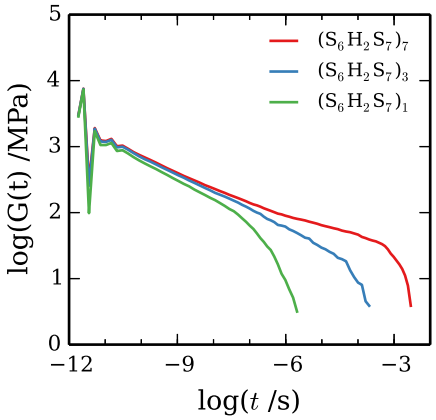

Figure 1.21: Dynamic shear modulus G(t) for $(S_6H_2S_7)_1$ (red), $(S_6H_2S_7)_3$ (blue), and $(S_6H_2S_7)_7$ (green) obtained from CG-MD simulations after applying rescaling factor f_G and $f_t(t)$ for both shear modulus and time axes, respectively.

we can clearly see the vast difference between the $G'(\omega)$ and $G''(\omega)$ value obtained from constant time scaled CG simulations and atomistic MD simulations. For the frequency range, (10^8 hz $\leq \omega \leq 10^{10}$ hz), we observe an excellent agreement between atomistic MD and CG-MD $G'(\omega)$ and $G''(\omega)$ values after applying f_{t}. For the higher frequency range, ($\omega \geq 10^{10}$ hz), the atomistic MD system is sufficient to predict the viscoelastic properties of polyurea. For the intermediate frequency range, (10^3 hz $\leq \omega \leq 10^8$ hz), where computing such wide range frequency dependent relaxation spectrum is computationally prohibitive from atomistic MD simulations, CG-MD simulation can compute $G'(\omega)$ and $G''(\omega)$ with speed up of six to seven orders of magnitude. At very low frequency, ($\omega \leq 10^3$ hz), computing $G'(\omega)$ and $G''(\omega)$ is computationally very expensive even for CG-MD simulations. Thus, the CG model developed here largely reproduces the structural, thermodynamic, and viscoelastic properties of short-chain polyurea melts computed from atomistic simulations. In Figure 1.23, we compare the frequency dependent storage and loss modulus for CG-

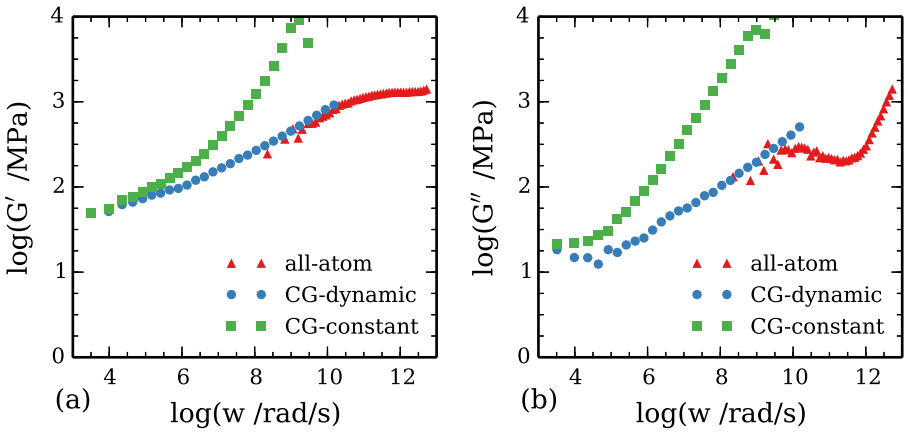

Figure 1.22: Comparison of frequency-dependent, (a) storage modulus $G'(\omega)$, and (b) loss modulus $G''(\omega)$, obtained from all atomistic simulation of $(S_6H_2S_7)_5$ polyurea system, from CG-MD simulations after applying constant time scaling and dynamic time scaling factor for $(S_6H_2S_7)_7$ polyurea system.

MD simulations by varying chain length. We observe a significant increase in the value of storage modulus from 1-block chain length CG system to 7-block chain length CG system, while in case of loss modulus, this improvement is minimal.

Finally, in Figure 1.24 we compare the predicted $G'(\omega)$ and $G''(\omega)$ values obtained from CG-MD simulation with the experimental values obtained from the ultrasonic and DMA data at 1 atm and 300 K. The experimental details regarding the synthesis and testing of the benchmark material are given in vipin et al.[66] We observe a very small difference between the scaled $G'(\omega)$ and $G''(\omega)$ values obtained from the two types of CG simulations, one for the monodisperse polyurea system and the second for the polydisperse polyurea system with PDI=41.8. For the case of storage modulus for the lower frequency range of $\omega \leq 10^6$ rad/sec, we observe a very close match between DMA and ultrasonic results if we extrapolate the ultrasonic data. Additionally, the predicted $G'(\omega)$ values from CG simulation are in good agreement in frequency

range of $\omega \leq 10^6$ rad/sec. For the higher frequency range of $\omega \geq 10^6$ rad/sec, we start to observe several differences among the results. Both the CG and ultrasonic values overestimate $G'(\omega)$ relative to the DMA results. It is evident that this overestimation is more pronounced in the CG simulation results. We do, however, observe excellent agreement between the atomistic results for frequency range of 10^8 rad/sec $\leq \omega \leq 10^{10}$ rad/sec. At lower frequency ranges, i.e., $\omega \leq 10^6$ rad/sec, the loss moduli determined from DMA and ultrasonic measurements differ substantially, with the coarse–grained predictions in closer agreement with ultrasonic measurements than DMA. At higher frequencies, the loss moduli computed from coarse–grained simulations are higher than those determined from time–temperature shifted DMA measurements. This could suggest that relaxation mechanisms with temperature dependence that is not consistent with the time–temperature superposition relationship are at at play, which consistent with prior observations that polyurea is thermorheologically-complex. Despite the observed differences between the coarse-grained computations and experimentally determined moduli, the coarse-grained models are extremely consistent with atomistic molecular dynamics calculations of the storage moduli, and reasonably consistent with atomistic predcitions of the loss moduli. Hence, we conclude that the coarse-grained models provide a representative picture of the relaxation processes captured by the all-atom simulations, and further analysis is needed to fully reconcile the computed high frequency viscoelastic response with experimental measurements.

1.4 Summary

In this work, we have developed a CG model of polyurea that corresponds to a known benchmark material system to evaluate how well systematic coarse-graining methods can predict the viscoelastic response of an elastomer at frequencies relevant

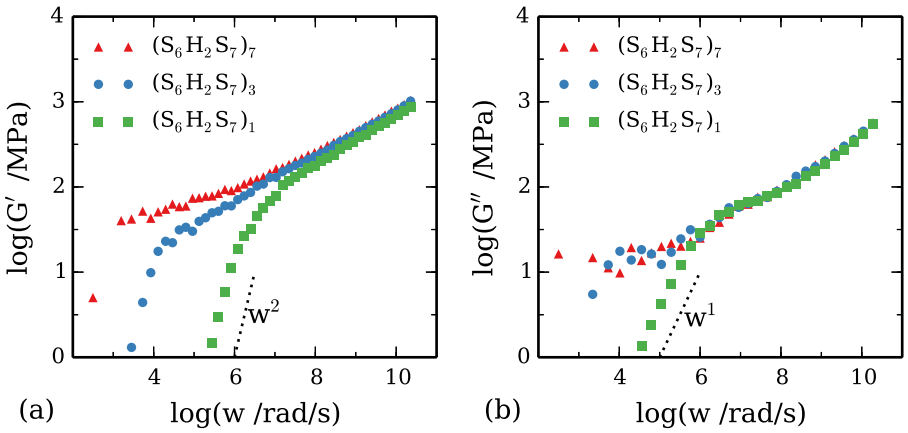

Figure 1.23: Comparison of frequency-dependent, (a) storage modulus $G'(\omega)$, and (b) loss modulus $G''(\omega)$, obtained from CG MD simulations for oligomeric polyurea of varying chain lengths. The dashed line in the G' and G'' representing the ω^2 and ω^1 scalings are included as guides.

for blast and impact energy dissipation. The CG model is calibrated in a bottomup fashion from atomistic MD simulations by simultaneously matching target pairwise, bonded, and bond-angle distributions computed from the fully atomistic system. Due to fewer degrees of freedom and a smoother free-energy landscape, frictional interactions between chain segments in the CG model are diminished, and therefore chain dynamics are accelerated. Consequently, in order to make predictions with realistic time scales, we have developed a scaling function that is calibrated from short chain simulations with the assumption that the accelerated dynamics due to coarse-graining are separable from the influence of molecular weight on chain relaxations. This scaling approach yields continuity in properties predicted through both CG and fully atomistic models at high frequencies, which is particularly evident in the nearly seamless transition from fully atomistic to CG predictions of the frequency-dependent storage modulus. Furthermore, experimental measurements of the dynamic shear moduli of

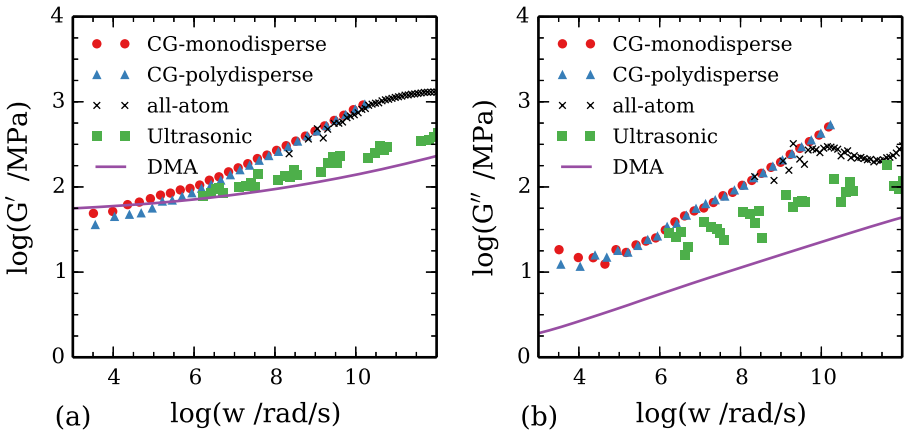

Figure 1.24: Comparison of frequency-dependent, (a) storage modulus $G'(\omega)$, and (b) loss modulus $G''(\omega)$, obtained from CG simulation for $(S_6H_2S_7)_7$ polyurea system, CG simulation by constructing simulation box of average molecular weight of 10708 gm/mol and PDI value 41.8, atomistic simulation for $(S_6H_2S_7)_5$ polyurea system, and experimental results obtained from ultrasonic and DMA data at P=1atm and T=300K.

the benchmark polyurea material by both dynamic mechanical analysis and ultrasonic wave transmission are quite comparable with the values predicted from the CG model.

For atomistic MD simulations of polyurea, it is evident that even short oligomeric chains require a significant amount of computational time to reach a well-equilibrated configuration. For instance, systems composed of a single hard segment connected to a chain of 14 tetramethylene oxide monomers require at least 32 ns of equilibration time at elevated temperatures to reach a steady state distribution. The most significant change observed during the equilibration of such oligomeric polyurea systems is the increase in the height of the peak in the H/H pair radial distribution function. Since this height corresponds to the depth of the energy well describing mutual

attraction between hard beads, calibration of a poorly equilibrated system with the IBI method will result in under-prediction of hard segment attraction and produce a system less likely to phase-segregate and ultimately not representative of polyurea. CG simulations conducted to compare the phase segregation of systems containing short oligomeric polyurea chains with systems containing longer chains produced similar results compared to the bead-spring model developed by Arman et al [53], where short oligomers produced larger clustered hard domains than did longer multi-block chains.

With copolymers that exhibit significant phase segregation, optimization of all pair potential simultaneously with iterative Boltzmann inversion appears to be more robust than individually optimizing each pair potential sequentially, due to the interdependencies between pair interactions. For example, in our polyurea CG model, the H/H and H/S interactions are correlated, as strong aggregation of the H beads automatically leads to some aggregation between the S and H beads, due to chain connectivity. Therefore, modifying the H/H potential alters both the H/H and H/S radial distribution functions. To improve the stability of the IBI method, corrections to the pair potentials are scaled by an additional parameter, α to reduce oscillations, mitigate strongly coupled interactions, and improve convergence to the target pair distributions. The optimal scaling parameter depends strongly on the underlying atomistic chemistry and CG mapping. In this work, we selected an initial value of unity and iteratively halved its value until the number of iterations required for convergence was minimized; we used the same scaling parameter for all pair combinations. A scaling factor of 0.05 is nearly optimal for our CG mapping of polyurea and excellent convergence of the target radial distribution functions is achieved within 100 iterations. While efforts to determine effective CG potentials for a phase segregating polymer blends of polyisoprene (PI) and polystyrene (PS) have been previously re-

ported [67, 68], the degree of independence between the PS/PS, PS/PI, and PI/PI pair potentials was far less than that observed here for polyurea. For instance, the peak in the radial distribution function of the polyurea CG H/H beads is four times higher than the reported peak in the PI/PI or PS/PS radial distribution functions.

A critical improvement of 5-bead model over 2-bead model of polyurea is the finer discretization of the current five-bead model. The two-bead model is suitable for predicting structural and morphological properties of polyurea as it also is calibrated to match structural distributions from atomistic simulations; however, it is not well-suited for predicting dynamic properties as it permits chains to pass through each other, thus violating topological constraints. The five-bead model presented in this work avoids such topology violations as the bond distance between beads is sufficiently small compared to their excluded volumes, and thus it is far more accurate for predicting dynamic properties.

At frequencies greater than 1 MHz, the calculated dynamic moduli from the CG model appear to be overpredic ted compared to those derived from TTS of either ultrasonic wave transmission or dynamical mechanical anal ysis measurements. The cause for this discrepancy is not clear, however, as the predicted values from both CG and fully atomi stic molecular dynamics are quite close in agreement at the very high frequencies accessible to fully atom istic models, the coarse-graining procedures developed in this work appear not to be the dominant source of error. Furthermore, as already noted, the applicability of TTS for polyurea at such high frequencies is questionable, especially for the loss modulus. Atomistic molecular dynamics studies of polyurea have been conducted with general purpose force fields, none of which have been explicitly calibrated for polyurea nor specialized for predicting mechanical properties. While the development of more accurate force fields for polymers is well beyond the scope of the present study, such improvements may be necessary for more

quantitatively accurate atomistic simulations.

The CG methodology developed in this work can be applied to predict the viscoelastic properties of many complex polymer materials, including chemical modifications of polyurea to design a tailored response, e.g. optimization of dissipation for a specific frequency band. Future work to extend this polyurea model to represent the multifunctional isocyanate present in common commercially available polyureas, which have been recently been the focus of many experimental studies [5, 16, 23, 69, 70] would help link observations of macroscopic properties to the chemistry and morphology of polyurea.

The model presented in this work is limited to studying near-equilibrium properties of polyurea, such as the mechanical response to weak shocks. In general, coarse-graining approaches are not yet suitable for representing large deformation, strong shock wave propagation, or large changes in temperature or pressure due to the well-documented lack of pressure and temperature transferability in these models. Furthermore, the scaling parameters used to map predictions of thermomechanical properties to real systems, require full-scale atomistic simulations to be performed for calibration, and rely on the assumption that such scaling factors are invariant over long time scales. The development of improved CG models that can more faithfully represent the thermodynamic state of a system thus remains a formidable yet important challenge.

Despite such challenges, the computational efficiency gained from coarse-graining approaches is tremendous and enables atomistic simulations to approach time and length scales that are relevant for practical application. In this work, a CG model of polyurea containing 10k beads progresses at a rate of 18 μ/day on 64 CPU cores (Intel Xeon E5-2670 processors). This is approximately 50% slower than the coarser two-bead model, yet including the faster dynamics, allows a million-fold speedup over

fully atomistic molecular dynamics. With this speedup, molecular models can directly probe the viscoelastic response to millisecond time scales.

Chapter 2

PREDICTION OF SHOCK HUGONIOT RESPONSE OF POLYETHYLENE

2.1 Introduction

Excellent mechanical properties, such as high toughness and the ability to dissipate shock and impact loads, make semicrystalline polymers suitable for many applications such as protective coatings, reinforced structural composites, sporting equipment, artificial joints for orthopedic devices, and lightweight armors. Traditionally, the development of materials for new applications has followed an iterative, empirically-driven process that requires a large investment of both time and effort. To accelerate new material development, computationally-aided material design processes are needed to efficiently explore the enormous design space of polymer chemistry, molecular architecture, and processing parameters. Such an approach is particularly needed for materials that must withstand extreme environments, as these conditions can be difficult and costly to reproduce experimentally. While both quantum mechanics calculations and classical molecular dynamics (MD) simulations have been used to explore properties such as the shock Hugoniot of various polymers [71], these methods are limited to quite small simulation volumes, e.g. tens of thousands of atoms or length scales on the order of 10 nm, and thus cannot incorporate important structural details, such as the lamellar structure of semi-crystalline polymers. Thus, the objective of this paper is to broaden the applicability of molecular models to investigate the role of nanoscale structural features on the thermomechanical response of polymers subjected to dynamic loading characteristic of shock and impact.

Several coarse-graining (CG) methods have been applied to study the response

of polymers under shock loading. Arman et al.[53] developed a bead-chain model similar to that of Kremer and Grest [72] to analyze the microstructure and shock response of polyurea-like multiblock and diblock copolymers. However, simple bead-spring models can only represent a polymer qualitatively, and so predictive modeling requires the use of systematic coarse-graining methods such as iterative Boltzmann inversion[28, 35, 38–40, 73] or force matching[74, 75] to model the interactions specific to a given polymer chemistry. In this light, Grujicic et al.[76] utilized the adaptive biasing force method to calibrate a CG model of polyurea based on simple Lennard-Jones interactions in order to compute the shock Hugoniot response. However, their model underpredicts experimental measurements[77] of the linear Hugoniot slope coefficient (du_s/du_p) by more than a factor of three, indicating that simple pairwise interactions are insufficient to represent thermodynamic properties across a broad range of state-space. Likewise, Santo et al.[78, 79] studied the interaction of shock waves with lipid membranes, using the MARTINI[80] force field, which can represent the u_s-u_p curve Hugoniot curve in water only for weak shocks ($u_p \leq 1$ km/s). Fu et al.[81] used the united atom model[82, 83] (UAM) to study dynamic response of polyethylene polymer nano–composite under shock wave loading and while their shock Hugoniot predictions are in good agreement with experimental data, the degree of coarse-graining that the UAM provides is quite modest, and thus for long chain molecules, a more general coarse-graining strategy is needed.

Coarse-grained models of polymers suffer from several limitations that restrict their capabilities to represent the correct thermodynamic response of material under non-equilibrium processes resulting from shock and impact loading. A major challenge for structure-matching methods is that of representability, i.e., the ability of a model to represent the correct thermodynamic state of a system, including properties such as density, heat capacity, and elastic moduli. A second challenge is that of trans-

ferability, i.e., the extent that a potential is accurate across different thermodynamic states. This latter requirement is particularly important to be able to predict material strength and toughness under dynamic loading, as the material may experience a wide range of temperatures and pressures along a deformation path leading to failure. Unfortunately, the transferability of CG models to thermodynamic states other than those in which they were calibrated has been shown to be inconsistent and difficult to predict[84, 85].

As demonstrated by Henderson et al. [86] for a specific CG mapping, there is a unique pairwise potential that can be derived to match the pairwise structural distributions of a fluid. However, the derived CG system will not generally reproduce the correct thermodynamic properties. This was also demonstrated by Johnson et al.[87], for CG water potentials where a single site effective potential derived to match structural distributions fails to reproduce higher order structural correlations, as well as thermodynamic properties such as virial pressure and internal energy. One remedy is to parameterize the CG models directly from experimental data [88], which is referred to as the "top down" approach. However, this approach is not predictive as empirical thermodynamic state data is required a-priori. Other strategies have been proposed to combine bottom-up and top-down methods in order to improve the representability of CG models. For example, Rosch et al[89] were able to improve the ability of a CG models of polystyrene to better represent the elastic moduli by manipulating the nonbonded interactions; however, the modified potential greatly affected the structure of the equilibrium model.

In order to improve the transferability of CG models, a multistate extension of the iterative Boltzmann inversion (IBI) method was proposed by Moore et al[90] to match the RDFs of a CG system with target data sampled from atomistic MD simulations performed at multiple thermodynamic states. By including target data for multiple

states, more constraints are added to the optimization of the CG potentials, which minimizes the state dependence of the derived potentials. As the objective of this work is to develop CG models that are transferable across a broad range of pressures, we further include a many-body interaction term to decouple the pairwise interactions from the pressure response so that the CG model can simultaneously reproduce RDFs and accurate pressures across a range of densities. The formulation of the many-body interaction term is adapted from the embedded atom method (EAM)[91], and thus we will refer to this method as the IBI-EAM method.

2.2 Computational Methods

In this section, we describe two different CG models of polyethylene (PE). The first is developed using the structure–based, iterative Boltzmann inversion (IBI) method, and in this chapter is subsequently referred to as the standard CG model. The second model is developed using a new approach that combines the multistate IBI method with a many-body interaction term calibrated to match thermodynamic states at multiple thermodynamic calibration states. The CG model resulting from this method will be referred to as the CG-EAM model throughout the remainder of this paper.

2.2.1 All–Atom Simulations

The CG models created in this work are calibrated in a bottom–up fashion from structural and thermodynamic state data sampled from all-atom MD simulations. All simulations are carried out using the large-scale atomic/molecular massively parallel simulator (LAMMPS) code [50]. We use the PCFF forcefield, a class II forcefield, to model the interactions between atoms. The functional form of the class II forcefield and its parameterization for alkane molecules are reported by Maple et al.[92]. Long-range Coloumbic interactions are computed using the particle-particle/particle-mesh

(PPPM) method in the LAMMPS kspace package [42]. The cutoff distance for short range Coloumbic and pairwise interactions was set to 9.5 Å.

To generate target structural distributions and state data, models of low molecular weight, linear PE were initialized by a random-walk process in a periodic unit cell. Ten $(C_2H_4)_{80}$ molecules are placed in a non-overlapping, random configuration within the computational cell [41]. As the procedure taken to equilibrate the atomistic systems is similar to previous studies [66, 73], we only briefly summarize the important details here. The atomistic systems are equilibrated in three parts: a constant pressure-temperature (NPT) run of 8 ns at 500 K, followed by a 8 ns temperature ramp to 300 K, and a final equilibration run of 16 ns at constant temperature and pressure (300 K and 1 atm). Following this equilibration, a 1 ns production run is performed in the canonical (NVT) ensemble to sample the radial, bond-length, and bond-angle distribution functions. In order to reduce the influence of the initial randomly generated state of the atomistic system, we sampled the structural distribution functions by averaging atomistic MD trajectories obtained from 10 different starting configurations. The average density over the ten configurations was 0.7841 g/cm^3.

We also sampled target structural distributions and densities along an isothermal volumetric deformation path. From the configurations relaxed at atmospheric pressure, a sequence of relaxation and sampling steps were performed at increasing pressure up to 10 GPa. After each pressure increment, a 4 ns NPT simulation was performed at the prescribed pressure set point, followed by a 1 ns NVT sampling run. This sequence was repeated, starting again from the configurations relaxed at 1 atm, for dilational up to a maximum hydrostatic tension of 50.7 MPa. Beyond this point, the deformation would localize with the formation of voids. The ten different states along the isotherm are summarized in Table 2.1.

Pressure (MPa)	Density (g/cm^3)	$\langle\rho\rangle$
-50.7	0.748	27.74
-10.1	0.781	28.96
0.1	0.784	29.02
1	0.785	29.22
10	0.792	29.33
100	0.829	30.69
1000	0.971	35.9
2000	1.043	38.53
5000	1.161	42.85
10000	1.274	47.03

Table 2.1: Pressure state points used to calibrate the IBI-EAM potentials for polyethylene. The average value of the cumulative density at a particle $\langle\rho\rangle$ is proportional, but not equivalent to the mass density.

2.2.2 Standard CG Model

We calibrated a CG model of PE using the standard IBI method. In the IBI method, interactions among CG beads are governed by an effective potential function, which is calibrated to match target structural distributions sampled from all–atom MD simulations. Figure 2.1 shows the chemical structure and mapping of the CG model of PE.

As previously mentioned, we calculated three types of structural distribution functions from the all–atom MD simulations. First, we collected the distributions in bond

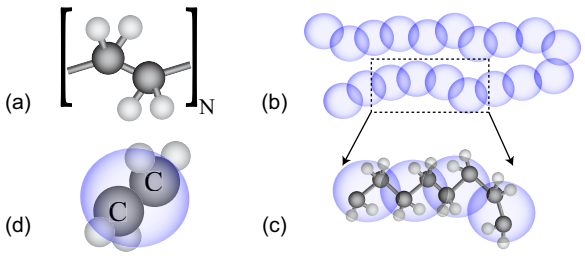

Figure 2.1: CG model of PE: (a) chemical structure of the repeating unit of PE, (b) figurative representation of a short PE chain composed of CG beads, (c) CG mapping of atoms to bead coordinates, (d) chemical structure of a single CG bead; the coordinate of the bead is coincident with the center of the C-C bond.

lengths l, which are the distances between the coarse-grained sites along the polymer chain and represent the distances between centers of consecutive beads along a chain. The bond-length probability distribution, $P(l)$ is used to parameterize the bond-stretching potential, $\mathcal{V}^{\text{str}}(l)$, of the CG model. The bond lengths sampled from the all–atom MD simulations form a double peaked distribution corresponding to the *trans* and *gauche* conformations along the PE molecule. In this study, we neglect the relatively small peak corresponding to the *gauche* configuration and approximate the bonded interactions with a harmonic potential fitted to the Boltzmann inversion of $P(l)$. The resulting CG bond potential is

$$\mathcal{V}^{\text{str}}(l) = \frac{k}{2}\left(l - l_0\right)^2, \tag{2.1}$$

where $k = 227.48$ kcal/mol/Å^2 and $l_0 = 2.5736$ Å are the bond stiffness and equilibrium bond length, respectively.

We also sampled the probability distributions of bond angles θ, which are the angles between consecutive bonds along the polymer chain. We use this bond angle probability distribution $P(\theta)$, to generate an initial approximation of the CG bending

potentials, $\mathcal{V}^{\text{bend}}(\theta)$, by the Boltzmann inversion

$$\mathcal{V}_0^{\text{bend}}(\theta) = -k_B T \ln\left(\frac{P(\theta)}{\sin(\theta)}\right). \tag{2.2}$$

where k_B is the Boltzmann constant, T is the temperature, and $\sin(\theta)$ accounts for the degeneracy in the coordinates of three sequentially bonded CG sites with fixed bond angle θ.

Lastly, we gathered the RDFs, $g(r)$, of pair distances between non-bonded pairs of beads. The RDFs are used to generate an initial approximation of the CG non-bonded potential $\mathcal{V}^{\text{pair}}(r)$.

$$\mathcal{V}_0^{\text{pair}}(r) = -k_B T \ln(g(r)) \tag{2.3}$$

To begin the IBI process, we generated approximate potentials using Eq. (2.1-2.3) and then placed 15 CG $(C_2H_4)_{80}$ molecules in a random, non-overlapped configuration. Each IBI iteration step starts with a 0.48 ns equilibration step at 300 K in NVT ensemble integrated with a time step of 8 fs. The equilibration step is followed by a pressure-correction step, during which the system is held at 300 K for 0.64 ns in the NVT ensemble to sample the virial pressure. We next adjusted the pressure by adding a linear correction[30] to the pair potential to match the computed CG pressure to the target pressure computed in the atomistic simulations. After the pressure correction cycle, a production run in the NVT ensemble is performed for 0.64 ns at 300 K to sample the structural distribution functions. Based on the difference of the structural distributions between the AA and CG model, corrections to the pair and angle potentials are applied using the IBI method:

$$\mathcal{V}_{i+1}^{\text{pair}}(r) = \mathcal{V}_i^{\text{pair}}(r) + \alpha k_B T \ln\left(\frac{g_i(r)}{g_{md}(r)}\right) \tag{2.4}$$

$$\mathcal{V}_{i+1}^{\text{bend}}(\theta) = \mathcal{V}_i^{\text{bend}}(\theta) + \beta k_B T \ln\left(\frac{P_i(\theta)}{P_{md}(\theta)}\right) \tag{2.5}$$

where $\alpha = 0.2$ and $\beta = 0.05$ scale the corrective terms in order to improve the stability of the IBI process. We iterate the IBI steps discussed above, inclusive of the pressure correction cycle, until the CG structural distribution functions converge to the atomistic structural distribution functions within a prescribed tolerance. Figure 2.2 shows the structural distribution functions obtained from the all–atom and CG MD simulations after convergence of the IBI method.

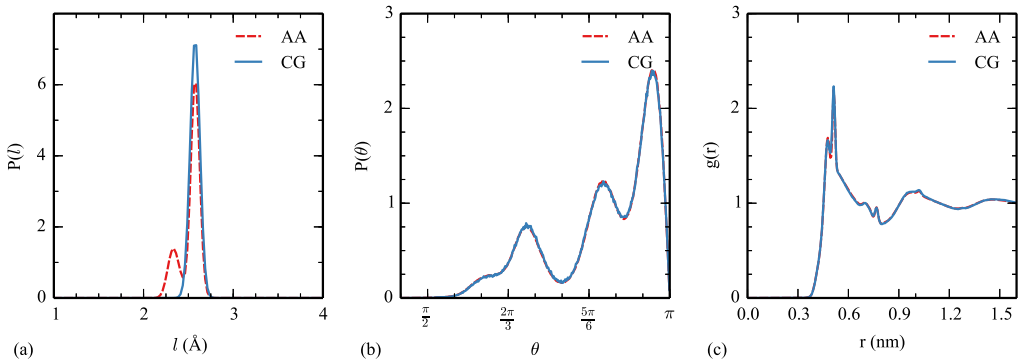

Figure 2.2: Comparison of distributions of (a) bond lengths $P(l)$, (b) bond angles $P(\theta)$, and (c) the radial distribution function $g(r)$ obtained from all-atom (AA) and CG MD simulations.

Using both the atomistic and the calibrated CG models, we performed NPT MD simulations at atmospheric pressure and 300 K of 50 $(C_2H_4)_{80}$ molecules starting with randomly generated configurations. The resulting configurations observed after 32 ns and 100 ns of simulation time for the all–atom and CG simulations, respectively, are shown in Figure 2.3. The emergence of semi-crystalline structure in the CG MD simulation is somewhat remarkable given that the target structural data from which the CG model was calibrated did not include any noticeable crystallinity, evident from the relatively flat RDF seen in Figure 2.2c. Furthermore, the CG model provides a speedup factor of 2-3 orders of magnitude over the AA model, due to the reduced

number of degrees of freedom, relatively simpler potentials, and larger stable time step in the integration of the equations of motion. As a result, the CG model is able to probe longer time scales and thus more efficiently explore the configurational space to the point that crystal nucleation and growth is observed.

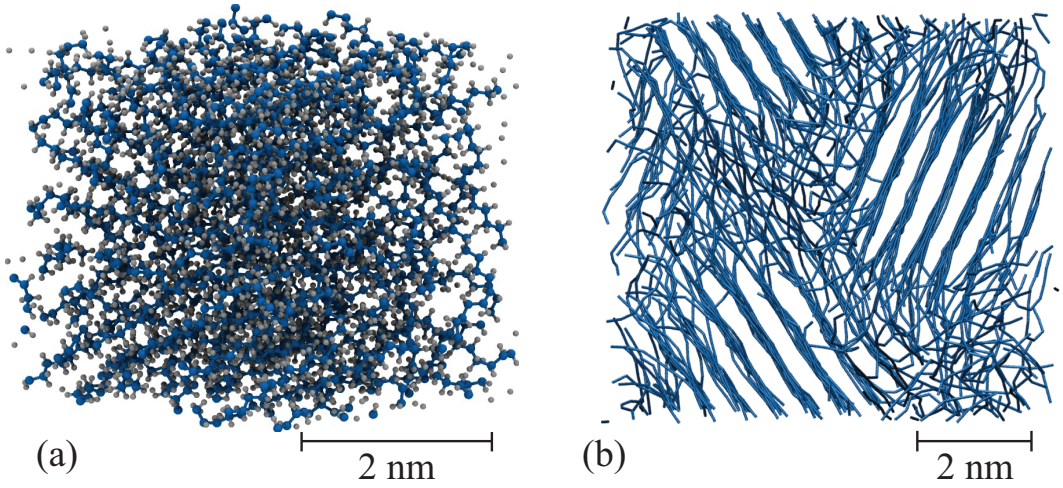

Figure 2.3: Observed structure of low molecular weight, linear polyethylene computed in (a) all–atom (AA) and (b) CG MD simulations.

2.2.3 Pressure Transferable and Representable CG Model

Coarse-grained MD simulations are not typically employed to study shock dynamics and high strain rate loading of polymers due to their well-known representability [84, 93] and transferability [85, 94] issues. For simulation of shock loading, it is crucial that a model can accurately represent the equation of state of the material. In order to highlight the poor pressure transferability characteristic of structure-based CG models, we compare CG potentials calibrated by the standard IBI method from target data sampled at different target pressures (1 atm and 1 GPa). The density versus pressure curves, computed by both CG models, are compared with a curve computed from all-atom molecular dynamics in Figure 2.4. Due to the linear pres-

sure correction step, both CG models reproduce the correct density at the pressure at which they were each calibrated, however, away from these pressures they rapidly diverge from the all–atom predictions. Thus, CG models generated by the IBI method for polyethylenes have very poor representability and transferability.

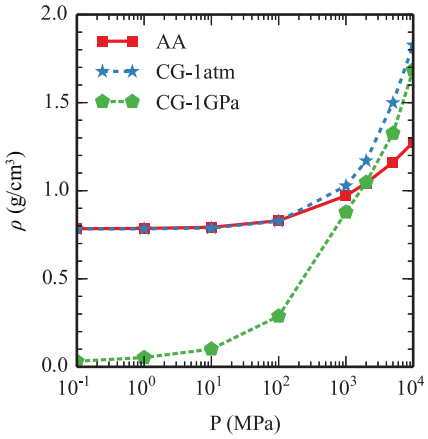

Figure 2.4: Comparison of density as a function of pressure along the 300 K isotherm computed from the AA model and from CG models calibrated at 1 atm and 1 GPa.

To correct these problems, we first consider the general expression of the potential energy of a system of N interacting particles:

$$\phi(\mathbf{r}) = \sum_{i<j}^{N} \phi_{ij}^{(2)}(r_i, r_j) + \sum_{i<j<k}^{N} \phi_{ijk}^{(3)}(r_i, r_j, r_k) + \ldots + \sum_{i<j<k\ldots<N}^{N} \phi_{ij\ldots n}^{(n)}(r_i, r_j, \ldots, r_N) \tag{2.6}$$

where, $\phi^{(2)}$, $\phi^{(3)}$ and $\phi^{(n)}$ are two, three, and n-body interactions, respectively. It is common to truncate the series after pairwise interactions so that the total potential energy of the system is approximated as pairwise terms $\phi^{(2)}$ and all higher order terms are neglected. However, this assumption is only valid for low density states.[95, 96] At higher densities, the effect of many-body terms becomes increasingly significant, and thus to improve the accuracy of CG polymer models at higher pressures, we adopt a

many-body interaction based on an estimate of the local density field.

2.2.4 CG-EAM Model

In what we refer to as the IBI-EAM method, the embedded atom model (EAM) is combined with the multistate IBI method[90] to develop a pressure–transferable CG model. The EAM potential describes interactions among atoms, including an embedding function that approximates the energy required to place an atom within the electron cloud surrounding its neighbors. In the EAM, the electron cloud density is computed by a summation of the contributions of all neighboring atoms. For the purpose of improving the representability of CG models of polymers, we utilize the general idea of the EAM; however, instead of representing an electron cloud density, the mass density is approximated by a kernel density estimator. Thus the embedding energy function directly relates the local density field to the potential energy, and thus provides a means to correct the pressure that can be nonlinear without disrupting the accuracy at which the model reproduces local structural features such as the RDF. In the IBI-EAM method, the bond, angle and pair interactions are optimized to reproduce local structural distributions, while the embedding energy term is optimized to represent thermodynamic state properties. In the implementation described here, all energy interactions are calibrated in a bottom-up approach from thermodynamic and structural information sampled from all–atom MD simulations using classical force fields. However, the target thermodynamic data can also be supplied from experimental measurements or quantum mechanical calculations.

The total potential energy of a CG system using the IBI-EAM method is written as:

$$\phi = \sum_i \left(\sum_{j>i} \phi_{ij}^{(2)}(r_{ij}) + F(\rho_i) \right) + \sum_k \mathcal{V}^{str}(l_k) + \sum_m \mathcal{V}^{bend}(\theta_m) \tag{2.7}$$

where $\rho_i = \sum w(r_{ij})$ is the cumulative local density evaluated at atom i, r_{ij} is the

distance between atoms i and j, F is the embedding energy function, and $\phi^{(2)}(r)$, $\mathcal{V}^{str}$ and $\mathcal{V}^{bend}$ are the pairwise, bond stretching, and bond bending energies, respectively. The kernel function $w(r)$ represents the distribution of mass each CG bead contributes to the local density field. The kernel function is arbitrarily chosen as $w(r) = (1 - r/r_c)^2$, which monotonically and smoothly decays to zero at the prescribed cutoff distance r_c. We do not normalize the kernel function, i.e., $\int w(r)\, dV \neq 1$, and thus it is proportional but not equivalent to the local number density. The model can be readily extended to polymers coarse-grained with multiple bead types by scaling the kernel functions by the mass of each CG bead.

The embedding function is approximated as a polynomial expansion of the cumulative density field. It should be noted that $F(\rho)$ must not be linear, in which case embedding energy is identical to a pair potential. The parameters of the embedding function are optimized by the least–squares method to minimize the error in the representation of the equation of state along selected calibration state points.

The virial pressure in MD simulations is computed as

$$p = \frac{Nk_BT}{V} + \frac{1}{3V}\sum_{i}^{N} \mathbf{r}_i \cdot \mathbf{f}_i, \tag{2.8}$$

where N is the number of atoms in the system, V is the system volume, and the second term includes the forces acting on each atom resulting from all bonded and nonbonded interactions. As the total force acting on each atom is a summation of pairwise, bond stretching, angle bending, and embedding interactions, the pressure can be decomposed as:

$$p = p_{ke} + p_\phi + p_F + p_b + p_a \tag{2.9}$$

where p_{ke}, p_ϕ, p_F, p_b, and p_a are the components of the pressure resulting from the kinetic, pairwise, embedding, bond, and angle energies, respectively. The correction

to the CG pressure is made by modifying the contribution from the embedding energy,

$$p_F = \frac{1}{3V} \sum_i \mathbf{r}_i \cdot F'(\rho_i) \sum_{j \neq i} w'(r_{ij}) \hat{\mathbf{r}}_{ij}. \tag{2.10}$$

In order to optimize the embedding energy $F(\rho)$, we first simplify Eq. (2.10) by approximating the cumulative local density ρ_i evaluated at each atom with its expected value, $\langle \rho_i \rangle$ at each calibration state using the RDF sampled from the atomistic simulations.

$$p_F = \frac{AN}{V} F'(\langle \rho_i \rangle), \tag{2.11}$$

where AN approximates the term $\sum_i \mathbf{r}_i \sum_{j \neq i} w'(r_{ij}) \hat{\mathbf{r}}_{ij}$. A value of $A = 100$ was heuristically determined by maximizing the rate of convergence of the pressure correction. The expected value of the local density $\langle \rho_i \rangle$ at each bead is calculated as:

$$\langle \rho_i \rangle = \frac{N}{V} \int_0^{r_c} g(r) w(r) 4\pi r^2 dr. \tag{2.12}$$

In order to calibrate the parameters of the embedding function $F(\rho)$, we sampled the density and structural distribution functions from atomistic MD simulations m different states along an isothermal compression at 300 K. As previously mentioned, the embedding energy is represented by a Taylor series approximation,

$$F(\rho) = \sum_{k=1}^{n} a_k \rho^k, \tag{2.13}$$

where a_k are the embedding energy parameters. For the parameterization of polyethylene, calibrated over a pressure ranging from -50 MPa to 10 GPa, a quartic function, $n = 4$, is sufficient to describe the embedding energy. Substituting (2.13) into (2.11), gives

$$p_F^{(m)} = \sum_{k=1}^{n} a_k D_{km} \quad \text{where} \quad D_{km} = \left[\frac{AN}{V_m} k \left\langle \rho_i \right\rangle_m^{k-1} \right] \tag{2.14}$$

where, V_m is the volume and $\langle \rho_i \rangle_m$ is the expected value of cumulative density of the mth state. A least square minimization method is used to optimize the coefficients

of the embedding function, based on the difference between target AA pressure and CG-EAM model pressure for m different states. We calculate the embedding function parameters $\Delta\mathbf{a}$ at each IBI-EAM iteration step as:

$$\Delta\mathbf{a} = \left(\mathbf{D}^T\mathbf{D}\right)^{-1}\mathbf{D}^T\Delta\mathbf{p}, \tag{2.15}$$

where the vector $\Delta\mathbf{p}$ is the difference in the pressure computed from the atomistic and CG-EAM MD simulations at each calibration state.

As with the standard IBI method, we begin the calibration of the CG-EAM model by initializing pair and angle potentials using the Boltzmann inversion of $g(r)$ and $P(\theta)$. The same bond stiffness and equilibrium bond length from the standard CG model are used in the CG-EAM model. The initial coefficients of the embedding energy are set to zero; i.e., at the first step there is no pressure correction term applied. At the sampling stage, the RDF $g(r)$ and bond angle distribution $P(\theta)$ are computed for each of the m different calibration state points from the trajectories of the CG coordinates. Following the multistate IBI method described by Moore et al. [90] the pair and angle bending potentials are corrected by averaging the corrective terms over each of the calibration state points using the expressions:

$$\mathcal{V}_{i+1}^{\text{pair}}(r) = \mathcal{V}_i^{\text{pair}}(r) + \left\langle \alpha k_B T \ln\left(\frac{g_{m,i}(r)}{g_{m,md}(r)}\right)\right\rangle, \tag{2.16}$$

and

$$\mathcal{V}_{i+1}^{\text{bend}}(\theta) = \mathcal{V}_i^{\text{bend}}(\theta) + \left\langle \beta k_B T \ln\left(\frac{P_{m,i}(\theta)}{P_{m,md}(\theta)}\right)\right\rangle, \tag{2.17}$$

where the same scaling factors, $\alpha = 0.2$ and $\beta = 0.05$, used to stabilize the standard IBI method are applied. After the pair and angle bending potentials are corrected, the parameters of the embedding energy are optimized to correct the pressure using Eq. (2.15).

The process to calibrate the CG-EAM model is summarized as follows. Initial configurations of 15 $(C_2H_4)_{80}$ molecules are randomly generated in cubic simulation

domains with box sizes dictated by the target density at each calibration state point. Each configuration is then relaxed by a 0.48 ns NVT MD simulation at a fixed temperature of 300 K. This relaxation step is then followed by a 0.64 ns production run to sample the pressure of each of the configurations. The pressure computed at each calibration state point is then compared with the target pressure computed in the all–atom MD simulations to compute a correction to the parameters of $F(\rho)$ using Eq. (2.15). After this pressure correction step, a second set production runs of 0.64 ns is performed using the updated embedding energy to sample the structural distribution functions at each of the calibration state points. The computed distribution functions are then compared against the target distributions to update the pair and angle potentials using Eqs. (2.16) and (2.17). This entire procedure is then iterated until the structural distribution functions and pressures computed from the CG model match the target all–atom data.

For the CG model of polyethylene, the convergence of the embedding energy is quite rapid, matching the target pressure data in 15 iterations, while the angle and pair energies require 80 iterations to converge. The latter convergence rate could likely be improved by selecting more aggressive scaling factors (α and β); however, as the major computational task is the generation of sufficiently sampled target atomistic data, we did not attempt to optimize the scaling factors.

The calibrated potentials, excluding the harmonic bond potential, are plotted in Figure 2.5. The pair potentials $\mathcal{V}^{\text{pair}}(r)$ of the standard CG and CG-EAM models are similar, with the exception that the CG-EAM has deeper energy minima at $r =$ 0.48 nm and $r = 0.54$ nm. The angle bending potentials $\mathcal{V}^{\text{bend}}(\theta)$ are similar for angles larger than 140°, but for angles $90 < \theta < 140°$, the CG-EAM potential has a somewhat higher energy. It should be noted that at higher pressures, there is a larger fraction of bond angles where $\theta < 2\pi/3$, and thus the CG-EAM model, optimized by

the multistate IBI method, is calibrated using a wider sampling of these smaller bond angles.

Figure 2.5c shows the optimized embedding energy $F(\rho)$, with the averaged cumulative density at each bead labeled at selected calibrated pressures, and the corresponding distributions of local cumulative density plotted along the bottom axis. The best fit coefficients of the embedding energy are listed in Table 2.2. As the embedding function is approximated as a polynomial, it is generally unfit for extrapolation, and thus the calibration points should encompass the range of states encountered in the problem being modeled. For example, as it is calibrated here, the potential becomes unstable at high temperature and low pressure, because the embedding energy decays to zero as the local density decreases beyond $\rho < 25$ due to thermal expansion.

a_1	a_2	a_3	a_4
0.357	0.0103	-8.78$\times 10^{-4}$	1.32$\times 10^{-5}$

Table 2.2: Optimized coefficients (in kcal/mol) of the embedding energy function.

2.3 Results and Discussion

2.3.1 Model Verification and Validation

In this section, we evaluate two CG models of polyethylene: a model parameterized at 300 K and 1 atm by the standard IBI method, and a model parameterized at different states along an isothermal p-V curve at 300 K by the IBI-EAM method. Figure 2.6 compares the bond angle distributions $P(\theta)$ and radial density functions $g(r)$ computed at five selected states using the all–atom, standard CG, and CG-EAM models. We omit a comparison of the bond length distributions as they are not very sensitive to the pressure and thus the distributions are not appreciably different

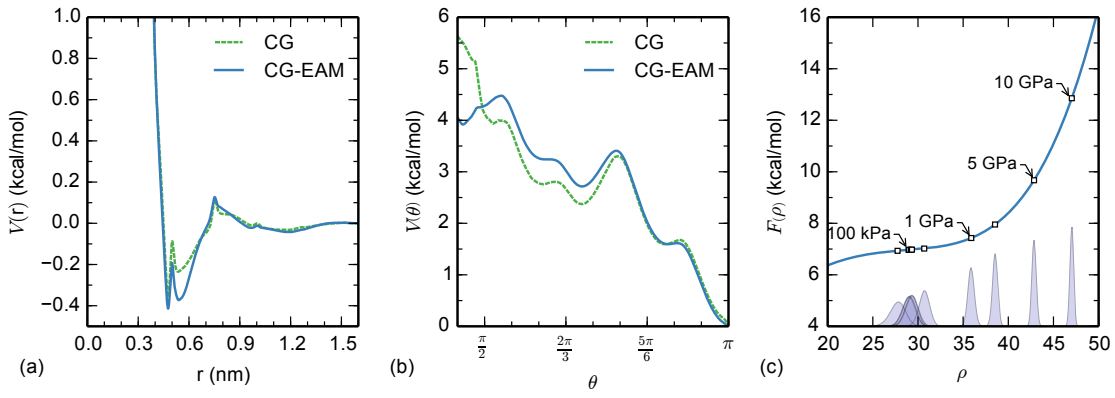

Figure 2.5: Optimized potential functions of the CG-EAM model: (a) pair potential, $\mathcal{V}^{\text{pair}}(r)$ (b) bending angle potential, $\mathcal{V}^{\text{bend}}(\theta)$, and (c) embedded energy function. In (c), the averaged density $\langle \rho_i \rangle$ is marked by a '□' at each calibration point and the corresponding distributions of bead densities are plotted along the bottom axis.

than those shown in Figure 2.2c. While the standard CG model is able to reproduce the bond angle distributions $P(\theta)$ reasonably well across the range of pressures, the radial distribution functions are shifted toward shorter pair distances reflecting an inaccurate computed density, and the distribution of peaks is qualitatively different from the target all-atom distributions. Meanwhile, the CG-EAM shows a substantial improvement in reproducing both the angle distributions and RDFs up to 5 GPa, although there are some small differences at the highest pressure point of 10 GPa. At such high densities, many-body effects become increasingly important and intercorrelations between local densities, bond-lengths, and bond-angles may become non-negligible.

To validate the representability and transferability of the CG-EAM model, we tested it along different thermodynamic paths, including the shock Hugoniot, using the multiscale shock-wave molecular dynamics technique (MSST)[97]. A simulation volume containing 200 randomly-distributed $(C_2H_4)_{80}$ molecules was generated by a

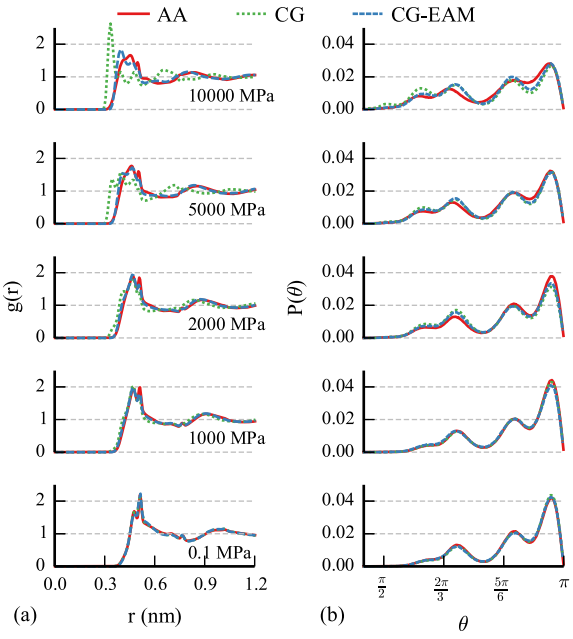

Figure 2.6: Analysis of transferability of the standard CG and CG-EAM models comparing the (a) radial distribution function $g(r)$ and (b) bond angle distribution function $P(\theta)$ across a range of pressures.

non-backtracking random walk. This system was equilibrated using the standard IBI-derived CG model for polyethylene over a simulation time of 960 ns at 300 K and 1 atm pressure. The resulting equilibrated structure is semi-crystalline, and has a density of 0.81 g/cm^3. From this starting configuration, we performed simulations comparing the standard IBI-derived CG model, the CG-EAM model, as well as all–atom MD simulations using a configuration generated by a reverse-mapping procedure. The all–atom and CG configurations are shown in Figure 2.7.

In the reverse-mapping procedure, each CG site is replaced by an ethylene monomer such that the generated interatomic bond lengths and bond angles are approximately at their equilibrium values. The atomistic structure is then briefly relaxed over a 10 ps simulation at constant temperature and volume (NVT). Table 2.3 shows the comparison of the average speed up achieved from the CG and CG-EAM model

relative to the all–atom MD simulations. While the CG-EAM model has, approximately, twice the computational cost as the standard CG model, it offers a nearly 60x speedup compared to all–atom MD. Furthermore, our present implementation of the CG-EAM model in LAMMPS is suboptimal as the pairwise and embedding interactions are computed separately, necessitating two loops over the neighbors of each CG site per time step. We expect that an optimized implementation could be comparable in performance to the standard IBI model.

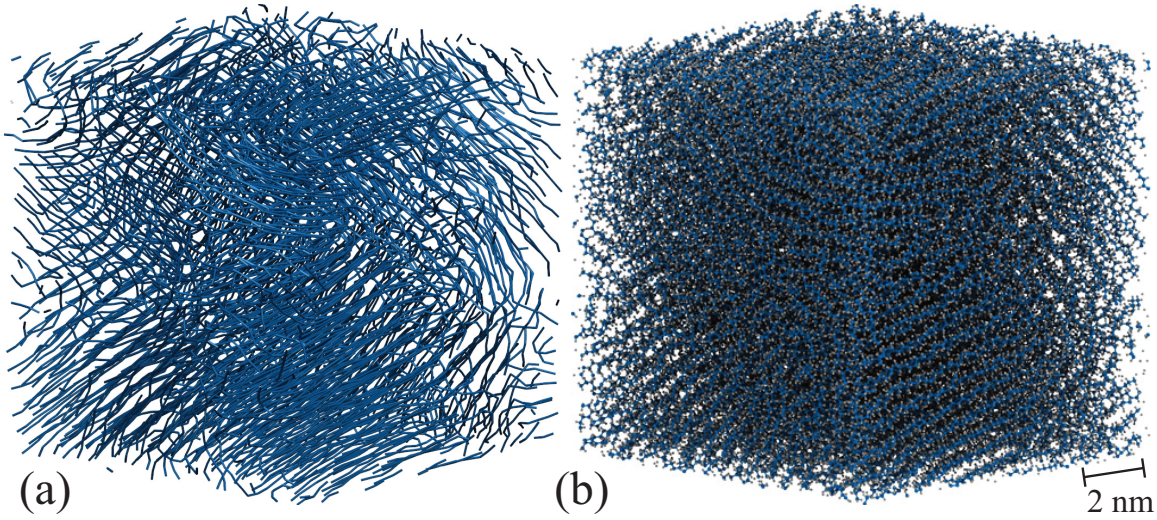

Figure 2.7: Semi-crystalline (a) CG and (b) reverse-mapped all-atom configurations of system containing 200 $(C_2H_4)_{80}$ molecules.

First, we verify that the CG-EAM model can accurately represent the thermodynamic response of the semi-crystalline configuration under isothermal compression at 300 K. Figure 2.8 shows the P-v curves computed with the standard CG, CG-EAM, and AA models. The excellent agreement between the pressures computed by the CG-EAM and AA models indicates that the calibrated parameters of the embedding function for the amorphous phase are also applicable for the crystalline phase.

Following the work of Hooper et al.[98], we fit the Tait equation of state (EOS)

Model	Δt (fs)	CPU (s)	Speed-up
AA	1	1825.2	–
CG	8	14.2	130.3x
CG-EAM	8	31.8	58.8x

Table 2.3: CPU time for a 1 ps MD simulation of 200 $(C_2H_4)_{80}$ molecules performed using the atomistic, standard CG, and CG-EAM models. The benchmark simulations were performed using a single core on an Intel Xeon E5-2670 processor.

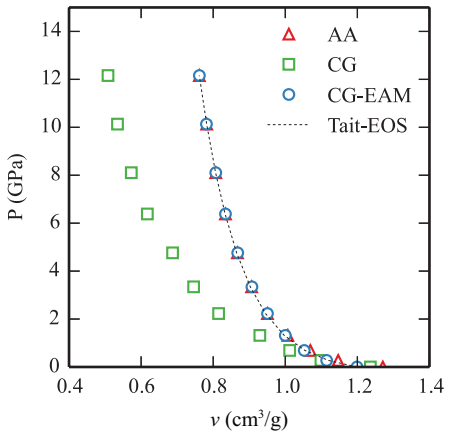

Figure 2.8: Isothermal compression P-v curves computed for semi-crystalline PE.

to the isotherm at 300 K. The Tait EOS[99] relates density to pressure and has the form:

$$\frac{V}{V_0} = 1 - c \ln\left(1 + \frac{P}{b}\right), \tag{2.18}$$

where P is pressure, V is volume, and V_0 is volume at zero pressure. The parameter b is a temperature-dependent material constant, and the parameter c has been found to be somewhat of a universal constant for many polymers, with a value of $c = 0.0894$ [100–102]. Fitting the Tait equation to the P-v curve calculated by the CG-EAM model resulted in parameter values of $c = 0.0955$ and $b = 275.94$ MPa.

To validate that the model is representative beyond isothermal states, we compute and compare the shock Hugoniot curves using all three molecular models. Neglecting the effect of shock heating, we transform the isothermal compression curve generated by the fitted Tait EOS into a "pseudo" u_s-u_p plane[98] and compare the resulting u_s-u_p Hugoniot curve with experimental measurements[103], and MSST simulations. The comparisons are shown in Figure 2.9. The MD simulations conducted using the CG-EAM and all-atom models closely match the experimental measurements, while the standard CG model fails to capture the rate at which the shock speed increases with increasing particle velocity. Furthermore, as the u_s-u_p curve calculated using the fitted Tait EOS is in agreement with the CG-EAM simulations, we conclude that shock heating effects do not appear to play a significant role for particle velocities $u_p < 3$ km/s.

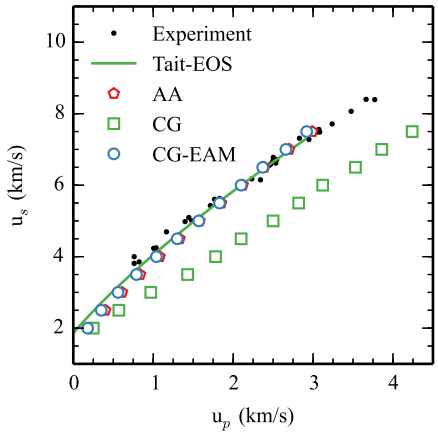

Figure 2.9: Computed u_s–u_p Hugoniot for the semicrystalline PE from the experimental data, Tait EOS, AA model, standard CG model and CG-EAM model. Experimental data are obtained from Marsh et al [103] for 46% crystalline PE.

The Hugoniot P-v curves calculated by the MD simulations are compared with experimental measurements in Figure 2.10a. The values computed by the CG-EAM

model closely follow the values computed by the all–atom model, indicating that the pressure response is consistent between the two models. Conversely, the standard CG model fails to reproduce the response calculated by all-atom simulations. The calculated results appear shifted relative to the experimental measurements. This is most likely due to the lower initial density of the molecular models. This conclusion is supported by transforming the computed u_s-u_p Hugoniot curve onto the P-v plane. We first fit the u_s-u_p relationship computed by the CG-EAM model to a linear relationship, i.e., $u_s = c + su_p$. The fitted parameters $c = 1.864$ km/s and $s = 1.959$ are then used to compute the P-v response along the Hugoniot by:[104]

$$v = \frac{1}{\rho_0}\left(1 - \frac{1}{s} + \frac{c}{su_s}\right), \text{ and} \tag{2.19}$$

$$P = \frac{\rho_0}{s}\left(u_s^2 - cu_s\right), \tag{2.20}$$

where ρ_0 is the initial density. Figure 2.10b shows two computed P-v curves, one using the initial density computed in the MD simulations and the other using the experimentally measured initial density. As the latter provides a reasonably good agreement with the experimental values, we conclude that the discrepancy between the simulated and measured Hugoniot pressures is caused primarily by the lower initial density of the molecular model.

To better understand the thermodynamics of the CG-EAM description, we analyze the Grüneisen constant, a dimensionless parameter that relates the mechanical and thermal properties of a material[105–107]. From a thermodynamic standpoint, the Grüneisen parameter is defined as $\gamma = V(\partial P/\partial E)_V$ [108], i.e., the derivative of pressure with respect to internal energy at constant volume. In terms of physical parameters, the Grüneisen constant can also be written as, $\gamma = \nu\alpha K_T/C_v$, where ν is the specific volume, α is the volumetric thermal expansion coefficient, C_v is the heat capacity, and K_T is the isothermal bulk modulus. Alternatively, the lattice Grüneisen

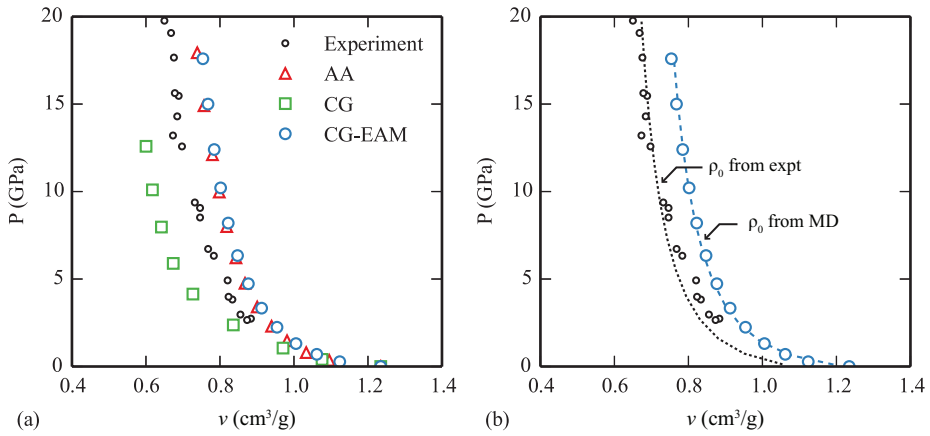

Figure 2.10: Comparisons of P-v curves along the Hugoniot between experimental values[103] and (a) MD calculations using all–atom (AA), a standard coarse-grained model (CG), and the CG-EAM model, and (b) transformation by Eq. (2.20) of the u_s–u_p Hugoniot computed from MD simulations using the CG-EAM model to P-v curves.

parameter[105] $\gamma_L = 1/2(\partial K/\partial P)_T$, is related to motion of polymer chains with respect to each other. In contrast to the thermodynamic Grüneisen constant, which effectively averages all molecular vibrations, the lattice Grüneisen constant describes the low frequency, highly anisotropic lattice vibrations that govern physical properties at lower temperatures.

Unlike metals, for which γ can be reliably calculated using thermodynamic properties, polymers are strongly anisotropic due to the sharp contrast between the stiff covalent bonds along the molecular chain and the weaker van der Waals interactions acting between chain segments. Furthermore, as the anharmonicity of the van der Waals forces is much larger than that of the covalent bonds, physical properties closely related to anharmonicity are determined by interchain vibrations. In CG models, the interchain vibrations governed by stiff covalent bonds are eliminated, and thus high frequency, short wavelength modes are not present. However, the anisotropy of the

lower frequency, longer wavelength modes should be preserved as they would be reflected in non-Gaussian structural distributions, which are accurately reproduced due to the IBI calibration. Thus, we conclude that the CG models are representing the interchain modes with sufficient accuracy to capture the coupling of thermal effects with pressure relevant to shock propagation. As a result, the CG model can provide valuable information about the thermal and mechanical properties of a polymer specific to the lower frequency, highly anisotropic vibrations that would be difficult or impossible to measure experimentally.

The all–atom MD simulations predict larger values for both $(\partial P/\partial T)_V$ and heat capacity relative to the CG models by factors of 2-5x. On the other hand, both CG models predict similar values of the $(\partial P/\partial T)_V$ and heat capacity. Additionally, the CG models show an increasing value of the derivative of pressure with temperature under compression, while the specific heat capacity is relatively constant under compression. As demonstrated in a prior study[73], CG models systematically underpredict the heat capacity of materials due to their reduced degrees of freedom, and as a result, for the same amount of change in internal energy, will produce a higher temperature rise. Now, given that both the CG-EAM and all–atom models exhibit a similar mechanical response, we argue that the heat capacity is the major factor for obtaining a higher temperature rise from the CG-EAM model.

We computed the Grüneisen constant γ using the thermodynamic definition by performing NVT MD simulations at selected points along the Hugoniot and calculating the rate of change of pressure and internal energy with temperature, as shown in Figure 2.11. The resulting Grüneisen constants are plotted in Figure 2.12, showing a consistent increase in γ with compression. At the initial density and temperature, the molecular models all show relatively good agreement with the value reported by Warfield [105]. We note that γ/ν, which is typically a constant for metals, is not so

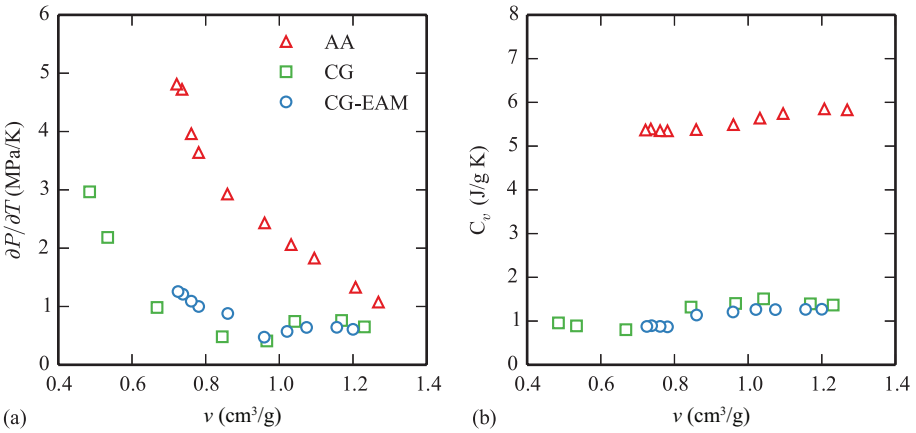

Figure 2.11: Computed values of (a) $(\partial P/\partial T)_V$ and (b) C_v along the Hugoniot from CG and all–atom MD simulations.

in this case, indicating that the relationship of γ with respect to specific volume is quite different for polymers.

Conversely, the lattice Grüneisen constant computed at the initial density by standard CG model, $\gamma_L = 3.54$, differs significantly from the value computed by the CG-EAM model, $\gamma_L = 5.74$, which is within 10% of the reported experimental value of 6.4[105]. The reason that standard CG models cannot produce accurate estimates of the lattice Grüneisen constant stems from the linear pressure correction term added to the pairwise potentials. This linear term has the effect of adding a constant force between all pairs of CG interaction sites. However, the lattice Grüneisen constant depends on the derivative of the bulk modulus, which would require at minimum a cubic correction to the potential energy to calibrate. Meanwhile, the embedding energy function used in the CG-EAM model is a quartic function of the local density, and is calibrated to correct the pressure at multiple states along an isotherm.

As measurement of the temperature rise in shocked polymers remains a significant experimental challenge, molecular models that can accurately predict shock heating can be helpful to develop equation of state models. We compare the temperature rise

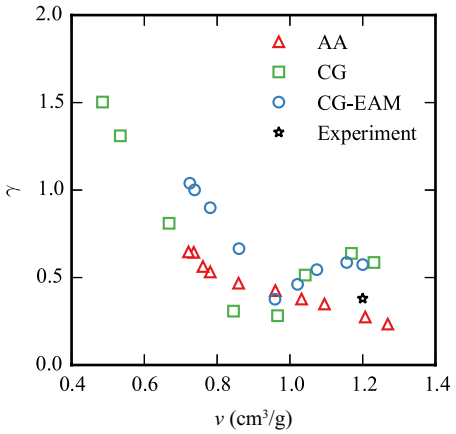

Figure 2.12: Grüneisen constant as a function of specific volume along the Hugoniot computed from the CG and all–atom models. The '⋆' denotes the value, $\gamma = 0.38$, calculated by Warfield[105] from measurements of the thermomechanical properties of PE at standard conditions.

computed by the three molecular models in Figure 2.13a. Although the standard CG model closely follows the path of the all–atom model in the T-v plane, the deviation in pressure is quite large, and thus the correlation in the T-v plane is likely coincidental. Conversely, while the CG-EAM model closely matches the all–atom simulations in the P-v plane, there is a significant difference in the predicted temperature rise. These results indicate a significant challenge in developing CG models with consistent thermodynamics.

Following the work of Forbes et al[108], we computed the temperature along the Hugoniot using the Mie–Grüneisen EOS by:

$$T_H(v) = T_0 e^{-\eta} + e^{-\eta} \int \frac{1}{2C_v} \left(\left(\frac{dP_H}{dv} \right) (v_0 - v) + P_H \right) e^{\eta} dv, \tag{2.21}$$

where, $\eta = \int \frac{\gamma}{v} dv$, P_H is the pressure along the Hugoniot, v_0 is the initial specific volume, and T_0 is the initial temperature. For simplicity, we assume a constant heat capacity along the Hugoniot, using the values computed at the initial density from

each of the molecular models. The temperature along the Hugoniot computed from Eq. (2.21) are compared with the temperatures calculated by the MSST simulations for the three molecular models. Since, the thermodynamic Grüneisen constants and P-v Hugoniot curves are similar for the CG-EAM and all–atom models, the temperature difference between these models must be primarily caused by the reduced heat capacity of the CG-EAM model. Accordingly, we recomputed the T-v curve of the CG-EAM model using instead the heat capacity computed from the all–atom model. The comparison of the temperatures predicted by the all–atom model and the CG-EAM model using the CG and all–atom heat capacities is shown in Figure 2.13b. The T-v curve computed using the corrected heat capacity matches that of the all–atom simulations within 10%. Moreover, the values computed with Eq. (2.21) are comparable with the quantum mechanical calculations of shock temperatures reported by Mattsson et al.[109] for crystalline PE; however, while quantum mechanical simulations are constrained to relatively small simulation sizes, the CG models reported here are computationally efficient enough to consider semi-crystalline configurations. Thus, while the CG simulations cannot be used to directly compute shock temperatures, the thermodynamic properties that can be predicted are sufficient to develop an EOS that can be used to compute the temperature along the Hugoniot with reasonable accuracy.

2.4 Summary

We have developed a new coarse-grained model that combines the structure–matching iterative Boltzmann inversion method at multiple thermodynamic states with a many–body interaction that greatly improves the representability and transferability of the model. Despite the fact that the model was only calibrated to match target local structural distributions and thermodynamic state data sampled from

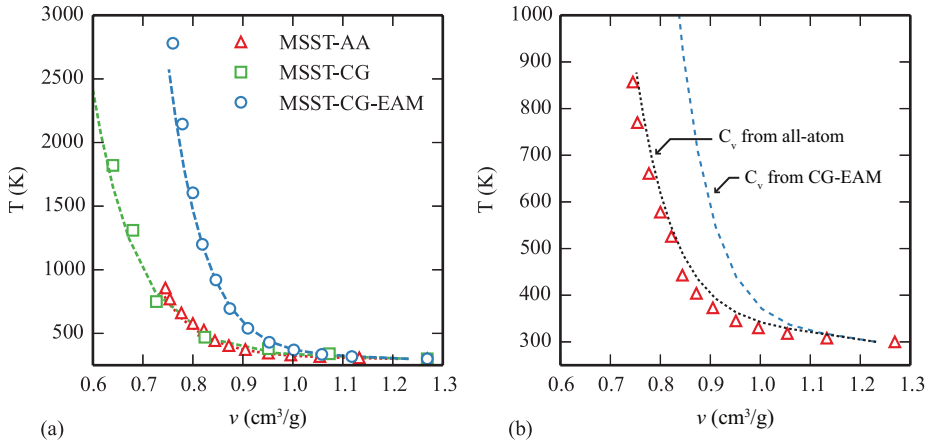

Figure 2.13: Comparison of computed and theoretical temperature rise along the Hugoniot: (a) Computed and integrated temperature rise for AA, CG and CG-EAM models. Dashed lines show the temperature rise for each model, (b) theoretical temperature rise of the CG-EAM model using computed and rescaled heat capacity.

all–atom MD simulations along an isotherm, the model is predictive along different thermodynamic paths, e.g., along the shock Hugoniot. However, due to the reduced number of degrees of freedom, the heat capacity of the model system is reduced in comparison to the heat capacity predicted by all–atom MD simulations. Nevertheless, the model predictions of the Grüneisen parameter (both overall and lattice) are consistent with experimental measurements, and so it is possible to compute the temperature rise along the Hugoniot using the Grüneisen parameter obtained by CG MD simulations but with the heat capacity calculated from all–atom simulations. As a result the CG-EAM model is simultaneously able to represent accurate structural detail and thermodynamic properties, which is in sharp contrast to structure–based CG models that are calibrated solely to match local structural distributions at a single state point, and therefore provide unreliable predictions of thermodynamic properties. In its current implementation, the CG-EAM model provides a nearly 60–fold speedup relative to all–atom MD simulations, which is roughly half the speedup offered by the

standard CG model. Accordingly, simple structure–based models remain useful for generating relaxed molecular configurations, as they are less computationally demanding and thus can efficiently explore the configurational space at a specific thermodynamic state. This work represents an important step toward realizing coarse-grained molecular models that can predict structure–property relationships in polymers. For a more complete understanding of the relationship between the Grüneisen parameter and polymer structure, we are working to characterize the shock Hugoniot properties of semicrystalline polyethylene with varying crystallinity, texture, and off-Hugoniot response. Furthermore, we plan to extend the EAM-inspired many–body interaction to be applicable for more complicated polymer chemistries, e.g., phase–segregated copolymers to provide a broadly applicable tool for studying the effect of chemistry and polymer structure on thermophysical properties in extreme conditions.

Chapter 3

AN ITERATIVE BOLTZMANN INVERSION METHOD TO MATCH THE CORRELATION OF INTERDEPENDENT VARIABLES

3.1 Introduction

Molecular scale computational methods are becoming popular to investigate the relationship between nanoscale structural features and thermomechanical response of polymers. While both quantum mechanics calculations and classical molecular dynamics (MD) simulations have been widely used to explore the properties of polymers such as shock Hugoniot response, plastic deformation mechanism, and viscoelastic properties, [54, 66, 71, 81, 109–112] these methods are limited to small simulation volumes, e.g. tens of thousands of atoms or length scales on the order of 10 nm, and thus cannot used to investigate the effect of important structural details on the thermomechanical response of the polymers. In order to model processing such as cold drawing and crystallization of polymers[113–115], or study the different conformations of peptides[116], computationally efficient coarse-grained (CG) models are required, which can generate large scale molecular structures of the polymers.

Structured-based CG models are calibrated by matching local structural distributions including pair distances, bond length, bond angles, and dihedral angles among CG interaction sites. [28–30, 35, 38, 39, 73]. The common assumption in these methods is that structural variables are uncorrelated and therefore the potential energy can be formulated additively. In practice, this assumption depends on the chemical structure of the polymer and the chosen CG mapping scheme. For example, Faller et al.[47] showed that a CG mapping of the cis-1-4-poly-isoprene results in double peaked

bond length distribution, and this multiplicity in peaks leads to interdependence of the bond and angle potential.[22]. In a similar study performed by Harmandaris et al.[117], CG models of polystyrene were unable to reproduce the correlations of bond-angle and dihedral angle. Fukunaga et al. [118] also observed strong correlations between bond-length and bond-angles in systems forming lamellar crystalline structures. A similar observation was made for models of hexane, where bond-lengths and bond-angles were seen to be correlated with each other[48]. Bezkorovaynaya et al.[116] showed the correlations of bond-angle and torsion angles from the CG models of peptides. All of these studies indicate the importance of capturing the correlations of bonded interacting terms to increase the fidelity of CG models. Li et al.[119] showed that a CG model derived by matching the local structural distributions of pair distances, bond-length and bond-angles is unable to match the correlations of bond-angles and bond lengths of polyethylene, as a result, the CG model of PE was not able to match the structural distributions in both the amorphous and crystal phases of semicrystalline PE.

The objective of this work is to increase the fidelity of CG models in generating large scale molecular structures by reproducing the correlations of interdependent variables. In this study, we address this objective by implementing a computational method to train effective CG potentials that match correlation of interdependent variables. As a test case, we extended the iterative Boltzmann inversion (IBI) method[30] and reproduce the correlated distributions of bond-length and bond-angles to generate more accurate structure of semicrystalline PE. The IBI derived CG model of polyethylene is referred as CG-BA model for the remainder of this study.

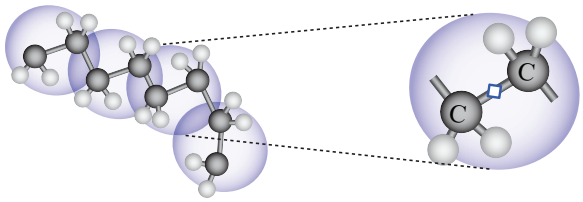

Figure 3.1: Coarse-graining of polyethylene into one site per monomer, located at the C-C bond midpoint.

3.2 Computational Methods

3.2.1 CG Model of PE

For calibrating CG potentials of polyethylene, the radial distribution function $g(r)$, bond-length distribution function $P(l)$, and bond-angle distribution function $P(\theta)$ are sampled from the all-atom MD simulations. Details of the all-atom MD simulations for sampling the $g(r)$, $P(l)$, and $P(\theta)$ are described in our previous works[120]. The distribution of torsion angles is not considered in this study. Two different variations of IBI-derived CG models of PE is considered in this study. Detailed description of mapping scheme and coarse-graining methodology of both type of CG models of PE are described by Li et al.[119]. Figure 3.1 shows the CG mapping of the CG model of PE. The first variation referred to as the CG-HB model, is derived by approximating $P(l)$ by a single Gaussian function and second variation is referred as CG-NLB model where $P(l)$ is reproduced by a sum of two Gaussian functions.

3.2.2 Structure of Semi-Crystalline PE

Figure 3.2 shows the distributions functions, i.e., $P(l)$, $P(\theta)$, and $g(r)$ obtained from all-atom MD simulations at 1 atm and 300 K. In case of the CG mapping scheme of PE, different peaks in $P(l)$ and $P(\theta)$ correspond to the different local conformations of PE, which are illustrated in Fig. 3.3. The shorter coarse-grained bond-lengths

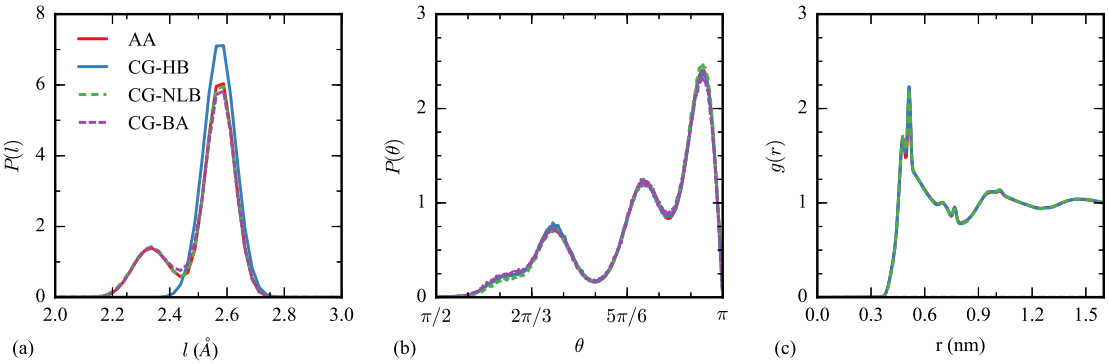

Figure 3.2: Comparison of (a) $P(l)$, (b) $P(\theta)$, and (c) $g(r)$ obtained from the all-atom (AA), CG-HB, CG-NLB, and CG-BA models of polyethylene at 1 atm and 300 K.

$l = 2.33$ $\mathring{A}$ correspond to atomistic configurations forming a gauche conformations, while the longer coarse-grained bond-lengths, $l = 2.57$ $\mathring{A}$, correspond to trans conformations. The crystal phases of polyethylene consists of parallel chains, each in all trans configurations. Whereas, combinations of gauche and trans conformations are formed in the amorphous phase. We first investigate whether the CG-HB and CG-NLB models reproduce the distributions of these individual conformations accurately. Therefore, we compare $P(l)$, $P(\theta)$, and $g(r)$ obtained from the CG-HB and CG-NLB models with structural distributions obtained from the all-atom MD simulations in Fig. 3.2. The CG-HB model can only reproduce $P(l)$ around longer l=2.57 $\mathring{A}$, while the CG-NLB model reproduced the more accurate $P(l)$. The coarse-grained models yield similar $P(\theta)$ and $g(r)$. Most CG approaches including, CG-HB and CG-NLB assume that correlations between different variations is uniform (i.e. uncorrelated) and the probability distributions of microstates can be formulated as $P(l, \theta, r) = P(l)P(\theta)g(r)$. This assumption is not valid using the mapping scheme we have defined.

Next to check the importance of correlated distribution of bond-length and bond-

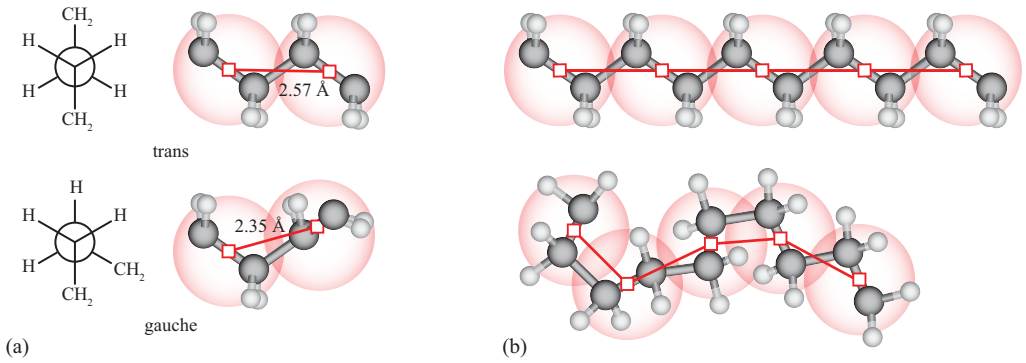

Figure 3.3: (a) Coarse-graining polyethylene into one site per C_2H_4 group leads to two peaks in the bond length distribution arising from trans and gauche conformations. (b) Crystalline chain segments are composed of all trans conformations resulting in collinear sites, and amorphous segments include both trans and gauche conformations.

angle of PE, we compute $P(l)$ and $P(\theta)$ sampling from simulations of the amorphous and crystal phases of PE. Amorphous phase of PE is generated by performing constant pressure-temperature MD simulations at 450 K and 1 atm. Figure 3.4 compares $P(l)$ and $P(\theta)$ obtained from the amorphous phase of the all-atom, CG-HB, and CG-NLB models. While the CG-NLB model more accurately reproduces the double-peaked bond-length distribution found in the amorphous phase, as shown in Fig. 3.5(b) it erroneously shows a double-peaked distribution also in crystalline phase. Since the different back bone torsion conformations are reflected by different virtual bond-length and bond-angle between CG beads, the bond-lengths and bond-angles are correlated, violating the assumption that the probability distributions of CG variables can be factorized. In the following, we develop a method to generate coarse-grained potentials where the distributions can only be partially factorized.

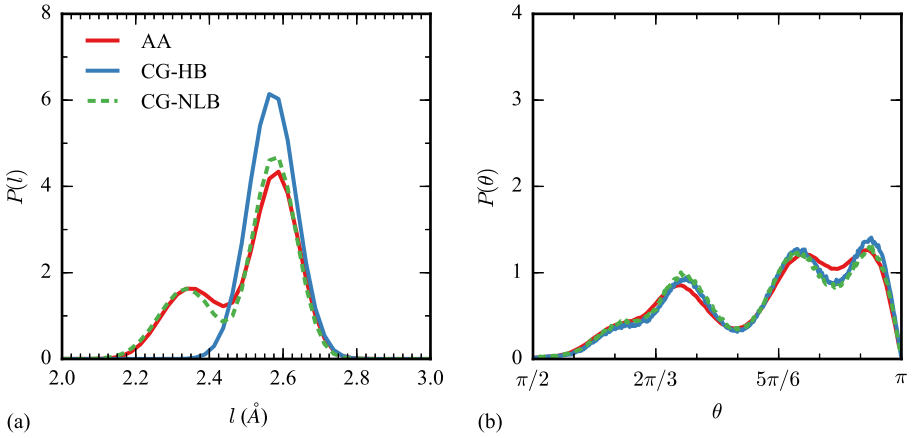

Figure 3.4: Comparison of (a) $P(l)$ and (b) $P(\theta)$ sampled from MD simulations of the amorphous phase using the of the all-atom (AA), CG-HB, and CG-NLB models.

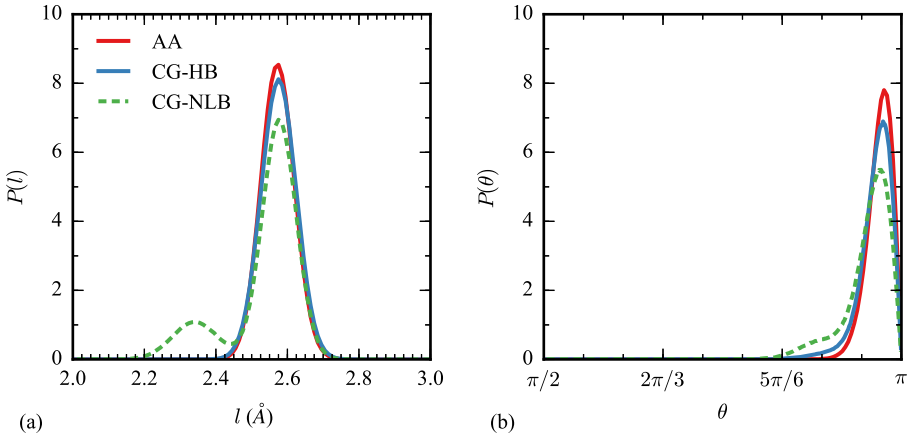

Figure 3.5: Comparison of (a) $P(l)$ and (b) $P(\theta)$ sampled from the MD simulations of the crystal phase using the all-atom (AA), CG-HB, and CG-NLB models.

3.2.3 Correlated Distributions of Bond-Length and Bond-Angle

The correlated distributions of bond-length and bond-angle $P(l, \theta)$ by estimating the kernel densities of sampled atomistic datasets in (l, θ) space. The analytical expression of computing kernel densities is given by Eq. 3.2.

$$P(l, \theta) = \frac{1}{nh} \sum_{i=1}^{n} K(l - l_i, \theta - \theta_i), \tag{3.1}$$

$$\text{where } h = 2\pi L\Theta, \text{ and } K(l, \theta) = \exp\left(-\frac{l^2}{2L^2} - \frac{\theta^2}{2\Theta^2}\right), \tag{3.2}$$

and where, n is the number of sampled bond/angle pairs from the atomistic trajectories. The density function was evaluated on a rectangular grid with 150 points along the bond length axis ($1.5 < l < 3.5$) and 250 points along the bond angle axis ($0 < \theta < \pi$). The bandwidth parameters L and Θ control the smoothness of the density function and were set to be 1.2 times the grid spacing along each axis.

Figure 3.6(a) shows the correlated distributions of bond-lengths and bond-angles at 300 K and 1 atm. The highest probability of $P(l, \theta)$ is found at θ=174° and l=2.57 $\mathring{A}$, which coincides with the maxima of $P(l)$ and $P(\theta)$. For the shorter bond-lengths, l=2.33 Å, most probable bond-angle is at $\theta = 155°$ and with zero probability at $\theta = 174°$. However, both the CG-HB and CG-NLB models do not show such correlated distributions of bond-lengths and bond-angles from the Fig. 3.6(b) and 3.6(c). The CG-HB model does not shows any configurations for shorter bond-lengths, and the CG-NLB model gives the additional configurations for the shorter bond-lengths.

Further, the original IBI method was formulated under the assumption that assumes that the $P(l)$, $P(\theta)$, and $g(r)$ are independent of each other[28–30, 73]. Consequently, the overall configuration probability $P(l, \theta, r)$ is expressed as $P(l)P(\theta)g(r)$

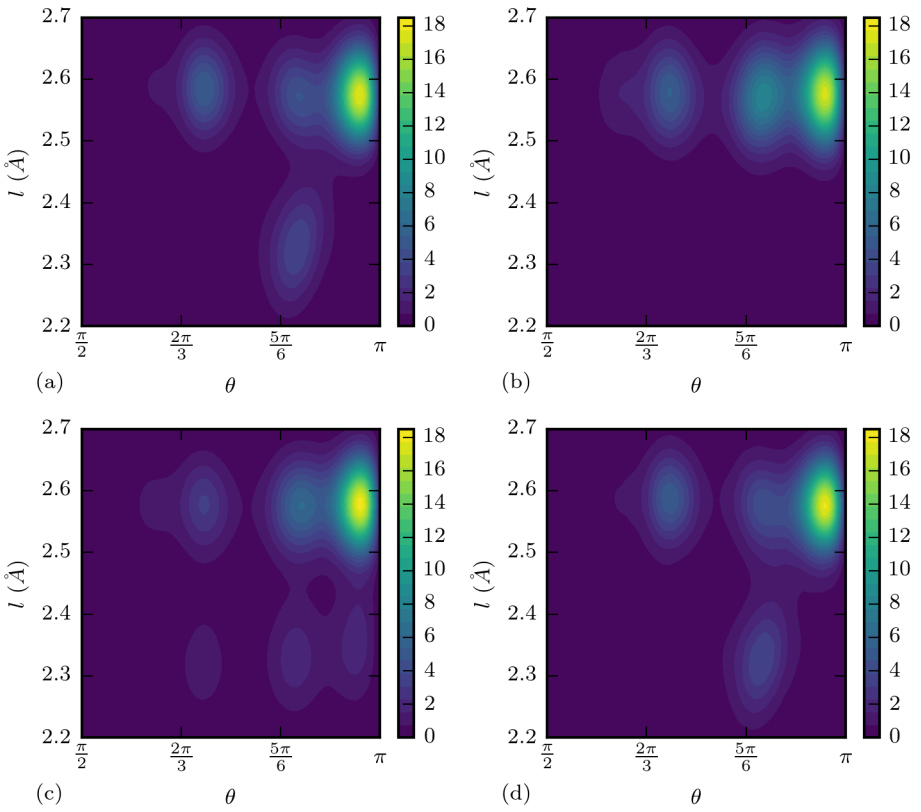

Figure 3.6: Comparison of $P(l, \theta)$ obtained from the (a) all-atom, (b) CG-HB, (c) CG-NLB, and (d) CG-BA models at 1 atm and 300 K.

and resultant total potential energy, $U(l, \theta, r)$ of the CG system is expressed as

$$U(l, \theta, r) = U(l) + U(\theta) + U(r) \tag{3.3}$$

where $U(l)$, $U(\theta)$, and $U(r)$ are the bond stretching, bending, and pair potential energies, respectively. However, as shown previously for the CG model of polyethylene, bond-lengths and bond-angles are correlated with each other and the $P(l, \theta, r)$ should be expressed as $P(l, \theta)g(r)$ to improve the fidelity of CG model of PE. Hence, the resultant total potential energy $U(l, \theta, r)$ is expressed as

$$U(l, \theta, r) = U(l, \theta) + U(r) \tag{3.4}$$

where, $U(l,\theta)$ is the potential energy arising from the correlated distributions of bond-lengths and bond-angles. In the following, we describe a computational approach to calibrate the CG model of PE by matching the correlated distributions of bond-lengths and bond-angles.

3.2.4 CG-BA Model

To calibrate the CG-BA model of PE, the CG non-bonded potential $U(r)$ is parameterized from $g(r)$ from the Boltzmann inversion of $g(r)$. The combined bond-angle energy is initialized from the Boltzmann inversion of the joint probability density $P(l,\theta)$ as:

$$U(l,\theta) = -k_B T \ln\left(\frac{P(l,\theta)}{l^2\sin(\theta)}\right), \tag{3.5}$$

where $l^2\sin(\theta)$ accounts for the Jacobian of the transformation from spherical to cartesian coordinates.

The joint probability density $P(l,\theta)$ and the combined bond-angle energy are reproduced by discreet tabulated values. The initial values of $U(l,\theta)$ are only well defined in regions of (l,θ) space where there is sufficient sampling of $P(l,\theta)$. This region where the potential is well defined is shown in Fig. 3.7(a). As simulations performed using the CG model may venture into states where the potential is not defined, we extrapolate the potential beyond the sampled space using a quadratic interpolate determined by moving least square.

In a similar approach as the fast marching method[121], the grid points are divided into three sets which are shown in Fig. 3.8(a). First set is composed of points where values of the $U(l,\theta)$ are well defined using Eq. 3.5. Second set is composed of the points neighboring the known points. The remainder of the points are called distant points. For extrapolation purpose, a neighbor list L1 is build from all the points

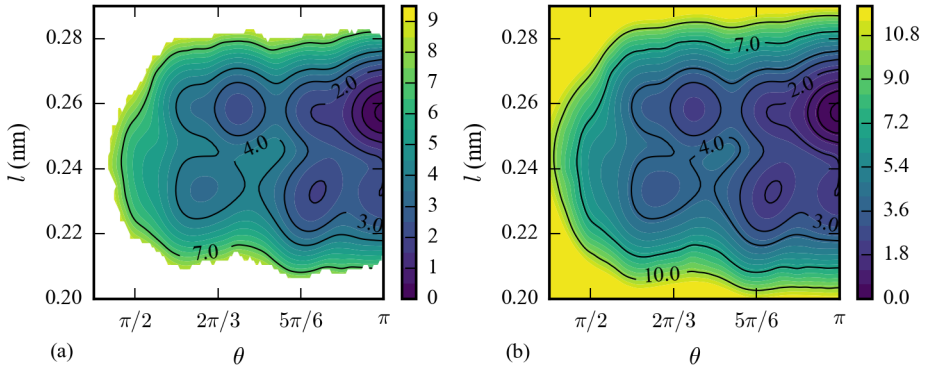

Figure 3.7: (a) $U(l, \theta)$ obtained from the correlated distributions of the bond-length and bond-angle. (b) Extrapolated $U(l, \theta)$ generated from the least square based approach. Units of $U(l, \theta)$ is in kcal/mol.

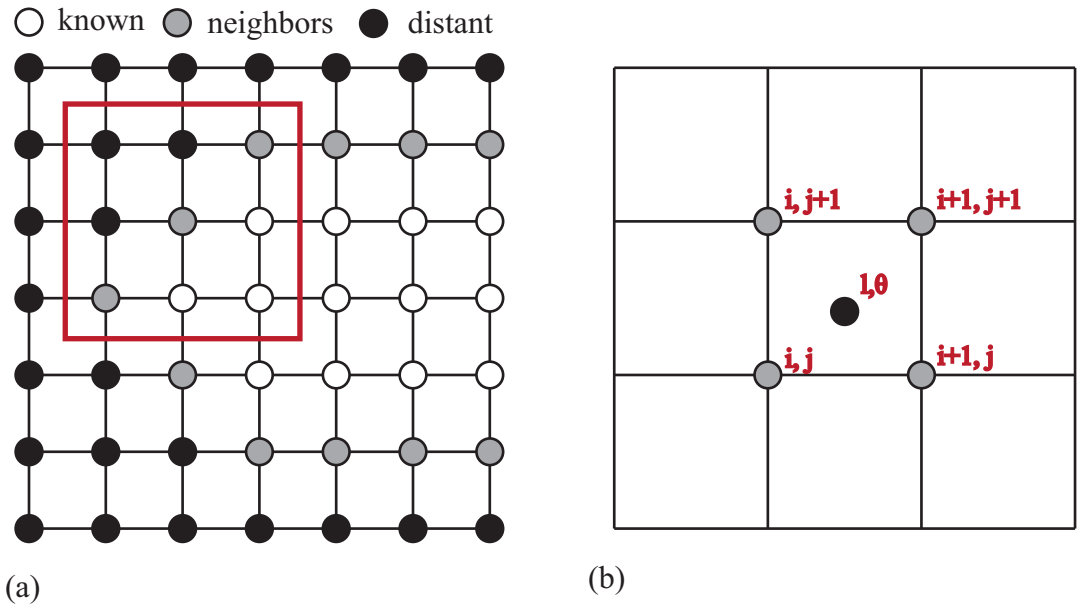

Figure 3.8: (a) Illustration of least square based method to extrapolate the $U(l, \theta)$ and (b) Illustration of bilinear interpolation of the $U(l, \theta)$.

belong to second region. A small window is created around each point (l_i, θ_i) in L1 list, which is illustrated in Fig. 3.8(a). In the CG-BA model of PE, size of the small window is chosen to be equal to $25\Delta l$ and $25\Delta\theta$. Next, an another list L2 of known points in this small window is created. From all the points in L2 list, a quadratic surface $f(l, \theta)$ (Eq. 3.6) is fit by least square based approach.

$$f(l, \theta) = a_1 + a_2 l + a_3 \theta + a_4 l\theta + a_5 l^2 + a_6 \theta^2, \tag{3.6}$$

where, a_i are the fitting parameters for $f(l, \theta)$. Briefly, for each point (l_i, θ_i) in L1 list, we fit a_i parameters using least square method from its nearby known points and use the fitted surface to extrapolate $U_{ex}(l_i, \theta_i)$.

After calculating the $U_{ex}(l_i, \theta_i)$ for each point in the L1 list, we rebuild a new neighbor list L1 from the updated known values of $U(l, \theta)$ and calculate the energies of new L1 list to extrapolate the $U(l, \theta)$ in (l, θ) space. We repeat this process untill the set of distant points is empty. Figure 3.7(b) shows the extrapolated $U(l, \theta)$ obtained from the least square based extrapolation method. This extrapolated $U(l, \theta)$ is used as an initial guess to begin CG calibrate potentials for the CG-BA model.

Once we have the initial guess of both the $U(r)$ and $U(l, \theta)$ then both the $U(r)$ and $U(l, \theta)$ are iteratively refined to match the target $g(r)$ and $P(l, \theta)$. This process is similar to the IBI method. The correction in CG potentials at each iteration step is computed as

$$U_{i+1}(r) = U_i(r) + \alpha k_B T \ln\left(\frac{g_i(r)}{g_{AA}(r)}\right) \tag{3.7}$$

$$U_{i+1}(l, \theta) = U_i(l, \theta) + \beta k_B T \ln\left(\frac{P_i(l, \theta)}{P_{AA}(l, \theta)}\right) \tag{3.8}$$

where i is the iteration number. $\alpha = 0.2$ and $\beta = 0.2$ are scaling factors to improve the convergence and stability of the iterative process. We also correct the pressure during each iteration by adding a linear term in pair potential energy as described in previous work[47].

We begin the calibration of the CG-BA model of PE by placing the 20 $(C_2H_4)_{80}$ CG bead-chains in random configurations within a cubic box of size determined with target density obtained from atomistic simulations. Initial l and θ are set to be 2.4 $\mathring{A}$ and 150° as a reasonable guess to create the initial system based on the $P(l)$ and $P(\theta)$ (Fig 3.2). At each iteration step, this initial system is used to perform CG simulation in NVE ensemble for 10 ps. This short equilibration is performed to separate atoms which are very close to each other. The $U(r)$ and $U(l,\theta)$ computed as an initial guess to begin the CG simulations. The CG system is further equilibrated for 0.48 ns at NVT ensemble. This equilibration is followed by a cycle of pressure correction steps. During this step, the CG simulations is performed for 0.64 ns at NVT ensemble and ensemble- and time-averaged pressure is computed. Then, the $U(r)$ is adjusted to match the target pressure by adding a linear correction term. After the pressure correction step, an another simulation for 0.64 ns at NVT ensemble is performed to sample the $g(r)$, $P(l)$, $P(\theta)$, and $P(l,\theta)$. Based on the deviation of $g(r)$ and $P(l,\theta)$ from the target $g_{AA}(r)$ and $P_{AA}(l,\theta)$, a correction in CG potentials is applied using the Eq. (3.7-3.8). We repeat this process till we are able to match the $g(r)$, $P(l)$, $P(\theta)$, and $P(l,\theta)$ with the target all-atom distribution functions. For the CG-BA model of PE, we are able to find the converged CG potentials within 65 iterations.

3.2.5 LAMMPS Implementation

In order to perform CG simulations using the combined bond-angle potential $U(l,\theta)$ in LAMMPS, we implemented a 2D-table style in LAMMPS to input $U(l,\theta)$, $dU(l,\theta)/dl$ and $dU(l,\theta)/d\theta$ at tabulated values of (l,θ). The gradient of the potential energy is computed using a central difference approximation at each grid point. Using these tabulated values, the energies and forces are computed by interpolating $U(l,\theta)$, $dU(l,\theta)/dl$ and $dU(l,\theta)/d\theta$ with a bilinear interpolation method over the neighboring

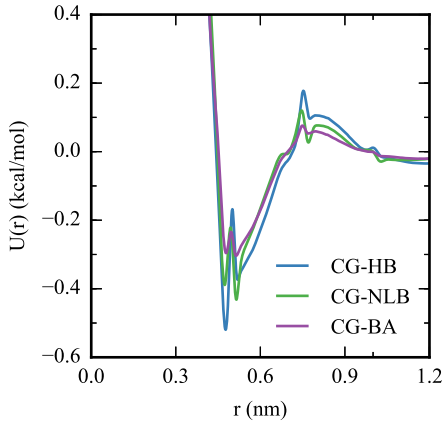

Figure 3.9: Comparison of converged pair potential obtained from (a) CG-HB model (b) CG-NLB model and (c) CG-BA model.

grid points, as shown in Fig. 3.8(b). Then we interpolate the value of $U(l,\theta)$ at any point (l_i,θ_i) using Eq. 3.9. Similarly, we also interpolate the value of $dU(l,\theta)/dl$ and $dU(l,\theta)/d\theta$ with bilinear interpolation.

$$U(l,\theta) = \frac{1}{\Delta l \Delta\theta}((l_{i+1}-l)(\theta_{j+1}-\theta)U_{ij} + (l-l_i)(\theta_{j+1}-\theta)U_{i+1,j} + (l_{i+1}-l)(\theta-\theta_j)U_{i,j+1} + (l-l_i)(\theta-\theta_j)U_{i+1,j+1}) \tag{3.9}$$

3.2.6 Model Parameterization

Figure 3.9 compares the calibrated $U(r)$ obtained from the CG-HB, CG-NLB, and CG-BA models. The CG-HB model gives the deepest potential well while the potential well of the CG-BA model is the most shallow. Fig. 3.10(a) and 3.10(b) compare the initial guess of $U(l,\theta)$ with the converged $U(l,\theta)$. Fig. 3.10(c) and 3.10(d) show the gradient of the bond-angle energy function.

As discussed previously, the CG potentials for the CG-BA model is derived by matching the $g(r)$ and $P(l,\theta)$ obtained from the atomistic and CG MD simulations.

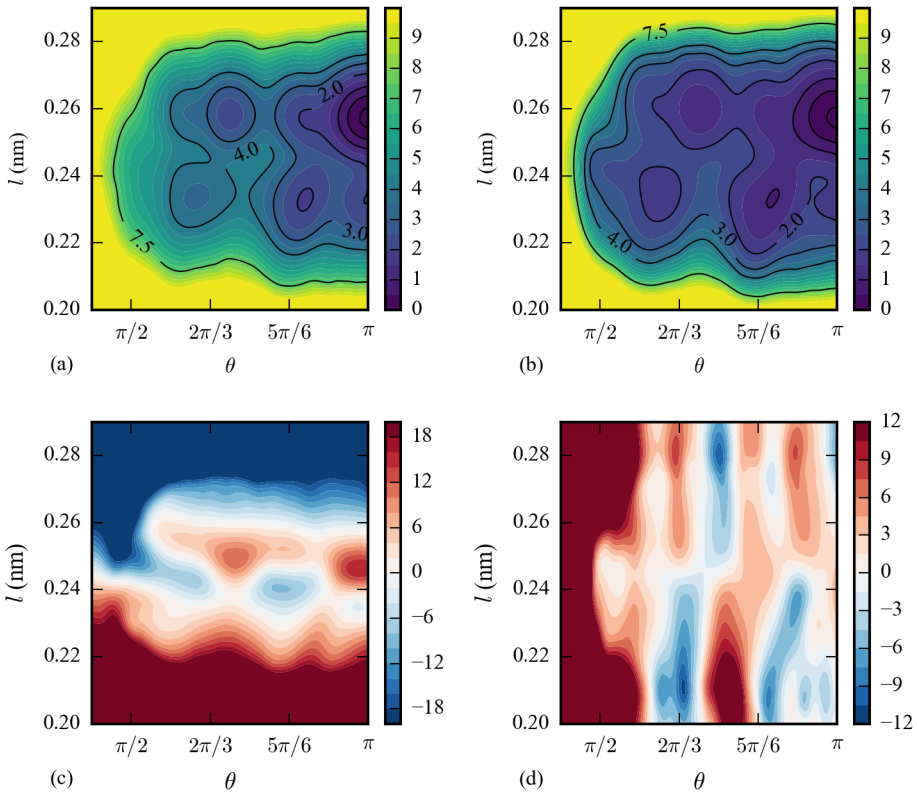

Figure 3.10: Comparison of (a) initial guess of $U(l,\theta)$, and (b) converged $U(l,\theta)$ derived from the BA-IBI method. Computed values of (c) $-\frac{\partial U(l,\theta)}{\partial l}$ and (d) $-\frac{\partial U(l,\theta)}{\partial \theta}$. Unit of potential energy values is in kcal/mol and unit of the $\frac{\partial U(l,\theta)}{\partial l}$ and $\frac{\partial U(l,\theta)}{\partial \theta}$ is in kcal/mol/$\mathring{A}$ and kcal/mol/rad, respectively.

Therefore, we first check the efficiency of the CG-BA model by comparing the $P(l,\theta)$ between the all-atom and CG-BA models in Fig. 3.6. These results prove that the CG-BA model can accurately reproduce the correlated distributions of l and θ.

3.3 Results

3.3.1 Model Validation

To verify that the CG-BA model generates accurate structure of both the crystalline and amorphous phases of PE, $P(l, \theta)$ is compared between the all-atom and CG-BA models. Figure 3.11 compares $P(l, \theta)$ obtained from amorphous phase of the all-atom and CG-BA models of PE. Also, Fig. 3.12 compare $P(l, \theta)$ obtained from crystal phase of the all-atom and CG-BA models. These results show that the CG-BA model can reproduce the local structural distributions of both the amorphous and crystalline phase of PE and small deviations arises due to the fact that these potentials are calibrated from the amorphous structure of PE at 1 atm and 300 K.

We further verify the crystal structure of PE by computing the lattice parameters and density of the PE crystal from all molecular models. These comparisons are shown in Table 3.1. Both the CG-HB and CG-NLB models give lattice parameters within 10% accuracy of the all-atom model of PE. These results are quite astonishing since the CG potentials are derived from the all-atom systems which do not show much of crystallinity.[120] Also, Table 3.2 show the comparison of volumetric and anisotropic thermal expansion coefficients from all molecular models of PE. As shown by Li et al.[119] that the crystal structure obtained from the CG-HB model gives very high volumetric and expansion around 300 K. On the contrary, we do not see such observations in crystal structure of the CG-BA model. Also, the CG-BA model shows significant improvement in thermal expansion coefficients in c direction of PE crystal. Therefore, we could say that the CG-BA model more accurately reproduce crystal phase of PE.

Further, Table 3.3 compares the computational speed-up of all the three CG models relative to the all-atom model. We find that the CG-HB model is computationally

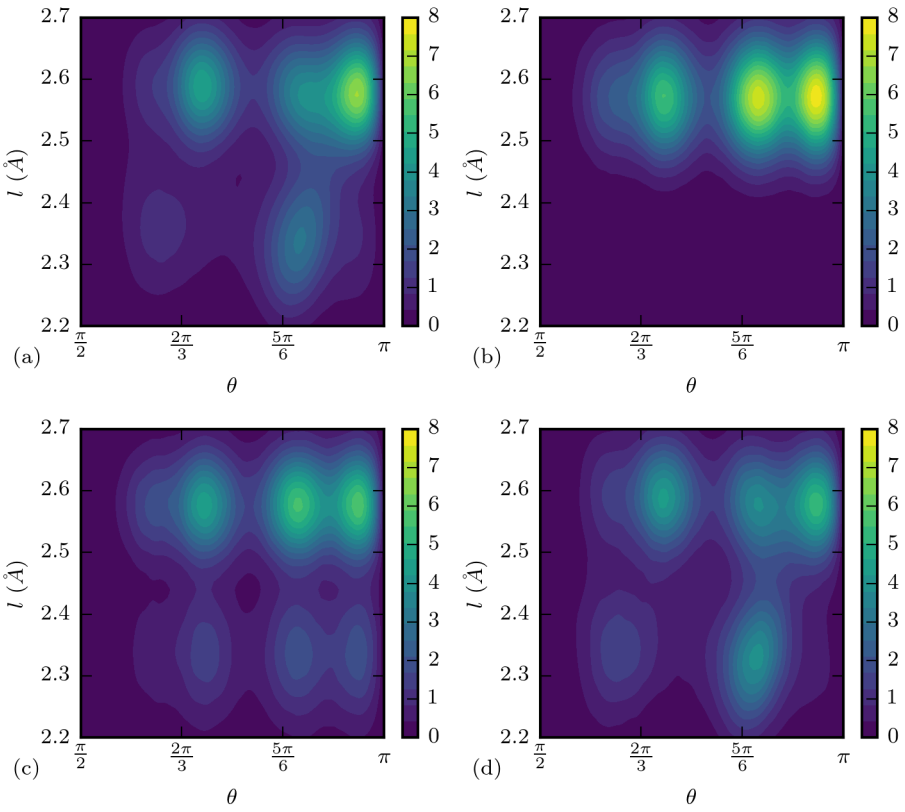

Figure 3.11: Comparison of $P(l, \theta)$ obtained from the (a) all-atom model, (b) CG-HB model, (c) CG-NLB model, and (d) CG-BA model for the amorphous phase of the PE.

efficient than the CG-NLB and CG-BA models. Also, both the CG-NLB and CG-HB model provide nearly 100x speed-up relative to the all-atom model. To check the capability of the CG-BA model in generating semicrystalline structure of PE, we perform CG simulations of system consisting 200 $(C_2H_4)_{80}$ bead chains at NPT ensemble for 100 ns from potentials derived for the CG-BA model. Figure 3.13 plots the semicrystalline structure obtained from the CG-BA model.

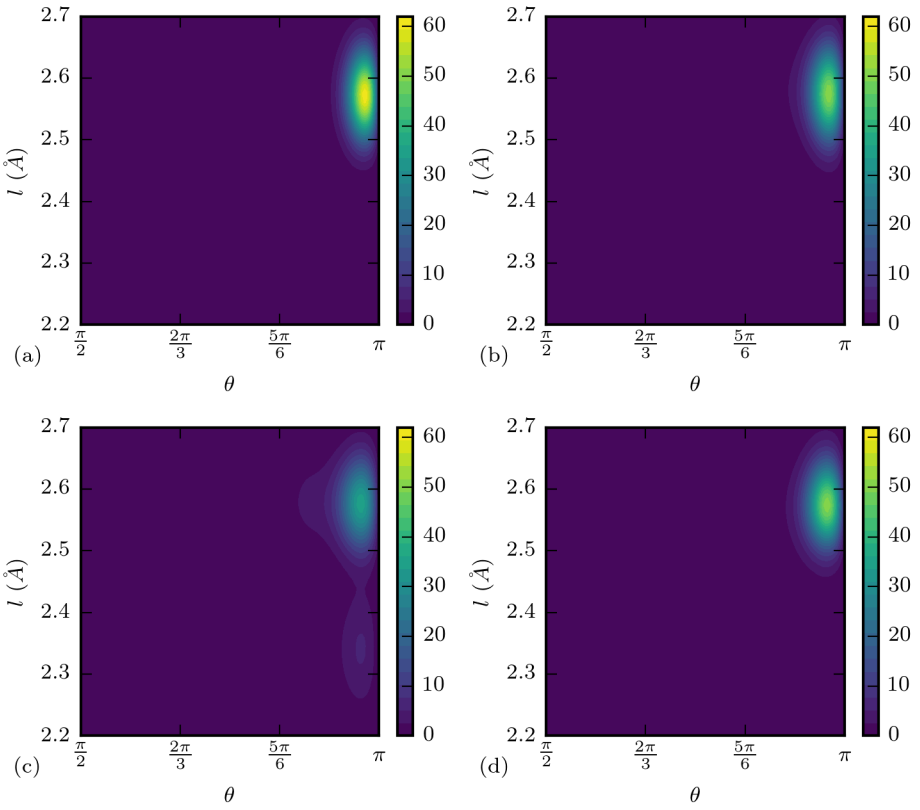

Figure 3.12: Comparison of $P(l, \theta)$ obtained from the (a) all-atom model, (b) CG-HB model (c) CG-NLB model, and (d) CG-BA model for the crystal phase of PE.

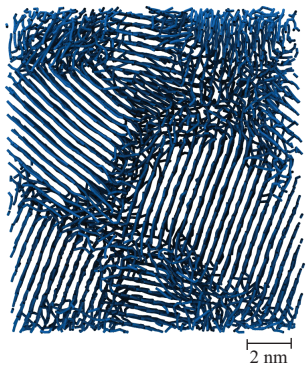

Figure 3.13: Semicrystalline domain obtained from the CG-BA model for 200 $(C_2H_4)_{80}$ PE system.

	a (Å)	b (Å)	c (Å)	ρ (g/cm^3)
Exp [122]	7.4201	4.9420	2.544	0.998
all-atom	7.6794	4.9455	2.5640	0.956
CG-HB	8.3306	4.8095	2.5630	0.907
CG-NLB	8.5692	4.9477	2.5141	0.873
CG-BA	8.4287	4.8659	2.5576	0.888

Table 3.1: Comparison of the equilibrium lattice parameters and density of PE crystal obtained from the experiment[122] and molecular models at 300 K and 1 atm.

	α_V	α_a	α_b	α_c
Exp[123]	254.5	220	38	-3.5
all-atom	366.6	448.2	-4.7	-77.1
CG-HB	2650.5	1413.1	1422.2	-184.8
CG-NLB	106.1	155.2	144.5	-194.4
CG-BA	188.9	126.3	137.5	-75.2

Table 3.2: Volumetric and anisotropic thermal expansion coefficients ($\times 10^{-6}$/K) at 300 K.

3.4 Summary

In this study, we developed a structure based CG method that can match the correlated distributions of interdependent variables. Many polymeric systems show strong correlations between the variables such as bond-length, bond-angle and torsion angles. For example, the semicrystalline PE material shows a strong correlations

Model	Timestep	CPU time (s)	Speed-up
all-atom	1 fs	1825.2	–
CG-HB	8 fs	14.2	130.3x
CG-NLB	8 fs	18.35	99.5x
CG-BA	8 fs	18.48	98.8x

Table 3.3: Computational cost comparison of the all-atom, CG-HB, CG-NLB, and CG-BA models. CPU time listed is a wall time for a 1 ps simulation performed on a single processor core. The speed up ratio is relative to the all-atom model

between the bond-length and bond-angle. In order to increase the efficiency in generating large scale polymeric systems with structure based coarse-graining techniques, these correlations of interdependent variables need to reproduced accurately. Therefore, in this study we develop a structure based coarse-graining method that enable us to reproduce the correlations of interdependent variables. A new CG model is calibrated for polyethylene to check the efficiency of this method. We find that the new model can accurately reproduces the correlations of bond-length and bond-angles of PE. Additionally, the new CG model can generate both the amorphous and crystal phases accurately.

In future, the new CG model of PE can be used to generate the large-scale molecular structure to study modeling processes such as cold-drawing and crystallization of polyethylene. Also, the new method can potentially be used to generate structure of other polymeric systems where the correlations of bond-length, bond-angle and torsion angles are important.

Chapter 4

SUMMARY AND CONCLUSIONS

Systematic coarse–graining approaches provide a useful framework for studying how the chemical composition, structure, and physical properties of polymers are related. However, coarse–grained models generated by structure matching methods generally do not represent non-structural properties accurately, can not be transferred to states different from those which they were calibrated at, and exhibit different time scales for relaxation and other dynamic processes. In this dissertation, approaches for addressing these challenges have been studied, including developing time mapping schemes to relate time scales in coarse–grained simulation to real time, performing structure matching simultaneously across a range of states to improve transferability, and extending the types of interactions to density–based and other many body effects.

The iterative Boltzmann inversion (IBI) method was applied to develop coarse-grained models for polyurea with two different mapping schemes. The first, which used two different types of coarse-grained beads, allowed for chains to pass through each other due to the large distance between bonded beads. While this makes it not effective for modeling relaxation properties, it allows for the system to very quickly explore the configurational space, greatly accelerating simulation of phase segregation to predict the equilibrium phase morphology. A second, finer mapping, employed 5 different bead types, and did not allow for chains to pass cross each other. For deriving CG potentials for 5-bead mapping scheme, overall 15 different pair potentials were optimized simultaneously. The 5-bead mapping scheme is more suitable for predicting viscoelastic properties of polyurea since it does not exhibit any topology violations, and thus represents relaxation mechanisms in the elastomer more realistically.

The effect of the molecular weight on polyurea morphology was investigated with coarse–grained MD simulations. It was observed that with a lower molecular weight, the hard domains aggregated into a smaller number of larger clusters. While the 2-bead model of polyurea provided a speedup factor of approximately 2800 compared with fully atomistic simulations, it is still challenging to reproduce the large scale structures observed with atomic force microscopy. To predict the phase morphology of polyurea more accurately, higher degrees of coarse–graining should be investigated. Furthermore, to adequately sample the configuration space, multiple levels of coarse–graining may be necessary, where very coarse descriptions are used to rapidly explore the phase space, and more fine descriptions are used to investigate local structural features.

Using the 5-bead model, the storage and loss moduli of polyurea were predicted at a frequency accessible to experimental measurement, without reliance on time–temperature superposition. A dynamic time scaling function was applied to map the CG time scale to atomistic time scale for computing viscoelastic properties of polyurea. The computed CG moduli were compared with experimental moduli determined from dynamic mechanical analysis and ultrasonic measurements. Predicted storage and loss modulus from the CG model are in good agreement with experimental measurements for frequencies ranging from milliseconds to microseconds. While the CG model overpredicts the moduli compared with values determined experimental measurements transformed by time-temperature superposition, it is in agreement with atomistic model. The discrepancy between experimentally determined moduli and molecular simulations at these higher frequencies likely arises due to the thermorheological complexity of polyurea. The coarse-grained methodology developed in this work is quite general, and enabling investigation of the morphology and viscoelastic properties of different variants of polyurea like materials and other elastomers.

CG methods have shown capability in generating large scale molecular structures. Structural distribution functions of semicrystalline polymers are greatly influenced by degree of coarse-graining and optimal CG mapping scheme is chosen to minimize the correlations between variables such as bond-length, bond-angle and torsion angle. However, in the case of semicrystalline polyethylene, retaining the atomic level structure from CG models is important to accurately generate structures for both amorphous and crystal phases and such CG mapping scheme shows the correlations in bond-length and bond-angle. Therefore, these correlated distributions need to be match by the coarse-grained model of polyethylene to improve the semicrystalline polymer structure.

In this study, a coarse-graining approach was developed for creating CG potentials if the probability distributions of variables can only be partially factorized. In this approach, the IBI method was extended to match the correlated distributions of bond-lengths and bond-angles. For extrapolating the combined bond angle potential energy surface, an extrapolation scheme was applied by combining the fast marching method with the moving least square based approach. To perform CG simulations with the new CG method, a 2D tabulated potential was implemented in LAMMPS, which took account of combined degree of freedom related to bond-stretching and bond-bending. This method could easily extended to match joint probability distributions between different variable such as bond-angle and torsion angle. With application of the new CG method, derived potential can accurately model both amorphous and crystal structure of polyethylene.

The new CG model of polyethylene which was derived by matching the correlated distributions of bond-length and bond-angle, provides a hundred fold speedup compared with atomistic MD simulations and approximately a speedup factor of three compared to the united atom model. Due to the computational speedup gained from

the new model, a large scale semicrystalline structure will be generated to study the spinodal decomposition of polyethylene. Simulation of polymer crystallization and melting is a challenging task because these processes are slow on the molecular time scale; also chains must be long enough to reveal experimentally realistic situations. Therefore, the new CG model give us capability to understand the effect of strain, cooling rate, and molecular weight on the crystallization with a relatively low computational cost.

A density-dependent interaction and least squares method was developed for the calibration of CG potentials to improve transferability and representability of CG model. With application of new method, it was showed that a CG model could be calibrated to reproduce isotherm and predict Hugoniot. It represents an important step forward in transferable and representative CG potentials. This model in future will be extend to compute the shock response of complicated polymers e.g. polyurea.

Analysis of the rise in temperature along the shock Hugoniot and comparison with analytical predictions from the Mie-Grüneisen equation of state was performed to thoroughly explore the thermodynamic consistency of the model. The Gruneisen parameter for polyethylene was computed along the Hugoniot from molecular simulations, which is extremely difficult to measure from experiments. The heat capacity computed from CG models are based on classical harmonic approximations and inclusion of quantum effects to correct the heat capacity of CG models will give more accurate estimation of the predicted temperature rise from CG models. In future, the new CG model will be used to investigate the effect of crystallinity and texture on the shock properties of polyethylene. Also, the new model will be used to investigate morphological change caused by shock loading for polyethylene and polyurea material.

REFERENCES

[1] S. Das, D. F. Cox, G. L. Wilkes, D. B. Klinedinst, I. Yilgor, E. Yilgor, F. L. Beyer, Effect of symmetry and h-bond strength of hard segments on the structure-property relationships of segmented, nonchain extended polyurethanes and polyureas, Journal of Macromolecular Science, Part B: Physics 46 (5) (2007) 853–875.

[2] D. Chattopadhyay, K. Raju, Structural engineering of polyurethane coatings for high performance applications, Progress in Polymer Science 32 (3) (2007) 352–418.

[3] J. A. Pathak, J. N. Twigg, K. E. Nugent, D. L. Ho, E. K. Lin, P. H. Mott, C. G. Robertson, M. K. Vukmir, T. H. E. Iii, C. M. Roland, Structure evolution in a polyurea segmented block copolymer because of mechanical deformation, Macromolecules 41 (2008) 7543–7548.

[4] Legge, N.R.; Holden, G.; Schroeder, H.E. Thermoplastic Elastomers: A Comprehensive Review; Hanser Publishers: New York, 1987.

[5] D. Fragiadakis, R. Gamache, R. Bogoslovov, C. Roland, Segmental dynamics of polyurea: Effect of stoichiometry, Polymer 51 (1) (2010) 178–184.

[6] C. Roland, J. Twigg, Y. Vu, P. Mott, High strain rate mechanical behavior of polyurea, Polymer 48 (2) (2007) 574–578.

[7] R. G. S. Barsoum, Elastomeric Polymers for Shockwave Mitigation and Extreme Loading Conditions, Springer, New York, 2013.

[8] S. Tekalur, A. Shukla, K. Shivakumar, Blast resistance of polyurea based layered composite materials, Composite Structures 84 (3) (2008) 271–281.

[9] N. Gardner, E. Wang, P. Kumar, A. Shukla, Blast mitigation in a sandwich composite using graded core and polyurea interlayer, Experimental Mechanics 52 (2012) 119–133.

[10] Versalink P-1000 Polytetramethyleneoxide-di-p-aminobenzoate, Pub No. 140-05-050-US, Polyurethane Specialty Products group, Air Products and Chemicals (2005).

[11] The Dow Chemical Company, Isonate 143L; Modified MDI, Dow Chemical, Midland, MI, 2001.

[12] J. D. Ferry, Viscoelastic Properties of Polymers, 3rd ed., Wiley, New York, 1990.

[13] N. W. Tschoegl, W. G. Knauss, I. Emri, The effect of temperature and pressure on the mechanical properties of thermo-and/or piezorheologically simple polymeric materials in thermodynamic equilibrium–a critical review, Mechanics of Time-Dependent Materials 6 (1) (2002) 53–99.

[14] W.G. Knauss. Viscoelastic Material Characterization relative to Constitutive and Failure Response of an Elastomer, Interim Report to the Office of Naval Research (GALCIT, Pasadena, CA, 2003).

[15] J. Zhao, W. Knauss, G. Ravichandran, Applicability of the time–temperature superposition principle in modeling dynamic response of a polyurea, Mechanics of Time-Dependent Materials 11 (3-4) (2007) 289–308.

[16] A. Amirkhizi, J. Isaacs, J. McGee, S. Nemat-Nasser, An experimentally-based viscoelastic constitutive model for polyurea, including pressure and temperature effects, Philosophical Magazine 86 (36) (2006) 5847–5866.

[17] J. Qiao, A. Amirkhizi, K. Schaaf, S. Nemat-Nasser, G. Wu, Dynamic mechanical and ultrasonic properties of polyurea, Mechanics of Materials 43 (10) (2011) 598–607.

[18] Y. Li, S. Tang, B. C. Abberton, M. Kröger, C. Burkhart, B. Jiang, G. J. Papakonstantopoulos, M. Poldneff, W. K. Liu, A predictive multiscale computational framework for viscoelastic properties of linear polymers, Polymer 53 (25) (2012) 5935–5952.

[19] C. Tzoumanekas, D. N. Theodorou, Topological analysis of linear polymer melts: a statistical approach, Macromolecules 39 (13) (2006) 4592–4604.

[20] P.-G. De Gennes, Scaling concepts in polymer physics, Cornell university press, 1979.

[21] M. Doi, S. Edwards, The Theory of Polymer Dynamics, International Series of Monographs on Physics, Clarendon Press, 1988.

[22] Y. Li, B. C. Abberton, M. Kröger, W. K. Liu, Challenges in multiscale modeling of polymer dynamics, Polymers 5 (2) (2013) 751–832.

[23] A. Castagna, A. Pangon, T. Choi, G. Dillon, J. Runt, The role of soft segment molecular weight on microphase separation and dynamics of bulk polymerized polyureas, Macromolecules 45 (20) (2012) 8438–8444.

[24] A. S. Sarvestani, Modeling the solid-like behavior of entangled polymer nanocomposites at low frequency regimes, European Polymer Journal 44 (2) (2008) 263–269.

[25] S. Izvekov, M. Parrinello, C. Burnham, G. Voth, Effective force fields for condensed phase systems from ab initio molecular dynamics simulation: A new method for force-matching, The Journal of Chemical Physics 120 (2004) 10896.

[26] W. Noid, J.-W. Chu, G. S. Ayton, V. Krishna, S. Izvekov, G. A. Voth, A. Das, H. C. Andersen, The multiscale coarse-graining method. i. a rigorous bridge between atomistic and coarse-grained models, The Journal of Chemical Physics 128 (24) (2008) 244114.

[27] A. P. Lyubartsev, A. Laaksonen, Calculation of effective interaction potentials from radial distribution functions: A reverse monte carlo approach, Physical Review E 52 (4) (1995) 3730.

[28] D. Reith, H. Meyer, F. Müller-Plathe, Mapping atomistic to coarse-grained polymer models using automatic simplex optimization to fit structural properties, Macromolecules 34 (7) (2001) 2335–2345.

[29] F. Müller-Plathe, Coarse-graining in polymer simulation: From the atomistic to the mesoscopic scale and back, ChemPhysChem 3 (9) (2002) 754–769.

[30] D. Reith, M. Pütz, F. Müller-Plathe, Deriving effective mesoscale potentials from atomistic simulations, Journal of Computational Chemistry 24 (13) (2003) 1624–1636.

[31] M. S. Shell, The relative entropy is fundamental to multiscale and inverse thermodynamic problems, J. Chem. Phys 129 (144) (2008) 108.

[32] A. Chaimovich, M. S. Shell, Coarse-graining errors and numerical optimization using a relative entropy framework, The Journal of Chemical Physics 134 (9) (2011) 094112.

[33] D. D. Hsu, W. Xia, S. G. Arturo, S. Keten, Systematic method for thermomechanically consistent coarse-graining: a universal model for methacrylate-based polymers, Journal of Chemical Theory and Computation 10 (6) (2014) 2514–2527.

[34] D. D. Hsu, W. Xia, S. G. Arturo, S. Keten, Thermomechanically consistent and temperature transferable coarse-graining of atactic polystyrene, Macromolecules.

[35] G. Maurel, B. Schnell, F. Goujon, M. Couty, P. Malfreyt, Multiscale modeling approach toward the prediction of viscoelastic properties of polymers, Journal of Chemical Theory and Computation 8 (11) (2012) 4570–4579.

[36] G. Maurel, F. Goujon, B. Schnell, P. Malfreyt, Prediction of structural and thermomechanical properties of polymers from multiscale simulations, RSC Advances 5 (19) (2015) 14065–14073.

[37] F. Lahmar, B. Rousseau, Influence of the adjustable parameters of the dpd on the global and local dynamics of a polymer melt, Polymer 48 (12) (2007) 3584–3592.

[38] G. Milano, F. Müller-Plathe, Mapping atomistic simulations to mesoscopic models: A systematic coarse-graining procedure for vinyl polymer chains, Journal of Physical Chemistry B 109 (39) (2005) 18609–18619.

[39] B. Bayramoglu, R. Faller, Coarse-grained modeling of polystyrene at different concentrations using the iterative boltzmann inversion technique, Bulletin of the American Physical Society 56.

[40] K. Kamio, K. Moorthi, D. N. Theodorou, Coarse grained end bridging monte carlo simulations of poly(ethylene terephthalate) melt, Macromolecules 40 (2007) 710–722.

[41] Accelrys, Accelrys 2012, "http://accelrys.com/products/materials-studio/.

[42] S. Plimpton, P. Crozier, A. Thompson, LAMMPS-large-scale atomic/molecular massively parallel simulator, Sandia National Laboratories.

[43] H. Sun, Compass: An ab initio force-field optimized for condensed-phase applications overview with details on alkane and benzene compounds, Journal of Physical Chemistry B 102 (38) (1998) 7338–7364.

[44] M. Hwang, T. Stockfisch, A. Hagler, Derivation of class II force fields. 2. derivation and characterization of a class II force field, cff93, for the alkyl functional group and alkane molecules, Journal of the American Chemical Society 116 (6) (1994) 2515–2525.

[45] M. McQuaid, H. Sun, D. Rigby, Development and validation of compass force field parameters for molecules with aliphatic azide chains, Journal of Computational Chemistry 25 (1) (2003) 61–71.

[46] D. Frenkel, B. Smit, Understanding Molecular Simulation: From Algorithms to Applications, Computational Science, Elsevier Science, 2001.

[47] R. Faller, Automatic coarse graining of polymers, Polymer 45 (11) (2004) 3869–3876.

[48] V. Ruhle, C. Junghans, A. Lukyanov, K. Kremer, D. Andrienko, Versatile object-oriented toolkit for coarse-graining applications, Journal of Chemical Theory and Computation 5 (12) (2009) 3211–3223.

[49] H. Eslami, H. A. Karimi-Varzaneh, F. Müller-Plathe, Coarse-grained computer simulation of nanoconfined polyamide-6, 6, Macromolecules 44 (8) (2011) 3117–3128.

[50] S. Plimpton, Fast parallel algorithms for short-range molecular dynamics, Journal of Computational Physics 117 (1995) 1–17.

[51] M. Allen, D. Tildesley, Computer simulation of liquids., Oxford Science Publications, Oxford University Press, 1989.
URL http://books.google.com/books?id=O32VXB9e5P4C

[52] Y. Zhou, M. Karplus, J. M. Wichert, C. K. Hall, Equilibrium thermodynamics of homopolymers and clusters: Molecular dynamics and monte carlo simulations of systems with square-well interactions, The Journal of Chemical Physics 107 (1997) 10691.

[53] B. Arman, A. Srinivas Reddy, G. Arya, Viscoelastic properties and shock response of coarse-grained models of multiblock versus diblock copolymers: Insights into dissipative properties of polyurea, Macromolecules 45 (7) (2012) 3247.

[54] S. Sen, S. K. Kumar, P. Keblinski, Viscoelastic properties of polymer melts from equilibrium molecular dynamics simulations, Macromolecules 38 (3) (2005) 650–653.

[55] M. Amini, J. Simon, S. Nemat-Nasser, Numerical modeling of effect of polyurea on response of steel plates to impulsive loads in direct pressure-pulse experiments, Mechanics of Materials 42 (6) (2010) 615–627.

[56] M. Rubinstein, R. H. Colby, Polymer Physics, OUP Oxford, 2003.

[57] D. Fritz, K. Koschke, V. A. Harmandaris, N. F. van der Vegt, K. Kremer, Multiscale modeling of soft matter: scaling of dynamics, Physical Chemistry Chemical Physics 13 (22) (2011) 10412–10420.

[58] D. Fritz, C. R. Herbers, K. Kremer, N. F. van der Vegt, Hierarchical modeling of polymer permeation, Soft Matter 5 (22) (2009) 4556–4563.

[59] S. Kumar, R. G. Larson, Brownian dynamics simulations of flexible polymers with spring–spring repulsions, The Journal of Chemical Physics 114 (15) (2001) 6937–6941.

[60] T. W. Sirk, Y. R. Slizoberg, J. K. Brennan, M. Lisal, J. W. Andzelm, An enhanced entangled polymer model for dissipative particle dynamics, The Journal of Chemical Physics 136 (13) (2012) 134903.

[61] Y. R. Sliozberg, T. W. Sirk, J. K. Brennan, J. W. Andzelm, Bead-spring models of entangled polymer melts: Comparison of hard-core and soft-core potentials, Journal of Polymer Science Part B: Polymer Physics 50 (24) (2012) 1694–1698.

[62] A. E. Likhtman, S. K. Sukumaran, J. Ramirez, Linear viscoelasticity from molecular dynamics simulation of entangled polymers, Macromolecules 40 (18) (2007) 6748–6757.

[63] R. Kimmich, N. Fatkullin, Polymer chain dynamics and NMR, in: NMR • 3D Analysis • Photopolymerization, Vol. 170 of Advances in Polymer Science, Springer Berlin Heidelberg, 2004, pp. 1–113. doi:10.1007/b12766.

[64] W. B. Lee, K. Kremer, Entangled polymer melts: Relation between plateau modulus and stress autocorrelation function, Macromolecules 42 (16) (2009) 6270–6276.

[65] R. Zwanzig, R. D. Mountain, High-frequency elastic moduli of simple fluids, The Journal of Chemical Physics 43 (12) (1965) 4464–4471.

[66] V. Agrawal, K. Holzworth, W. Nantasetphong, A. V. Amirkhizi, J. Oswald, S. Nemat-Nasser, Prediction of viscoelastic properties with coarse-grained molecular dynamics and experimental validation for a benchmark polyurea system, Journal of Polymer Science Part B: Polymer Physics.

[67] Q. Sun, R. Faller, Systematic coarse-graining of a polymer blend: Polyisoprene and polystyrene, Journal of Chemical Theory and Computation 2 (3) (2006) 607–615.

[68] Q. Sun, R. Faller, Phase separation in polyisoprene/polystyrene blends by a systematically coarse-grained model, The Journal of Chemical Physics 126 (2007) 144908.

[69] J. Yi, M. Boyce, G. Lee, E. Balizer, Large deformation rate-dependent stress–strain behavior of polyurea and polyurethanes, Polymer 47 (1) (2006) 319–329.

[70] C. Roland, R. Casalini, Effect of hydrostatic pressure on the viscoelastic response of polyurea, Polymer 48 (19) (2007) 5747–5752.

[71] T. L. Chantawansri, T. W. Sirk, E. F. Byrd, J. W. Andzelm, B. M. Rice, Shock hugoniot calculations of polymers using quantum mechanics and molecular dynamics, The Journal of Chemical Physics 137 (20) (2012) 204901.

[72] K. Kremer, G. S. Grest, Dynamics of entangled linear polymer melts: A molecular-dynamics simulation, The Journal of Chemical Physics 92 (1990) 5057.

[73] V. Agrawal, G. Arya, J. Oswald, Simultaneous iterative boltzmann inversion for coarse-graining of polyurea, Macromolecules.

[74] S. Izvekov, G. Voth, A multiscale coarse-graining method for biomolecular systems, The Journal of Physical Chemistry B 109 (7) (2005) 2469–2473.

[75] S. Izvekov, A. Violi, G. A. Voth, Systematic coarse-graining of nanoparticle interactions in molecular dynamics simulation, The Journal of Physical Chemistry B 109 (36) (2005) 17019–17024.

[76] M. Grujicic, J. Snipes, S. Ramaswami, R. Yavari, J. Runt, J. Tarter, G. Dillon, Coarse-grained molecular-level analysis of polyurea properties and shock-mitigation potential, Journal of materials engineering and performance 22 (7) (2013) 1964–1981.

[77] W. Mock Jr, S. Bartyczak, G. Lee, J. Fedderly, K. Jordan, Dynamic properties of polyurea 1000, in: Shock Compression of Condensed Matter 2009: Proceedings of the American Physical Society Topical Group on Shock Compression of Condensed Matter, Vol. 1195, AIP Publishing, 2009, pp. 1241–1244.

[78] K. P. Santo, M. L. Berkowitz, Shock wave interaction with a phospholipid membrane: coarse-grained computer simulations, The Journal of chemical physics 140 (5) (2014) 054906.

[79] K. P. Santo, M. L. Berkowitz, Shock wave induced collapse of arrays of nanobubbles located next to a lipid membrane: coarse-grained computer simulations, The Journal of Physical Chemistry B 119 (29) (2014) 8879–8889.

[80] S. J. Marrink, H. J. Risselada, S. Yefimov, D. P. Tieleman, A. H. De Vrie s, The martini force field: coarse grained model for biomolecular simulations, The Journal of Physical Chemistry B 111 (27) (2007) 7812–7824.

[81] Y. Fu, J. Michopoulos, J.-H. Song, Dynamics response of polyethylene polymer nanocomposites to shock wave loading, Journal of Polymer Science Part B: Polymer Physics 53 (18) (2015) 1292–1302.

[82] D. Brown, J. H. Clarke, Molecular dynamics simulation of an amorphous polymer under tension. 1. phenomenology, Macromolecules 24 (8) (1991) 2075–2082.

[83] F. M. Capaldi, M. C. Boyce, G. C. Rutledge, Molecular response of a glassy polymer to active deformation, Polymer 45 (4) (2004) 1391–1399.

[84] H. A. Karimi-Varzaneh, N. F. van der Vegt, F. Müller-Plathe, P. Carbone, How good are coarse-grained polymer models? a comparison for atactic polystyrene, ChemPhysChem 13 (15) (2012) 3428–3439.

[85] P. Carbone, H. Varzaneh, X. Chen, F. Müller-Plathe, Transferability of coarse-grained force fields: The polymer case, The Journal of Chemical Physics 128 (2008) 064904.

[86] R. Henderson, A uniqueness theorem for fluid pair correlation functions, Physics Letters A 49 (3) (1974) 197–198.

[87] M. E. Johnson, T. Head-Gordon, A. A. Louis, Representability problems for coarse-grained water potentials, The Journal of Chemical Physics 126 (14) (2007) 144509.

[88] R. DeVane, M. L. Klein, C.-c. Chiu, S. O. Nielsen, W. Shinoda, P. B. Moore, Coarse-grained potential models for phenyl-based molecules: I. parametrization using experimental data, The Journal of Physical Chemistry B 114 (19) (2010) 6386–6393.

[89] T. W. Rosch, J. K. Brennan, S. Izvekov, J. W. Andzelm, Exploring the ability of a multiscale coarse-grained potential to describe the stress-strain response of glassy polystyrene, Physical Review E 87 (4) (2013) 042606.

[90] T. C. Moore, C. R. Iacovella, C. McCabe, Derivation of coarse-grained potentials via multistate iterative boltzmann inversion, The Journal of Chemical Physics 140 (22) (2014) 224104.

[91] M. S. Daw, M. I. Baskes, Embedded-atom method: Derivation and application to impurities, surfaces, and other defects in metals, Physical Review B 29 (12) (1984) 6443.

[92] J. R. Maple, M.-J. Hwang, T. P. Stockfisch, U. Dinur, M. Waldman, C. S. Ewig, A. T. Hagler, Derivation of class ii force fields. i. methodology and quantum force field for the alkyl functional group and alkane molecules, Journal of Computational Chemistry 15 (2) (1994) 162–182.

[93] A. Clark, J. McCarty, I. Lyubimov, M. Guenza, Thermodynamic consistency in variable-level coarse graining of polymeric liquids, Physical Review Letters 109 (16) (2012) 168301.

[94] H. Qian, P. Carbone, X. Chen, H. Karimi-Varzaneh, C. Liew, F. Müller-Plathe, Temperature-transferable coarse-grained potentials for ethylbenzene, polystyrene, and their mixtures, Macromolecules 41 (24) (2008) 9919–9929.

[95] C. A. Croxton, Liquid state physics, Liquid State Physics. A Statistical Introduction. Cambridge Monographs on Physics. ISBN: 9780521114349 1.

[96] D. McQuarrie, Statistical mechanics, Happer and Row, New York.

[97] E. J. Reed, L. E. Fried, J. Joannopoulos, A method for tractable dynamical studies of single and double shock compression, Physical Review Letters 90 (23) (2003) 235503.

[98] J. B. Hooper, D. Bedrov, G. D. Smith, B. Hanson, O. Borodin, D. M. Dattelbaum, E. M. Kober, A molecular dynamics simulation study of the pressure-volume-temperature behavior of polymers under high pressure, The Journal of Chemical Physics 130 (14) (2009) 144904.

[99] A. T. J. Hayward, Compressibility equations for liquids: a comparative study, British Journal of Applied Physics 18 (7) (1967) 965.

[100] A. L. Kovarskii, High-pressure chemistry and physics of polymers, CRC Press, 1994.

[101] V. Nanda, R. Simha, Theoretical interpretation of tait equation parameters, The Journal of Chemical Physics 41 (6) (1964) 1884–1885.

[102] R. R. Matheson, Analysis of some equations of state in relation to microscopic interpretations of mechanically significant entropy for polymeric glasses and melts, Journal of Physical Chemistry 91 (23) (1987) 6062–6066.

[103] S. P. Marsh, LASL shock Hugoniot data, Vol. 5, Univ of California Press, 1980.

[104] M. A. Meyers, Dynamic behavior of materials, John Wiley & Sons, 1994.

[105] R. W. Warfield, The grüneisen constant of polymers, Die Makromolekulare Chemie 175 (11) (1974) 3285–3297.

[106] Y. Wada, A. Itani, T. Nishi, S. Nagai, Grüneisen constant and thermal properties of crystalline and glassy polymers, Journal of Polymer Science Part A-2: Polymer Physics 7 (1) (1969) 201–208.

[107] R. Barker Jr, Grüneisen numbers for polymeric solids, Journal of Applied Physics 38 (11) (1967) 4234–4242.

[108] J. W. Forbes, Shock wave compression of condensed matter: a primer, Springer, 2013.

[109] T. R. Mattsson, J. M. D. Lane, K. R. Cochrane, M. P. Desjarlais, A. P. Thompson, F. Pierce, G. S. Grest, First-principles and classical molecular dynamics simulation of shocked polymers, Physical Review B 81 (5) (2010) 054103.

[110] S. Lee, G. C. Rutledge, Plastic deformation of semicrystalline polyethylene by molecular simulation, Macromolecules 44 (8) (2011) 3096–3108.

[111] I.-C. Yeh, J. W. Andzelm, G. C. Rutledge, Mechanical and structural characterization of semicrystalline polyethylene under tensile deformation by molecular dynamics simulations, Macromolecules 48 (12) (2015) 4228–4239.

[112] S. Jabbari-Farouji, J. Rottler, O. Lame, A. Makke, M. Perez, J.-L. Barrat, Plastic deformation mechanisms of semicrystalline and amorphous polymers, ACS Macro Letters 4 (2) (2015) 147–150.

[113] A. Koyama, T. Yamamoto, K. Fukao, Y. Miyamoto, Molecular dynamics studies on local ordering in amorphous polyethylene, The Journal of Chemical Physics 115 (1) (2001) 560–566.

[114] T. Yamamoto, Molecular dynamics simulation of polymer crystallization through chain folding, The Journal of chemical physics 107 (7) (1997) 2653–2663.

[115] Y. Men, J. Rieger, P. Lindner, H.-F. Enderle, D. Lilge, M. O. Kristen, S. Mihan, S. Jiang, Structural changes and chain radius of gyration in cold-drawn polyethylene after annealing: Small-and wide-angle x-ray scattering and small-angle neutron scattering studies, The Journal of Physical Chemistry B 109 (35) (2005) 16650–16657.

[116] O. Bezkorovaynaya, A. Lukyanov, K. Kremer, C. Peter, Multiscale simulation of small peptides: Consistent conformational sampling in atomistic and coarse-grained models, Journal of computational chemistry 33 (9) (2012) 937–949.

[117] V. A. Harmandaris, D. Reith, N. F. Van der Vegt, K. Kremer, Comparison between coarse-graining models for polymer systems: Two mapping schemes for polystyrene, Macromolecular chemistry and physics 208 (19-20) (2007) 2109–2120.

[118] H. Fukunaga, J.-i. Takimoto, M. Doi, A coarse-graining procedure for flexible polymer chains with bonded and nonbonded interactions, Journal of Chemical Physics 116 (2002) 8183.

[119] Y. Li, V. Agrawal, J. Oswald, On the ability of coarse–grained potentials to model amorphous and crystalline phases of macromolecules, Journal of Computational Chemistry.

[120] V. Agrawal, P. Peralta, J. Oswald, A pressure-transferable coarse-grained potential for modeling the shock hugoniot of polyethylene, Journal of Chemical Physics.

[121] J. A. Sethian, A fast marching level set method for monotonically advancing fronts, Proceedings of the National Academy of Sciences 93 (4) (1996) 1591–1595.

[122] G. Davis, R. Eby, J. Colson, Thermal expansion of polyethylene unit cell: effect of lamella thickness, Journal of Applied Physics 41 (11) (1970) 4316–4326.

[123] P. R. Swan, Polyethylene unit cell variations with temperature, Journal of Polymer Science 56 (164) (1962) 403–407.